Manufacturing and Sputter Behaviour of Cold Gas Sprayed Sputter Targets

Dipl.-Ing. Roland Lorenz

being a thesis in partial fulfilment of the requirements for the degree of a

Doktor der montanistischen Wissenschaften (Dr. mont.)

at the Montanuniversität Leoben

Leoben, March 2018

Affidavit

I declare in lieu of oath, that I wrote this thesis and performed the associated research myself, using only literature cited in this volume.

Leoben, March 2018 _____

ACKNOWLEDGMENTS

In the first place I would like to express my gratitude to Prof. Christian Mitterer, head of the chair of Functional Materials and Materials Systems at the Department of Physical Metallurgy and Materials Testing for the excellent guiding and for giving me the opportunity to conduct the present work.

Furthermore, I would like to thank all my colleagues at the Chair of Functional Materials and Materials Systems. It was a great pleasure for me sharing the past three years with you, having fruitful discussions during, but also after work.

I would like to thank our project partners from Plansee SE with whom we have worked out this interesting topic. My special gratitude are for Michael O'Sullivan and his co-workers for the great cooperation and their input during our project meetings over the years.

My greatest thanks are for my family: My parents Miranda and Manfred and my sister Franziska providing me all the support during my studies but also during the time of this dissertation. Thank you for everything!

TABLE OF CONTENTS

1. INTRODUCTION

Thin film technology is considered as a current key material technology and the increasing number of thin film products are strong economic drivers within our economy, including microelectronics, photovoltaics, optical components and flat panel displays. With a broad range of advanced physical, chemical or electrical properties, the deposited thin films represent an important part of surface engineering [1,2].

Multifunctional thin films based on molybdenum (Mo) and Mo alloys have undergone an intense development during the recent years. Particularly, the versatile range of properties approved Mo as a suitable material for a large number of different applications. With its low electrical resistivity and high thermal stability it is used as back contact layer for Cu(In,Ga)Se_2 (CIGS) solar cells [3–6]. In microelectronics and the manufacturing of thin film transistor-liquid crystal displays (TFT-LCD), Mo thin films act as diffusion barriers between Cu and Si, preventing the formation of the Cu_3Si phase. Due to its high melting point, Mo is characterised by a low diffusivity. Further, Mo thin films show a good line patterning by dry or wet etching, a key step in TFT manufacturing [5,7–9]. Moreover, Mo thin films are widely used as gate and source/drain signal lines and interconnect material in data bus lines for TFT-LCD or touch screen panels, again because of the low electrical resistivity, the easy patterning and the strong adhesion to glass [3,5,6,8,9]. By alloying of Mo with elements like Al, Ti, Nb or others, a further improvement of the oxidation and corrosion resistance of the thin films can be achieved [3,9,10].

Another promising class of materials in the field of thin films are niobium oxides (NbO_x). Within the complex Nb-O system, as a result of the Nb charge states of 2+, 4+ and 5+, three different stable oxides are existing, namely niobium monoxide NbO, niobium dioxide NbO_2 and niobium pentoxide Nb_2O_5. Besides, several stoichiometric and non-stoichiometric (metastable) phases and polymorphs are known in the Nb-O system [11]. NbO, which is a metallic material, shows superconductive properties at temperatures < 1.38 K, while NbO_2 is a blue coloured oxide, showing a semiconductor-metal transition at elevated temperatures [11,12]. Nb_2O_5 is the thermodynamically most stable phase, covering several temperature dependent polymorphs, like the TT-, T-, M- and H-phases,

but can also exist in an amorphous state. The amorphous, dielectric Nb_2O_5 is transparent in the visible light range with a high refractive index, making it usable for optical thin film applications like optical interference filters [11–15]. In addition to these optical applications, NbO_x are applied as capacitors, oxygen sensors, corrosion resistant materials and biocompatible coatings [14–16].

To deposit the above mentioned Mo-based and NbO_x thin films, physical vapour deposition, or more precisely d.c. magnetron sputtering, is often the technique of choice. With film thicknesses ranging from a few nm up to µm and substrate sizes up to large glass panels used for architectural glass, magnetron sputtering is a multifarious thin film process. The films deposited can be single-element or alloyed metallic films, if the deposition is carried out in an inert atmosphere, as well as compound films in case of a reactive deposition. Here, compounds (like oxides) are formed by the reaction of the sputtered elements with the reactive gas atmosphere [17]. Alloying of films during deposition can be performed by co-sputtering of single-element targets. There, two or more single-element targets are sputtered simultaneously, leading to a mixture of the sputtered atoms and the formation of a homogenous, alloyed film [18]. Alternatively, alloying can also be performed by sputtering from an alloyed or a compound target, consisting of two or more elements within one target. During sputtering, a flux of atoms is ejected from the target surface with a composition identical to the target composition, forming again a homogenous, alloyed film [18].

The manufacturing of such alloyed or compound targets can be carried out by cold gas spraying (CGS), a novel thermal spray technique. There, a dense and solid thick coating is deposited by accelerating a metallic powder or powder mixture in a high velocity gas jet. The powder particles are not getting melted or thermally softened prior to the impact onto the substrate. Deposition only occurs by the plastic deformation of solid particles. Due to the high kinetic energy of the powder particles and respective low gas temperature of a maximum of 1000°C, the oxygen content within the coatings is low, since no oxidation or phase transformation occurs during spraying. Thus, thick CGS coatings are a potential candidate for the use as sputter targets [19–22].

Within the present work, CGS was used for the manufacturing of laboratory-scale planar as well as industrial-scale cylindrical rotatable sputter targets. The chemical

compositions of the cold sprayed targets cover both, single-element targets made of Nb and multi-element compound targets made of MoAl, MoAlTi and MoNb. Investigations were carried out on the preparation of multicomponent targets by CGS, the influence of sputtering parameters like the Ar gas pressure on the chemical composition of the alloyed films due to changes occurring during the gas phase transport from the target to the substrate and differences in the element specific gas phase scattering. In addition, the evolution of thin film microstructure and properties, in particular electrical resistivity, oxidation resistance and wet etching behaviour, has been analysed. Further, a comparison between the sputter behaviour of Nb CGS targets and commercially available, sintered Nb targets during reactive magnetron sputtering was established.

2. SPUTTER DEPOSITION

Magnetron sputter deposition represents a typical thin film deposition technique within the group of physical vapour deposition (PVD) methods. Physical sputtering is the non-thermal vaporization of a target material, followed by the transport of the vapour from the target towards a substrate and finally the condensation of the vapour on the substrate [1,17]. With the high variety of materials possible to be deposited by magnetron sputter deposition, it is an established process of choice in many different applications. Examples are optical coatings used for mirrors or architectural glazing, wear-, erosion-resistant or tribological coatings for cutting tools, corrosion-resistant coatings and functional thin films used in flat panel displays and microelectronics [17,23,24].

2.1. Physical basics

Sputter deposition is one of the most frequently used techniques for deposition of thin films onto a substrate. Sputtering itself is based on the bombardment of a target surface by energetic charged particles, which are accelerated by an electric field, leading to a number of processes on the target surface, as shown in Figure 1. Some of the energetic particles, usually ions originating from a gas discharge, penetrate the target surface region (depending on their initial energy to depths between 1.5 and 15 nm [18]), creating a collision cascade, where some of the momentum is transferred to the surface atoms. These atoms may be ejected (“sputtered”) from the surface and may condense on a substrate as thin film. Other ions bombarding the surface can be neutralized and reflected or implanted into the near surface region, as can be seen for the squared symbols in Figure 1. To describe the efficiency of the sputtering process, the sputter yield can be used. The sputter yield corresponds to the number of ejected atoms per incident ion. It depends on the energy of the incident ions, their mass, the mass of the target atoms as well as the surface binding energy of the target atoms. The most common form of sputtering is the plasma assisted sputtering, where positive ions, like Ar^+, are accelerated towards the target, which is at negative potential with respect to the plasma. The ionization of the Ar atoms takes place by inelastic collision with

electrons. Secondary electrons, generated by the Ar^+ bombardment of the target surface, are able to further increase the ionization of the Ar atoms [1,2,17,18].

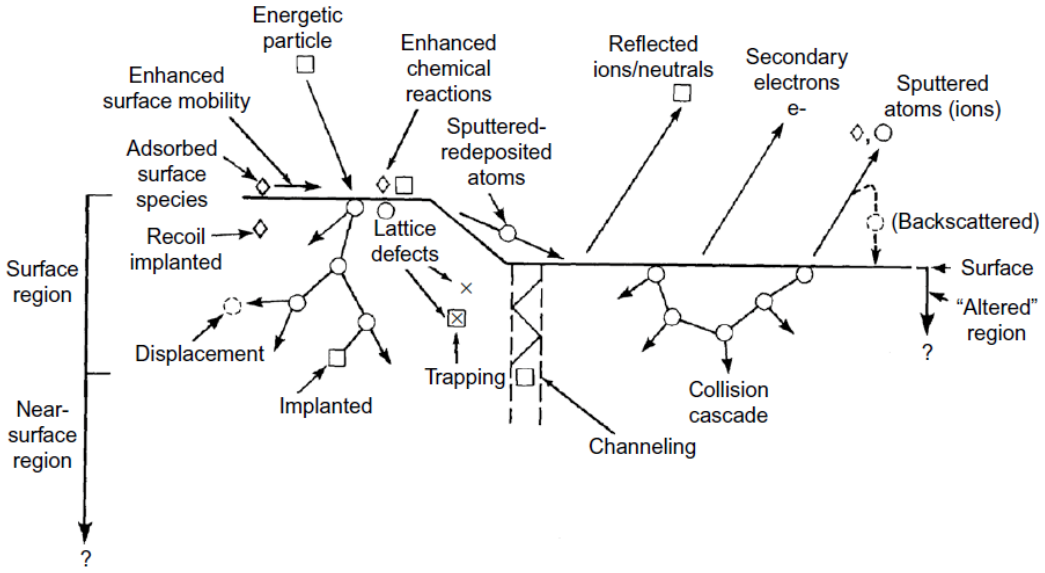

Figure 1: *Interaction of energetic particles bombarding a surface [17].*

2.2. Direct current diode sputtering

The principle of sputtering, as described in section 2.1., can essentially be applied using a d.c. diode sputtering system, which represents the basis of other sputtering systems like d.c. magnetron sputtering. The sputtering system, evacuated to pressures in the high or ultra-high vacuum range (10^{-3} – 10^{-7} mbar), consists of two planar electrodes. The cathode, which acts as the target, is connected to a negative voltage of several thousand volts, whereas the substrate holder represents the anode. In the simplest case, the anode is grounded. By applying an Ar gas pressure of > 1.3 Pa (> 10 mTorr [17]), which acts as the working gas, and a d.c. voltage of -2 to -3 kV to the cathode [23], the gas discharge can be initiated. Electrons are accelerated away from the cathode, bombarding the substrate and the surface of the vacuum chamber, resulting in undesired heating, whereas a few electrons collide with Ar atoms to create additional ions by inelastic collisions. The cathode material is limited to electrically conductive materials, since for an insulating material a positive surface charge develops, preventing

further ion bombardment. Due to several limitations like the low ion current density and thus low sputtering rate plus the effect of substrate heating, d.c. diode sputtering is nowadays very rarely employed in production environments [17,18,23,25].

2.3. Magnetron sputtering

A schematic representation of a planar magnetron sputtering system is displayed in Figure 2, with one permanent magnet positioned in the target centre and a ring of magnets on the outer edge of the target [18]. The installation of the magnets on the target reverse side applies a magnetic field B parallel to the target surface. This magnetic field forces the secondary electrons, emitted during ion bombardment of the target, to stay on a circulating closed path near the target surface. This leads to a high flux of electrons, increasing the ionization efficiency of Ar atoms, creating a high density plasma. The region of the most intense plasma can be named as the so-called “racetrack”, where the electric field E and the magnetic field B are perpendicular to each other and thus form a maximum of the Lorentz force, providing an effective confinement for electrons [1,17,18,25]. With the now higher sputtering rate, the deposition rate at the substrate is also increased, whereas at the same time undesired heating of the substrates by electron bombardment is significantly reduced. Additionally, the higher ionization efficiency enables a sputtering process performed at lower target voltage as well as lower Ar gas pressure, preventing scattering and thermalization of the sputtered atoms during the gas phase transport towards the substrate [23,25].

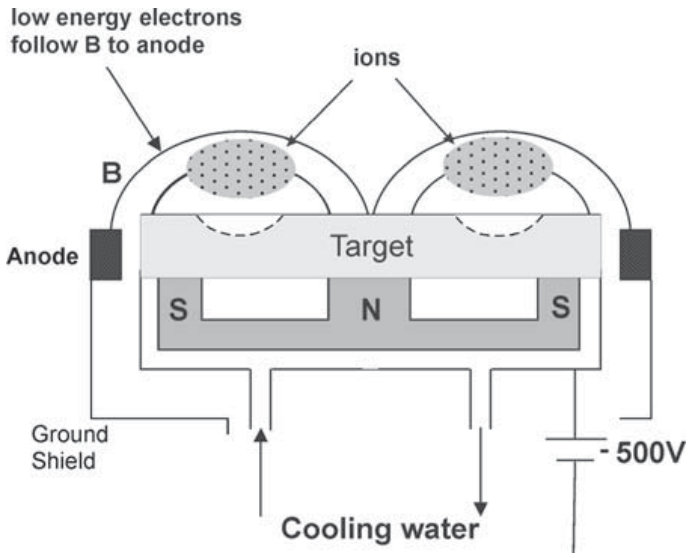

Figure 2: *Schematic representation of a planar magnetron with the indication of the magnetic field lines, the most intense plasma region as well as the formation of the target racetrack [18].*

A possible disadvantage of this conventional "balanced" arrangement of the magnetrons is, that the plasma is limited to an area near the target, making it unavailable to activate reactive gases in the plasma near the substrate to perform reactive magnetron sputtering [17,25]. By strengthening the inner pole relatively to the outer pole (type 1) or the outer pole relatively to the inner pole (type 2), unbalanced magnetron sputtering can be established, as can be seen in Figure 3. In both cases the magnetic field lines are not closed. For type 2 unbalanced magnetron sputtering, which is the commonly used design, some magnetic field lines are directed towards the substrate which limits the plasma not only to the near target region. Additionally it has been mentioned, that with the type 2 configuration the substrate ion current density can be roughly an order of magnitude higher than in the balanced configuration. The changed shape of the magnetic field lines allows electrons to escape the magnetic trap and follow the field lines towards the substrate. The increased electron flux and thereby the also increased ion flux deliver more energy to the substrate, which can support thin film growth [1,17,23,25].

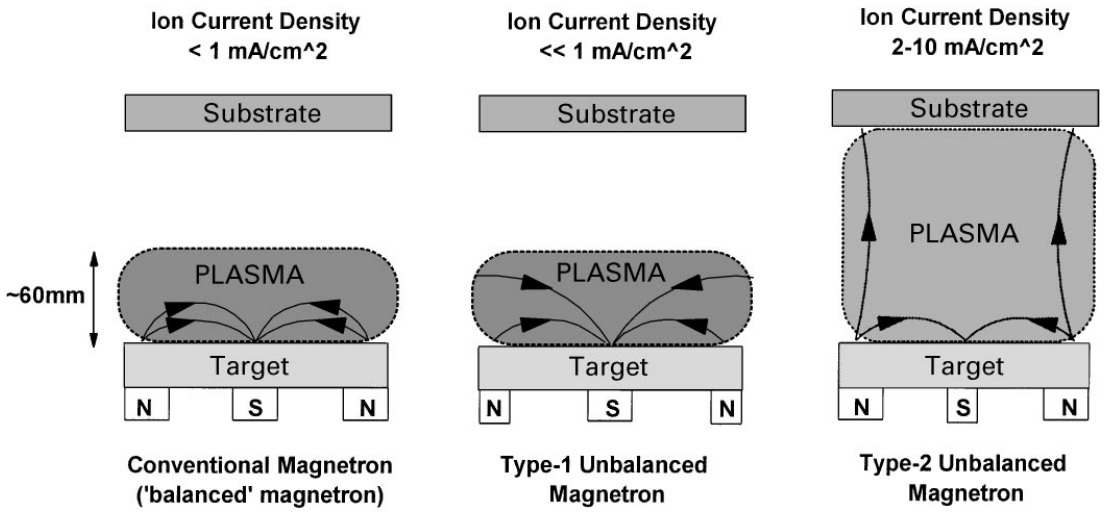

Figure 3: *Configuration of a conventional balanced planar magnetron plus the configuration of type 1 and type 2 unbalanced planar magnetrons [23].*

2.4. Cylindrical rotatable targets

The formation of a racetrack on the surface of a planar target leads to an inhomogeneous material removal and to the formation of sputter erosion tracks. Within this erosion track the targets thins out, while areas beside stay largely untouched. As a consequence the target material utilization is only between 30 and 40 % [24,26]. One way to improve the target utilization was the development of rotatable cylindrical targets in the early 1980's and their industrial use since the 1990's [24,27,28]. There, the sputter target, displayed in Figure 4, is a cylindrical tube rotating around a stationary magnetron configuration with a magnetic field line design similar to planar magnetrons [1,24]. Due to the rotation, continously new target surface gets exposed to the plasma, leading to uniform sputter erosion and significantly increased target utilization, reaching 75 – 90 % without the localized formation of erosion tracks. The uniform erosion also results in a continuous and homogeneous change of the effective magnetic field at the target surface over target lifetime [1,24,27,28]. Because of the more efficient cooling by the water inside the target tube (see Figure 4), higher power densities can be used for cylindrical rotatable targets compared to planar targets. The increased sputter power results in an increased deposition rate and consequently decreased process time [24,28]. The more complex target design and the more elaborate fabrication are the drawbacks of cylindrical rotatable targets, limiting the availability of target materials or

necessitating alternative manufacturing routes, like thermal spray techniques such as cold gas spraying, described in section 4 [1,27]. Nevertheless, cylindrical rotatable targets find a wide field of applications, mainly in large area depositions like web coatings, flat panel displays, photovoltaic solar cells and architectural glass coatings [28,29].

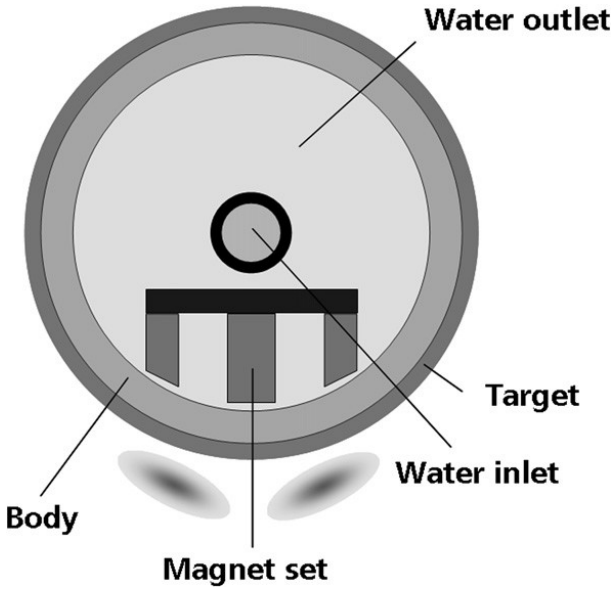

Figure 4: *Cross-section of a cylindrical rotatable magnetron sputter system [24].*

2.5. Reactive magnetron sputtering

By sputtering from a pure metallic target with the presence of a reactive gas, reactive magnetron sputtering can be performed. Typically reactive gases, which are added to the inert Ar working gas, are O_2, N_2, CH_4 or CF_4, as well as mixtures of the named gases. Therefore, a large number of different compound films can be deposited like oxides, nitrides, oxy-nitrides, carbides and fluorides, which are found in a large number of applications (e.g. hard coatings for cutting tools, optical films, decorative coatings, thin films for micro-electromechanical systems or transparent conductive oxides) [2,18,30,31]. A characteristic of reactive magnetron sputtering is the existence of two different sputtering modes: (*i*) the metallic mode at low reactive gas partial pressures and (*ii*) the poisoned mode at high reactive gas partial pressures. These two modes are

separated by a transition region which shows a hysteresis behaviour, as indicated by Figure 5. In the area A to B, the reactive gas is gettered by the sputtered atoms, yielding a constant reactive gas partial pressure. Without the presence of a discharge, the reactive gas partial pressure would increase linearly, as shown by the dashed line in Figure 5 (b). At point B, the number of reactive gas atoms is equal to the number of sputtered atoms gettering them. The further increase of the reactive gas flow leads to the formation of a compound on the (metallic) target surface freshly exposed to the reactive gas, significantly decreasing the sputter rate of the metal atoms from the target. Therefore, a lower flux of metal atoms is available at the substrate to react with the reactive gas, drastically decreasing the deposition rate. During this poisoned mode (area C to D), where the whole target surface is covered by the compound, the deposition rate stays constant at low values with an at the same time linearly increasing reactive gas partial pressure. In the subsequent decrease of the reactive gas flow (D to E), the return to the metallic mode is delayed until all of the compound is removed from the target surface and only metal atoms are sputtered again (F), completing the hysteresis [2,18,30].

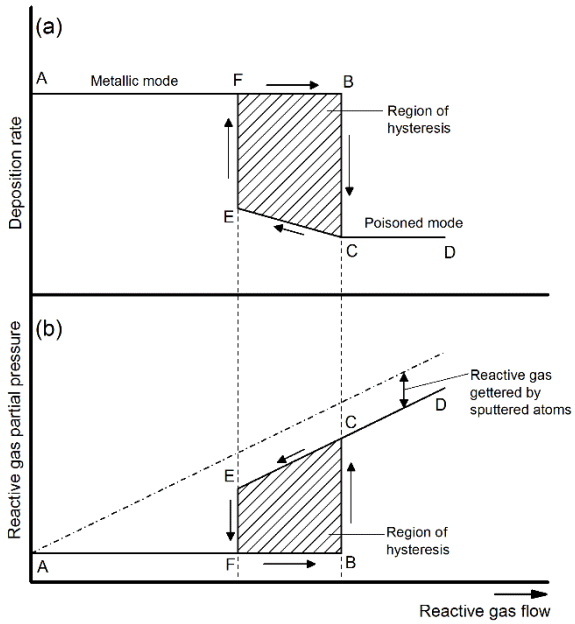

Figure 5: *Outline of (a) the deposition rate and (b) the reactive gas partial pressure as a function of the reactive gas flow during reactive magnetron sputtering, redrawn after [2,30].*

2.6. Sputter deposition of multicomponent films

A number of scientific contributions covering different aspects of the deposition of multicomponent films grown by sputtering from multicomponent sputter targets have been published. Examples include material systems like W-Ti [32–34], Ti-B [35], Zr-B [36], Al-Cu [32] and Mo-Al [37]. A similarity of these films is the deviation of the chemical composition of the films with respect to the chemical composition of the targets.

During sputtering of a virgin multicomponent target, where bulk diffusion within the target can be neglected due to the low target temperature, surface atoms possessing a high sputter yield are initially preferentially sputtered. This leads to a depletion of the high sputter yield elements on the target surface and to a decrease of their sputter rate, while the sputter rate of low sputter yield elements increases. This balance between the two element types continues until a steady-state is reached; then the composition of the flux of sputtered atoms leaving the target surface is identical to the composition of the target. Steady-state can be typically achieved within the first 100 - 200 atom layers sputtered, depending on sputter rate and Ar ion energy, which usually occurs within the first few seconds of sputtering [2,18].

During the transport phase from the target to the substrate, collisions between the sputtered atoms and gas atoms occur. In case of a multicomponent system, in particular with a pronounced mass difference between the sputtered species, element specific scattering can lead to a shift in the chemical composition of the flux with respect to the target. Lighter elements are scattered more efficiently and undergo a more efficient thermalization during collision with the Ar background gas, which can be expressed by the energy transfer coefficient ε [1,18,32,34,35].

$$\varepsilon = \frac{4\, m_1\, m_2}{(m_1 + m_2)^2} \qquad (1)$$

If a collision occurs, the sputtered atom shares its momentum with the gas atom and loses a certain amount of energy and gets deflected at a certain angle. ε, and therefore the energy loss, gets maximized when the mass of the gas atom (m_1) is similar to the

mass of the sputtered atom (m_2). Heavy elements loose only a small fraction of their kinetic energy and deflect only slightly, retaining their initial direction towards the substrate, whereas lighter elements scatter through a large angle. Additionally, heavy elements need a higher number of collisions until they are finally thermalized [18].

The influence of the background gas pressure on the gas phase transport of alloys has been described by Rossnagel et at. [32] and Bundaleski et al. [34]. There, the gas phase transport is characterised by three different regimes. At low pressure conditions hardly any collisions between sputtered atoms and gas atoms appear, which leads to a film composition similar to the target composition. This regime is called the ballistic regime. An increase of the pressure causes a shift towards the intermediate regime. There, in case of a mass difference of the sputtered elements, the lighter ones are now scattered more rapidly. The film composition with respect to the sputter target shifts towards the heavier element. With a further rise of the pressure, the gas phase transport becomes more diffusive. In this so called diffusive regime the heavier elements are also slowed down and scattered effectively, which should lead to a rise of the fraction of lighter elements, approaching again the original target composition.

Apart from that, condensation and diffusion effects occurring on the surface of the growing film are also able to influence the chemical composition of a multicomponent film. Condensation is on the one hand governed by differences in the sticking coefficient of the individual species, on the other hand by preferential re-sputtering due to energetic particles, like energetic neutrals or ions [33,35]. Differences in the sputter yield and the energy transfer coeffcient (see Eq. (1)) during re-sputtering can cause a shift in the chemical compostion of multicomponent films. The diffusion of atoms depends on their surface mobility, which gets increased by the atom energy and thermal energy originating from the substrate temperature. Differences in the diffusivity may cause self-shadowing effects and the formation of lower density films (see also section 3.2) [18].

3. THIN FILM GROWTH

Thin film deposition and growth usually takes place far from thermodynamic equilibrium. Low temperatures during deposition of 0.2-0.3 T_m, where T_m is the melting point of the deposited material in Kelvin, enables formation of metastable phases as well as the evolving of a microstructure in a competitive fashion [38]. The growth process is typically characterised by different stages such as nucleation, island growth, coalescence of islands, formation of polycrystalline islands, the development of a continuous structure and finally film growth [1,39].

3.1. Nucleation and island growth

The initial stage of thin film growth, i.e. the nucleation stage, is visualized in Figure 6 together with the development of the 3D island growth and 2D layer growth stages. A flux of atoms with energies between 5-10 eV arrives at the substrate either condensing from the gas phase, becoming so-called adatoms, getting immediately reflected back to the gas phase or re-evaporating. Condensed adatoms are able to diffuse on the substrate surface and to interact with other adatoms. Their mobility depends on the energy of the initial atom, the chemical bonding to the surface as well as the substrate temperature and can be increased by a low energy ion bombardment during deposition [1,17]. Preferred nucleation sites for adatoms can be substrate lattice defects, atomic steps and impurities, where they form stable nuclei (clusters of adatoms) by collision with other adatoms. The nuclei form 3D islands or 2D layers by capturing more adatoms as illustrated on the right hand side of Figure 6. To grow a dense film the number of nuclei per surface unit, the nuclei density, should be high [17].

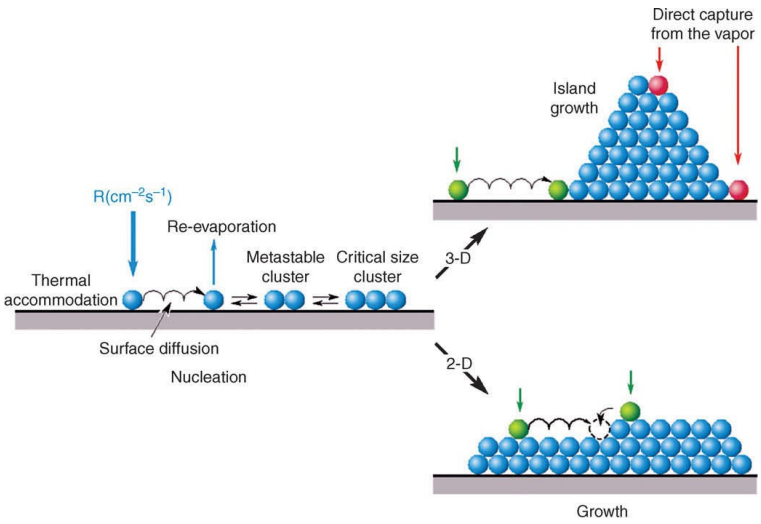

Figure 6: *Schematic representation of the nucleation process and the 3D island growth and 2D layer growth [1].*

As already indicated in Figure 6, the outline in Figure 7 shows the three different modes of film growth, which depend on the interaction between the adatoms and between the adatoms and the substrate surface. During the island growth, or Volmer-Weber type growth, adatoms supply to islands by surface diffusion, since the adatoms are more strongly bonded to each other than to the substrate. The islands grow laterally until they coalescence, forming a continuous film. An opposite bonding characteristic can be found in the layer growth type, the Frank-van der Merwe type growth. Here the atoms are more strongly bonded to the substrate, building a complete monolayer which is then covered by another monolayer. The third mode, the Stranski-Krastanov type growth mode, can be described by a mixture of the two other modes. After the formation of one or several monolayers, the subsequent formation of layers becomes energetic unfavourable leading to the formation of islands. Except single-crystal epitaxial growth of semiconductor films growing by the Frank-van der Merwe type growth, film growth takes place by island formation in nearly all practical cases of films nucleating on substrates with different composition or microstructure [1,2,17,25].

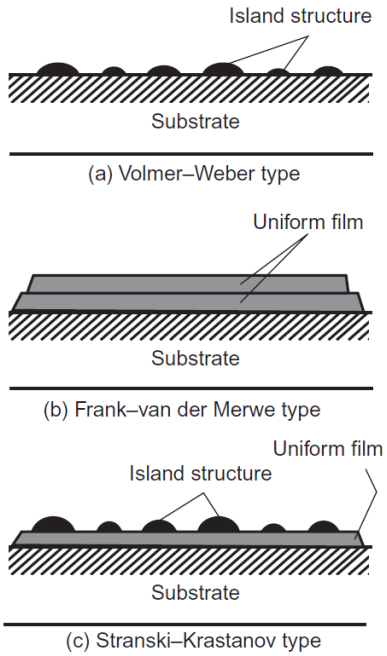

Figure 7: *Outline of the three different modes during thin film growth [2].*

3.2. Structure zone models

A multitude number of studies have been performed to correlate the polycrystalline film structure with the applied deposition conditions. Structure zone models (SZM) have been developed and refined to categorize the structural evolution during thin film growth as a function of the deposition parameters [1,17,38,39]. Figure 8 shows exemplary the SZM for the substrate temperature T_s, with respect to the melting temperature T_m of the film material (the so-called homologous temperature), and the film development over the film thickness. This SZM consists of three different zones. Zone I at low deposition temperatures ($0 < T_s/T_m < 0.2$), where no bulk or surface diffusion are recognisable, is characterised by the formation of small crystalline fibres. The underdense films grown under these conditions preserve the random orientation of the islands formed during nucleation and due to atomic shadowing the film shows an extensive porosity. Within the transition Zone T ($0.2 < T_s/T_m < 0.4$), surface diffusion becomes important. During this stage the grains show coarsening during island coalescence, but no grain boundary mobility within the continuous film. The adatom surface diffusivity enables the competitive growth of different grain orientations and therefore a change in morphology, texture and topography with increasing film

thickness. Near the substrate, the small grains formed show a random orientation out of which the V-shaped columns grow. Grains with favourite orientations overgrow kinetically disadvantaged columns, yielding a columnar grain structure in the upper film part. For still higher temperatures (T_s/T_m > 0.4), in Zone II, bulk diffusion becomes considerable, leading to grain boundary mobility throughout the whole film growth process. With large grains growing at the expense of small or unfavourable oriented grains, the total grain boundary area as well as the interface and surface energy gets minimized. Zone II films are characterised by a homogeneous, columnar structure over the film thickness with grain boundaries perpendicular to the substrate surface [1,17,38,39].

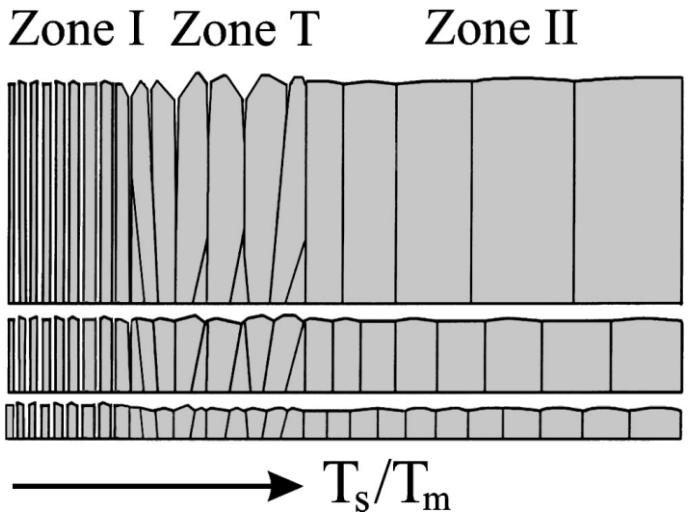

Figure 8: *Microstructural evolution during thin film growth as a function of the homologous temperature and film thickness [38].*

4. COLD GAS SPRAYING

The cold gas spraying (CGS) process is the youngest process within the technical field of thermal spraying. It was originally developed in the middle of the 1980's at the Institute of Theoretical and Applied Mechanics of the Siberian Branch of the Russian Academy of Science in Novosibirsk, Russia, during studies of a supersonic two-phase flow in a wind tunnel. The subsequent publication of a various number of US and European patents in the 1990's focused on the development of cold spray equipment and technologies. Increased research activities and production efforts all over the world in the last decade consider the CGS process a strong potential and particular attention within the scientific community and industry [40–43]. Within the current work, CGS has been used for the manufacturing of single-element (Nb) and multi-element (MoAl) planar sputter targets as well as the manufacturing of multi-element (MoAlTi) cylindrical, rotatable sputter targets.

4.1. Technical basics

The main principle of CGS is the deposition of a dense and solid coating by accelerating a metallic powder feedstock in a high-velocity gas jet, with the particularity that the metallic powder particles are not getting melted or thermally softened prior to the impact onto the substrate [21,22,42]. Figure 9 shows a classification of CGS in accordance with the gas jet temperature and the particle impact velocity, compared to other thermal spray processes like flame spraying or air plasma spraying [22]. Depending on various types of parameters like the nozzle geometry, particle type, size and shape, or the temperature and pressure of the process gas, the particle impact velocities for CGS range typically between 200 and 500 m/s, but can even reach 1200 m/s. With a gas jet temperature typically not surpassing 1000°C, the particle impact temperature can range between room temperature and 800°C. These comparatively low temperatures enable cold spraying of most metals but also metal-base alloys which are sensitive to oxidation [19,20,22,44].

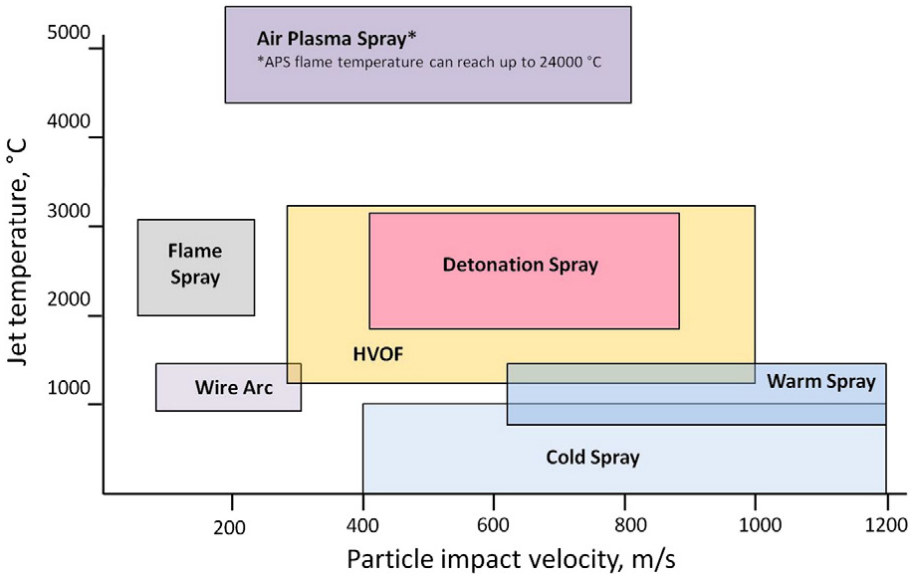

Figure 9: *Range of the gas jet temperature and particle impact velocity for CGS compared to air plasma spraying (APS), flame spraying, detonation spraying, high velocity fuel oxygen spraying (HVOF), wire arc spraying and warm spraying [22].*

A schematic representation of a CGS system is displayed in Figure 10. The employed high pressurized gas, with pressures of up to 60 bar, is typically nitrogen but also helium or air can be used. The gas stream gets divided into the process gas stream and into the carrier gas stream. The process gas stream flows through a gas heater and afterwards streams into the prechamber of the spraying nozzle. The unheated carrier gas is transported through the powder feeder, where it is evenly charged with metallic particles to be sprayed. In the following, the charged stream enters the nozzle prechamber, where it recombines with the heated process gas stream. The nozzle is a de Laval type nozzle, which is characterised by a cross-section initially decreasing down to typically ø 2.7 mm in the narrowest point and the subsequent enlargement of the diameter. Thus, supersonic gas and particle velocities can be achieved. Spraying is performed onto a substrate, which is located at a distance of 20 - 60 mm in front of the nozzle [19,21,42].

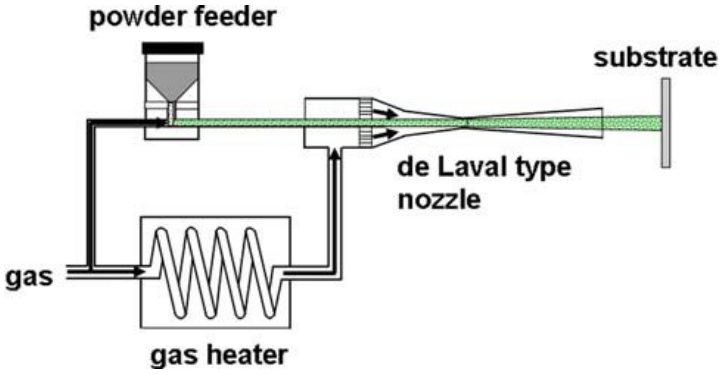

Figure 10: *Schematic representation of a CGS spraying system [19].*

With the above mentioned design, the powder particle injection into the de Laval nozzle is performed in the subsonic part, the prechamber, of the nozzle. The subsonic injection is characterised by an intense heat exchange of the powder particles with the process gas, leading to an increased particle impact temperature at the substrate and to an increased particle velocity. However, it is necessary to keep the stagnation pressure of the carrier gas stream higher than the static pressure inside the nozzle prechamber and thus high pressure powder feeders have to be utilised. Additionally, hard abrasive particles are able to erode the nozzle wall in the throat. In a second method, the powder particles can be injected into the diverging, supersonic part of the nozzle, as displayed in Figure 11. There, excessive erosion can be avoided but the particle impact temperature and velocities are significantly lower. Due to the injection of particles in a supersonic gas stream, strong perturbances may occur by arising shock waves leading to a considerable loss in stagnation pressure and gas velocity [22,45].

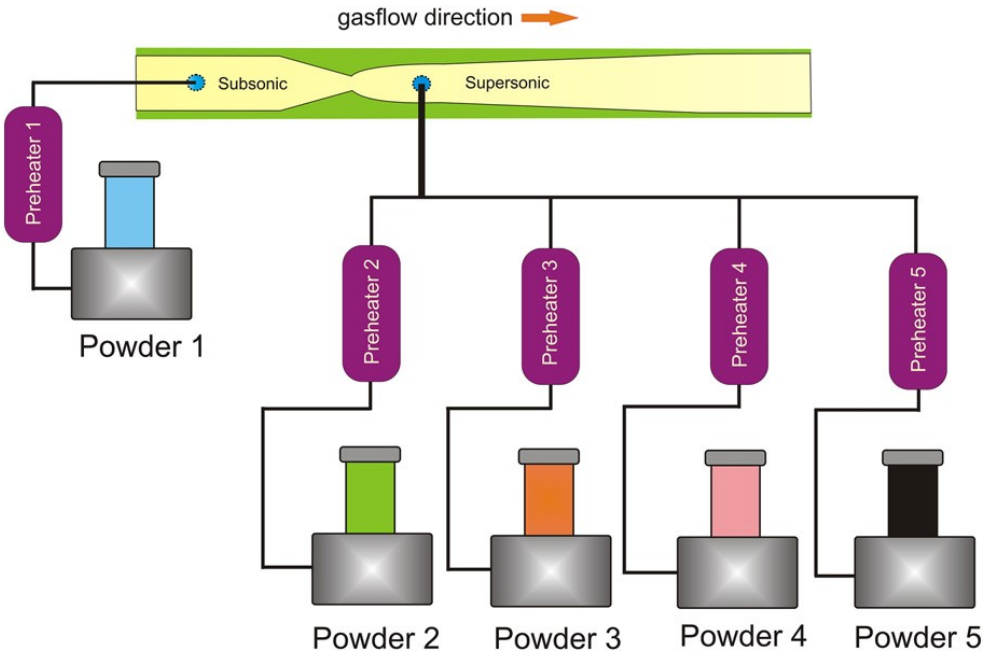

Figure 11: *Outline of a de Laval type nozzle with subsonic and supersonic particle injection points [22].*

Future trends and applications of CGS can be found in the spraying of composite coatings with several compounds within the coating, reaching specific functional properties like wear and corrosion resistance or specific electrical conductivity, to name a few [45]. Figure 12 illustrates three possibilities for the spraying of composite coatings by CGS. First, the deposition of a powder mixture by applying two or more powder feeders leads to a uniform distribution of the components within the coating. With the use of commercially available powders, this approach is characterized by low costs and the formation of a composition gradient across the coating thickness is feasible by adjusting the powder feeding rate of the single components. In the second approach, displayed in the middle of Figure 12, a preliminarily prepared composite powder, consisting of micro- or submicron sized grains, is used. The application of such powder leads to a higher level of homogeneity for the component distribution within the coating. However, due to the changed deformation behaviour of the composite particles, a successful spraying and deposition can be more challenging. Additionally, changes in the chemical composition over coating thickness are not possible. For the last, more innovative approach shown on the right-hand side of Figure 12, cladded or

coated powder particles are applied. There, typically hard particles are cladded by a soft thin material which enables the binding of the particles on the substrate [22,45].

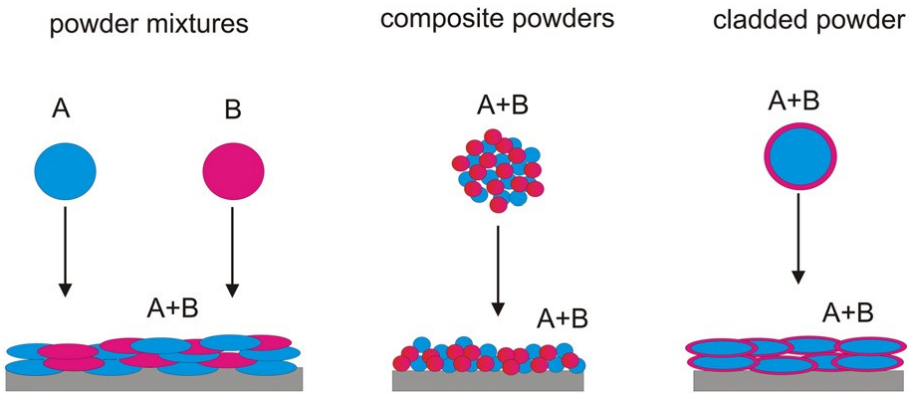

Figure 12: *Different approaches for the deposition of composite coatings by CGS [22].*

4.2. Bonding mechanisms in CGS

In view of the successful formation of a coating by the collision of solid particles with the surface of a substrate, fundamental and interesting questions concerning the bonding mechanisms are not yet fully understand. Likewise, it is not yet clear, if the particle impact just leads to plastic deformation or if also recrystallization takes place. Further thermal softening or even partial melting may occur due to kinetic to thermal energy transition [21]. An often mentioned term for bonding of the particles is adiabatic shear instability [19–22,46]: When the collision between particle and substrate occurs, the pressure gradient between the two interfaces generates a shear load, accelerating the material laterally, which causes a localized shear straining. In case of a high enough pressure gradient and deformation, these shear strains can lead to adiabatic shear instability. As a result, thermal softening is dominating locally over strain and strain rate hardening followed by a discontinuous jump of strain as well as temperature and a direct breakdown of stress. A viscous flow is generating an out-flowing materials jet with temperatures close to the materials melting temperature. The heated surfaces are thus bonded together. A simulated impact of a 25 µm Cu particle onto a Cu substrate is displayed in Figure 13 for two time sections, showing the resulting strain fields.

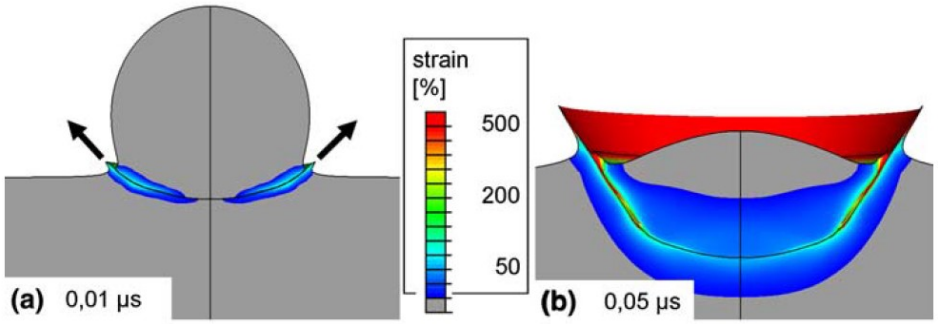

Figure 13: *Strain fields during impact of a single 25 µm Cu particle onto a Cu substrate for two time sections [19].*

The particles themselves must provide a sufficient ductility to build up a dense coating and to withstand the intense plastic deformation. Additionally, the materials cooling rate is mentioned as one important factor for bonding, which should be low enough to enable adiabatic shear instability but high enough to complete the bonding process [20]. Beside adiabatic shear instability, mechanical interlocking and metallurgical bonding are also considered as two mechanisms for the bonding in CGS coatings [21,22].

To undergo this intense plastic deformation of the sprayed particles, their velocity has to exceed a certain critical value, the critical velocity v_{crit} [19,22,40,42,46]. It is defined as the velocity where the deposition efficiency, i.e. the amount of particles adhering to the substrate compared to the amount of particles sprayed, reaches 50%. One possibility for the calculation of v_{crit} based on numerical analysis, dependent on materials properties as well as CGS parameters, has been described by Assadi et al. [46] with a simple empiric formula:

$$v_{crit} = 667 - 14\,\rho + 0.08\,T_m + 0.1\,\sigma_u - 0.4\,T_i \qquad (2)$$

There, the critical velocity v_{crit} decreases with the density ρ (in g/cm³) and the particle impact temperature T_i (in K), but increases with the melting temperature T_m (in K) and yield stress (in MPa) of the sprayed material. However, this formula does not consider other particle properties, like the particle grain size. A variation in grain size and surface to volume ratio influences v_{crit} due to the length scale of heat conduction and due to the

size dependent strain rate hardening [20]. Figure 14 displays critical velocities of different materials with a particle size of 25 µm, showing wide variations between ~150 m/s for Pb and nearly 900 m/s for Ti and Mg.

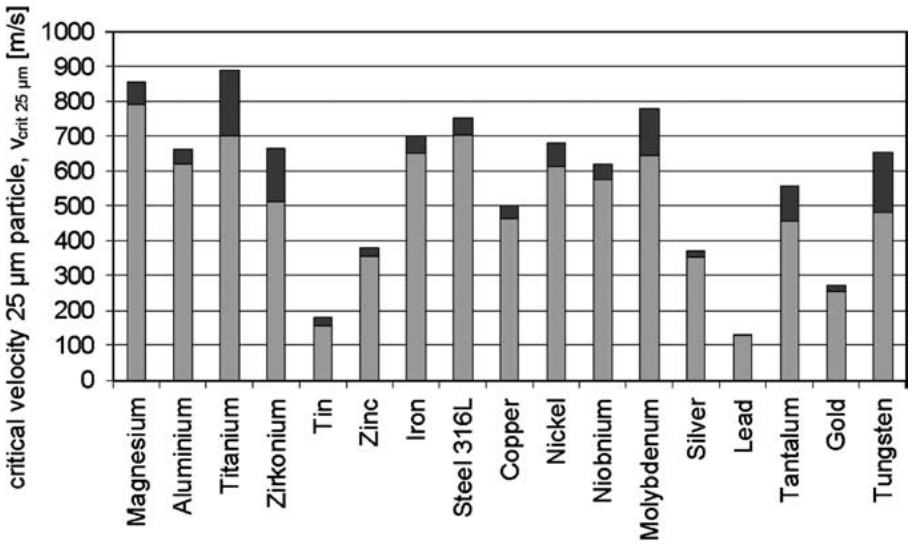

Figure 14: *Calculated critical velocity v_{crit} for 25 µm particles for different materials [20].*

The development of gas and particle velocity, as well as the gas and particle temperature along the distance from the de Laval nozzle throat are displayed in Figure 15 and described by van Steenkiste et al. [21] and Schmidt et al. [19]. Small particles with a size of 1 µm are able to nearly reach the gas velocity, while with increasing particle size the velocity is lowered. Acceleration in a gas stream takes place by drag, where larger, and therefore heavier particles, behave more slowly. With an increasing gas temperature the gas density is changed, which affects the drag force on the particles leading to an increased particle velocity. Particles heat up before reaching the nozzle throat, i.e. the smallest cross-section of the nozzle. After passing this section, they cool down again due to the working gas expansion within the nozzle. Small particles with sizes up to 10 µm attain the gas temperature before reaching the nozzle throat in the example displayed in Figure 15, but show a significant temperature drop afterwards. Both can be explained by the low thermal inertia of these small particles. Mid-size particles of 20 µm and large particles of 50 µm are heated more moderately, however their temperature profile stays also more constant leading to the highest particle impact temperatures.

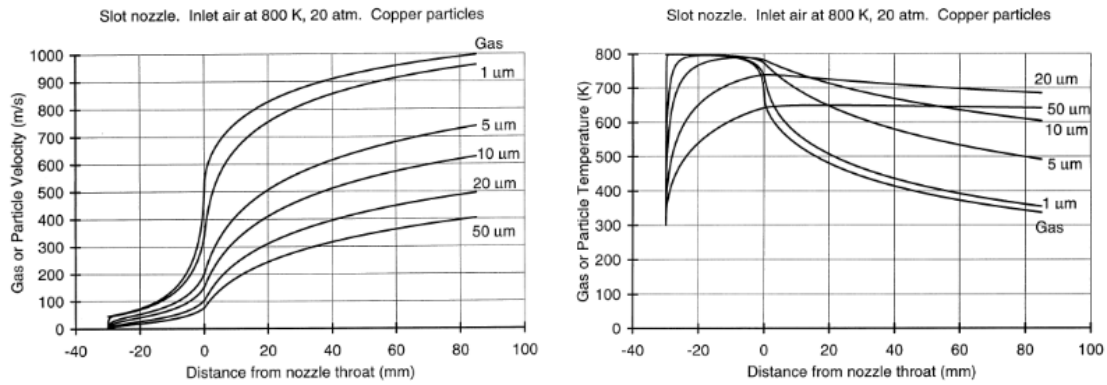

Figure 15: *Computed gas and particle velocity and temperature for various particle sizes as a function of the distance from the nozzle throat [21].*

4.3. CGS coating properties

Thermal spraying of materials which are sensitive to oxidation such as Mo, Nb, Ti or Al can be difficult due to the increased temperatures and therefore accelerated oxidation. For CGS with its significantly lower temperature working area and typically inert working gas, oxidation can be almost completely avoided. Usual oxygen contents reported are in the range of or even below the powder feedstock oxygen content. Additionally, possible thin particle surface oxide layers can be crushed and removed by the high velocity particle impact [19,21,41,47]. With the sprayed particles staying in solid-state and the low temperature, undesirable grain growth is also avoided during CGS. The powder feedstock grain size distribution usually is maintained within the sprayed coatings. Phase changes, like decompensation or the formation of metastable phases, are also not expected during cold spraying [41].

Cold sprayed coatings are characterized by a low porosity and respective high coating density due to the intense plastic deformation upon impact on the substrate. Any loosely bonded particles are removed by the spray jet and subsequent impinging particles shot peening the already coated surface, further increasing the coating density [21,41]. Typically mentioned density values for cold spray coatings are for example up to 98.5% of the Al bulk density [48] or 98.4% of the Nb bulk density [49]. Porosity values range between 0.1 and 1% for Fe, between 0 and 0.1% for Cu [21] and 0.3% for Nb coatings [50], while for plasma sprayed coatings porosities of up to 10% are possible

[44]. Figures 16 (a) to (c) show exemplarily light optical micrographs of CGS coatings prepared within this thesis, demonstrating the uniform particle distribution, the strong particle deformation and the formation of low porosity coatings for the systems Mo-Al, Mo-Al-Ti and Nb.

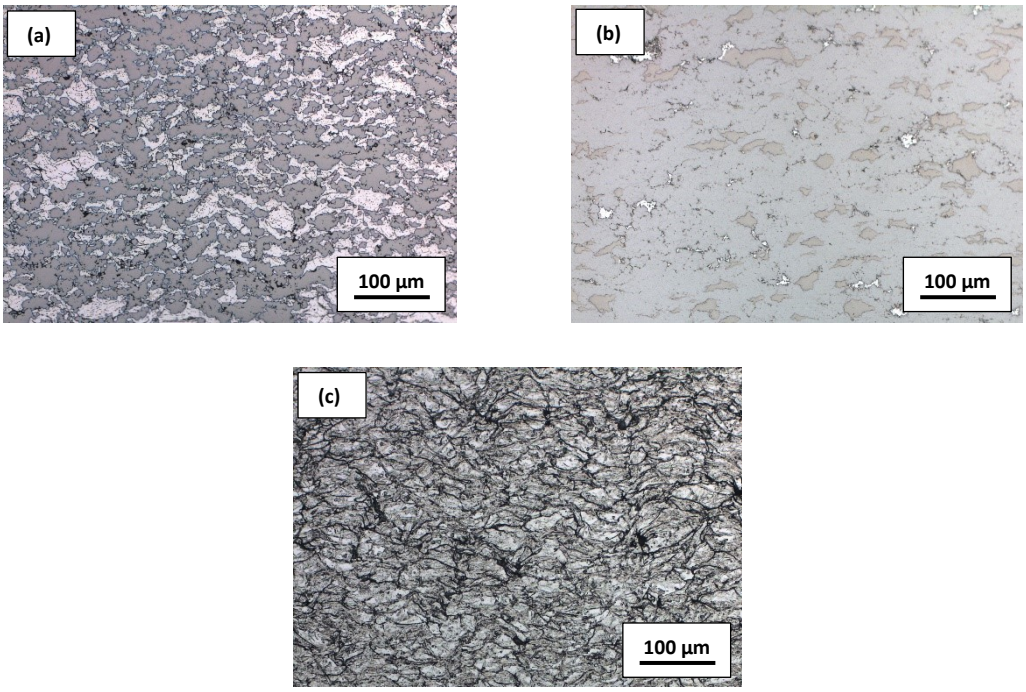

Figure 16: *Light optical micrographs of cold sprayed (a) Mo-Al, (b) Mo-Al-Ti and (c) Nb coatings (own work).*

Most thermal spray processes lead to tensile residual stresses within the coatings with possible bonding failures due to micro-cracking and deterioration of the coating performance. In CGS the residual stress profile consists of two sources, (*i*) thermal mismatch and (*ii*) deposition stress. Since CGS is performed above room temperature, a thermal misfit can occur during cooling down because of differences in the thermal expansion coefficient of coating and substrate. With a suitable choice of the substrate material and sample thickness, thermal stresses can be eliminated. The peening process with the high amount of plastic deformation is governing the residual stress profile with the formation of compressive stresses across the whole CGS coating thickness [41,48]. Possible locations for a coating failure can be found at the substrate/coating interface in case of a high stress gradient or weak interfacial bond strength. Figure 17 shows an

example of a residual stress profile of an Al CGS coating on Mg substrate. The absolute stress values are low, but significant differences can be seen at the substrate/coating interface position (through thickness position 0 in Figure 17), representing a potential risk for coating delamination [48].

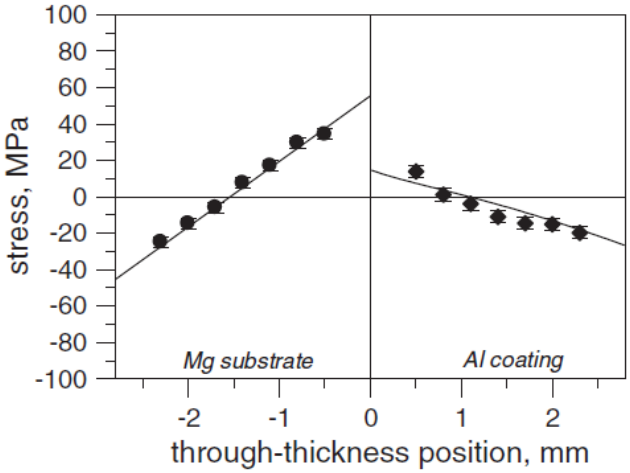

Figure 17: *Through-thickness stress profile of a CGS Al alloy (Al 6061) on a Mg substrate [48].*

5. SUMMARY AND CONCLUSIONS

Within the present thesis, cold gas spraying was used for the development and manufacturing of magnetron sputter targets based on refractory metals. The investigation focused on the preparation of thick cold sprayed coatings, the evaluation of the sputtering behaviour of cold sprayed targets and the development of thin film microstructure and properties. Cold gas spraying has proven a high flexibility in the manufacturing of sputter targets with respect to target shape and target alloying concept. Planar laboratory scale as well as industrial scale cylindrical, rotatable sputter targets have been successfully prepared. In addition, single-element as well as multi-element sputter targets have been fabricated. The targets are characterised by a uniform distribution of the sprayed particles and a low porosity, as exemplarily demonstrated for the Mo-Nb system. The use of single-element Nb targets during reactive magnetron sputtering indicated that the cold sprayed targets behave equivalent to commercially available sintered Nb targets. The deposited NbO_x films presented a comparable profile of properties, with an amorphous microstructure, an optical transparency shift with increasing oxygen partial pressure and the formation of Nb_2O_5 bonds. Variations of the Ar gas pressure during sputtering of multi-element Mo-based targets evidenced a strong influence on the chemical composition of the deposited films with respect to the chemical composition of the targets. The mass difference of the individual elements within the investigated Mo-Al-(Ti) targets leads consequently to a different scattering behaviour during collisions of the sputtered atoms with the gas atoms during the transport phase between target and substrate. An increasing Ar gas pressure, however, can further influence the chemical composition due to changes in the gas phase transport characteristics, changing from ballistic to diffusive. With the changed chemical composition, the properties of the films are also influenced, showing for example an increased oxidation resistance as the Al and Ti content in Mo-based films increases. Therefore, the Ar gas pressure allows the fine-tuning of the thin film properties by sputtering from a cold gas sprayed multi-element target.

With respect to future prospects for cold gas spraying and the manufacturing of sputter targets, potential approaches might be found in the expansion of the system diversity. Alloying concepts based on refractory metals other than Mo might be a first step, which should simultaneously include the improvement of the spraying process to enhance the deposition efficiency and therefore the efficiency for the target preparation compared to commercially available manufacturing routes. The number of elements within a multi-element cold gas sprayed target is also a factor which is not necessarily limited, just as the deposition of multi-element oxide or nitride films by reactive magnetron sputtering. In summary, cold gas spraying has proven its potential to break the chains of present target manufacturing routes in the design and alloying of sputter targets for the deposition of multifunctional thin films.

6. REFERENCES

[1] P.M. Martin, Handbook of Deposition Technologies for Films and Coatings: Science, Applications and Technology, 3rd ed., Elsevier, Amsterdam, Boston, 2010.

[2] K. Wasa, I. Kanno, H. Kotera, Handbook of Sputter Deposition Technology: Fundamentals and Applications for Functional Thin Films, Nanomaterials and MEMS, 2nd ed., Elsevier/Andrew, Amsterdam u. a., 2012.

[3] J.A. Shields, Applications of molybdenum metal and its alloys, 2nd ed., International Molybdenum Association IMOA, London, 2013.

[4] J.H. Scofield, A. Duda, D. Albin, B.L. Ballard, P.K. Predecki, Sputtered molybdenum bilayer back contact for copper indium diselenide-based polycrystalline thin-film solar cells, Thin Solid Films 260 (1995) 26–31.

[5] D. Rafaja, H. Köstenbauer, U. Mühle, C. Löffler, G. Schreiber, M. Kathrein, J. Winkler, Effect of the deposition process and substrate temperature on the microstructure defects and electrical conductivity of molybdenum thin films, Thin Solid Films 528 (2013) 42–48.

[6] T. Jörg, M.J. Cordill, R. Franz, O. Glushko, J. Winkler, C. Mitterer, The electro-mechanical behavior of sputter-deposited Mo thin films on flexible substrates, Thin Solid Films 606 (2016) 45–50.

[7] Y.-W. Yen, Y.-L. Kuo, J.-Y. Chen, C. Lee, C.-Y. Lee, Investigation of thermal stability of Mo thin-films as the buffer layer and various Cu metallization as interconnection materials for thin film transistor–liquid crystal display applications, Thin Solid Films 515 (2007) 7209–7216.

[8] A.M. Hofer, J. Schlacher, J. Keckes, J. Winkler, C. Mitterer, Sputtered molybdenum films: Structure and property evolution with film thickness, Vacuum 99 (2014) 149–152.

[9] T. Jörg, A.M. Hofer, H. Köstenbauer, J. Winkler, C. Mitterer, Oxidation and wet etching behavior of sputtered Mo-Ti-Al films, J. Vac. Sci. Technol. A 36 (2018) 21513.

[10] A. List, C. Mitterer, G. Mori, J. Winkler, N. Reinfried, W. Knabl, Oxidation of sputtered thin films of molybdenum alloys at ambient conditions, Proceeding of the 17th Plansee Seminar Vol. 1 (2009) RM 12/1-9.

[11] C. Nico, T. Monteiro, M.P.F. Graça, Niobium oxides and niobates physical properties: Review and prospects, Prog. Mater. Sci. 80 (2016) 1–37.

[12] A. Foroughi-Abari, K.C. Cadien, Growth, structure and properties of sputtered niobium oxide thin films, Thin Solid Films 519 (2011) 3068–3073.

[13] B. Hunsche, M. Vergöhl, H. Neuhäuser, F. Klose, B. Szyszka, T. Matthée, Effect of deposition parameters on optical and mechanical properties of MF- and DC-sputtered Nb_2O_5 films, Thin Solid Films 392 (2001) 184–190.

[14] S. Venkataraj, R. Drese, O. Kappertz, R. Jayavel, M. Wuttig, Characterization of niobium oxide films prepared by reactive dc magnetron sputtering, Phys. Status. Solidi. A 188 (2001) 1047–1058.

[15] F. Lai, L. Lin, Z. Huang, R. Gai, Y. Qu, Effect of thickness on the structure, morphology and optical properties of sputter deposited Nb_2O_5 films, Appl. Surf. Sci. 253 (2006) 1801–1805.

[16] G. Ramírez, S.E. Rodil, S. Muhl, D. Turcio-Ortega, J.J. Olaya, M. Rivera, E. Camps, L. Escobar-Alarcón, Amorphous niobium oxide thin films, J. Non.-Cryst. Solids. 356 (2010) 2714–2721.

[17] D.M. Mattox, Handbook of Physical Vapor Deposition (PVD) Processing, 2nd ed., William Andrew, Oxford, UK, 2010.

[18] W.D. Westwood, Sputter Deposition, AVS, New York, 2003.

[19] T. Schmidt, H. Assadi, F. Gärtner, H. Richter, T. Stoltenhoff, H. Kreye, T. Klassen, From particle acceleration to impact and bonding in cold spraying, J. Therm. Spray. Tech. 18 (2009) 794–808.

[20] T. Schmidt, F. Gärtner, H. Assadi, H. Kreye, Development of a generalized parameter window for cold spray deposition, Acta Mater. 54 (2006) 729–742.

[21] T.H. van Steenkiste, J.R. Smith, R.E. Teets, J.J. Moleski, D.W. Gorkiewicz, R.P. Tison, D.R. Marantz, K.A. Kowalsky, W.L. Riggs, P.H. Zajchowski, B. Pilsner, R.C. McCune, K.J. Barnett, Kinetic spray coatings, Surf. Coat. Tech. 111 (1999) 62–71.

[22] S. Grigoriev, A. Okunkova, A. Sova, P. Bertrand, I. Smurov, Cold spraying: From process fundamentals towards advanced applications, Surf. Coat. Tech. 268 (2015) 77–84.

[23] P.J. Kelly, R.D. Arnell, Magnetron sputtering: A review of recent developments and applications, Vacuum 56 (2000) 159–172.

[24] G. Bräuer, B. Szyszka, M. Vergöhl, R. Bandorf, Magnetron sputtering – Milestones of 30 years, Vacuum 84 (2010) 1354–1359.

[25] M. Ohring, Materials Science of Thin Films: Deposition and Structure, 2nd ed., Academic Press, San Diego, Calif., 2002.

[26] S. Matthews, W. de Bosscher, A. Blondeel, J. van Holsbeke, H. Delrue, New target materials for innovative applications on glass, Vacuum 83 (2008) 518–521.

[27] R. de Gryse, J. Haemers, W.P. Leroy, D. Depla, Thirty years of rotatable magnetrons, Thin Solid Films 520 (2012) 5833–5845.

[28] A. Blondeel, P. Persoone, W. de Bosscher, Rotatable magnetron sputter technology for large area glass and web coating, VIP 21 (2009) 6–13.

[29] P.J. Kelly, G. West, Y.N. Kok, J.W. Bradley, I. Swindells, G.C.B. Clarke, A comparison of the characteristics of planar and cylindrical magnetrons operating in pulsed DC and AC modes, Surf. Coat. Tech. 202 (2007) 952–956.

[30] J. Musil, P. Baroch, J. Vlček, K.H. Nam, J.G. Han, Reactive magnetron sputtering of thin films: present status and trends, Thin Solid Films 475 (2005) 208–218.

[31] W.D. Sproul, D.J. Christie, D.C. Carter, Control of reactive sputtering processes, Thin Solid Films 491 (2005) 1–17.

[32] S.M. Rossnagel, I. Yang, J.J. Cuomo, Compositional changes during magnetron sputtering of alloys, Thin Solid Films 199 (1991) 59–69.

[33] L.R. Shaginyan, M. Mišina, S. Kadlec, L. Jastrabík, A. Macková, V. Peřina, Mechanism of the film composition formation during magnetron sputtering of WTi, J. Vac. Sci. Technol. A 19 (2001) 2554–2566.

[34] N. Bundaleski, S. Petrović, D. Peruško, J. Kovač, A. Zalar, Composition of the sputter deposited W–Ti thin films, Appl. Surf. Sci. 254 (2008) 6390–6394.

[35] J. Neidhardt, S. Mráz, J.M. Schneider, E. Strub, W. Bohne, B. Liedke, W. Möller, C. Mitterer, Experiment and simulation of the compositional evolution of Ti–B thin films deposited by sputtering of a compound target, J. Appl. Phys. 104 (2008) 63304.

[36] P. Losbichler, C. Mitterer, W.S.M. Werner, H. Störi, J. Barounig, The influence of various process gases on the magnetron sputtering of ZrB_{12}, Thin Solid Films 228 (1993) 56–59.

[37] R. Lorenz, M. O'Sullivan, D. Sprenger, B. Lang, C. Mitterer, Chemical composition and properties of MoAl thin films deposited by sputtering from MoAl compound targets, J. Vac. Sci. Technol. A 35 (2017) 41504.

[38] I. Petrov, P.B. Barna, L. Hultman, J.E. Greene, Microstructural evolution during film growth, J. Vac. Sci. Technol. A 21 (2003) S117-S128.

[39] P.B. Barna, M. Adamik, Fundamental structure forming phenomena of polycrystalline films and the structure zone models, Thin Solid Films 317 (1998) 27–33.

[40] A. Papyrin, V. Kosarev, S. Klinkov, A. Alkimov, V. Fomin, Cold Spray Technology, 1st ed., Elsevier, Amsterdam, 2007.

[41] V.K. Champagne, The cold spray materials deposition process: Fundamentals and applications, Woodhead, Cambridge, Boca Raton, 2007.

[42] T. Schmidt, Kaltgasspritzen: Eine Analyse des Materialverhaltens beim Partikelaufprall und die daraus abgeleitete Prozessoptimierung, Shaker, Aachen, 2007.

[43] R.N. Raoelison, C. Verdy, H. Liao, Cold gas dynamic spray additive manufacturing today: Deposit possibilities, technological solutions and viable applications, Mater. Design 133 (2017) 266–287.

[44] H.-K. Kang, S.B. Kang, Tungsten/copper composite deposits produced by a cold spray, Scripta Mater. 49 (2003) 1169–1174.

[45] A. Sova, D. Pervushin, I. Smurov, Development of multimaterial coatings by cold spray and gas detonation spraying, Surf. Coat. Tech. 205 (2010) 1108–1114.

[46] H. Assadi, F. Gärtner, T. Stoltenhoff, H. Kreye, Bonding mechanism in cold gas spraying, Acta Mater. 51 (2003) 4379–4394.

[47] T. Stoltenhoff, C. Borchers, F. Gärtner, H. Kreye, Microstructures and key properties of cold-sprayed and thermally sprayed copper coatings, Surf. Coat. Tech. 200 (2006) 4947–4960.

[48] K. Spencer, V. Luzin, N. Matthews, M.-X. Zhang, Residual stresses in cold spray Al coatings: The effect of alloying and of process parameters, Surf. Coat. Tech. 206 (2012) 4249–4255.

[49] R. Lorenz, M. O'Sullivan, A. Fian, D. Sprenger, B. Lang, C. Mitterer, A comparative study on NbO_x films reactively sputtered from sintered and cold gas sprayed targets, Appl. Surf. Sci. 436 (2018) 1157–1162.

[50] S. Kumar, A. Jyothirmayi, N. Wasekar, S.V. Joshi, Influence of annealing on mechanical and electrochemical properties of cold sprayed niobium coatings, Surf. Coat. Tech. 296 (2016) 124–135.

7. PUBLICATIONS

I. R. Lorenz, M. O'Sullivan, D. Sprenger, B. Lang, C. Mitterer, Cold spraying of Mo-Nb coatings, manuscript in final preparation.

II. R. Lorenz, M. O'Sullivan, D. Sprenger, B. Lang, C. Mitterer, Chemical composition and properties of MoAl thin films deposited by sputtering from MoAl compound targets, J. Vac. Sci. Technol. A 35 (2017) 041504.

III. R. Lorenz, M. O'Sullivan, D. Sprenger, B. Lang, H. Köstenbauer, J. Winkler, C. Mitterer, Oxidation and wet-etching behaviour of MoAlTi thin films deposited by sputtering from a rotatable MoAlTi compound target, submitted for publication.

IV. R. Lorenz, M. O'Sullivan, A. Fian, D. Sprenger, B. Lang, C. Mitterer, A comparative study on NbO_x films reactively sputtered from sintered and cold gas sprayed targets, Appl. Surf. Sci. 436 (2018) 1157-1162.

V. R. Lorenz, M. O'Sullivan, A. Fian, D. Sprenger, B. Lang, C. Mitterer, Effect of the bias pulse frequency on reactively sputter deposited NbO_x films, submitted for publication.

Publication I

Cold gas spraying of Mo-Nb coatings

Roland Lorenz, Michael O'Sullivan, Dietmar Sprenger, Bernhard Lang, Christian Mitterer

Manuscript in final preparation

Cold gas spraying of Mo-Nb coatings

Roland Lorenz[1*], Michael O'Sullian[2], Dietmar Sprenger[2], Bernhard Lang[2],

Christian Mitterer[1]

[1] Department of Physical Metallurgy and Materials Testing, Montanuniversität Leoben, Franz-Josef-Straße 18, 8700 Leoben, Austria

[2] Plansee SE, Metallwerk-Plansee-Straße 71, 6600 Reutte, Austria

Abstract

Within the current work, Mo-Nb coatings have been deposited on Ti substrates by cold gas spraying. Two different approaches for powders have been compared, i.e. a Mo/Nb powder mixture and elemental Mo and Nb powders, where for the latter the feed rate was individually controlled by two separate powder feeders. Additional variations included the shape of the used Mo powders as well as the spraying gas temperature and gas pressure. The homogenous, dense and low porosity coatings are characterised by a significantly decreased Mo content within the coating with respect to the powder composition used. A higher gas temperature and pressure increased the deposition efficiency, which nevertheless strongly declines as the Mo content within the powder mixtures increases. The use of a more porous Mo powder results in a higher deposition efficiency and higher Mo content within the coatings, as compared to a densified Mo powder.

[*] Corresponding author: Mail: roland.lorenz@stud.unileoben.ac.at

1. Introduction

Cold gas spraying (CGS), a novel deposition technology within the field of thermal spraying, has created a lot of interest in research, leading subsequently to a growing market share within the last decade [1–3]. The major advantage of CGS, compared to other thermal spray processes like flame spraying or plasma spraying, is the avoidance of melting or thermal softening of the powder particles prior to the impact on the substrate [1–6]. The deposition of solid and dense coatings by CGS is attributed to the high kinetic energy impact of the solid powder particles onto the substrate, leading to a low oxygen content and low thermal stresses in the coating and the substrate, preventing coating failure at the substrate-coating interface [4–7]. The powder particles are accelerated by a high pressurized gas jet with the use of a De Laval type nozzle to reach supersonic velocities of up to ~1200 m/s. The particle temperature during impact ranges between room temperature and 800°C, depending on the adjusted gas temperature (up to 1000°C), the nozzle design, the particle size and the heat capacity of the particles [2,3,5,8]. If the powder particles reach a critical velocity, they are bonded to each other and to the substrate due to adiabatic shear instability and localized extensive plastic deformation [2,6,8]. As reported by Grigoriev et al. [2], the critical velocity can depend on the particle specific heat, the particle melting point, the particle density, the particle yield strength as well as the particle impact temperature.

Reports on the cold gas spraying of refractory metals or refractory metal containing compound systems are rare due to their brittle nature and the thus low deposition efficiency, but they can be found for systems like WC-Co [9], Mo-Al [10], Nb [11,12], and W-Cu [13]. Within this work, the sprayability of the Mo-Nb system by CGS is explored, to shed light on the deposition efficiency, the chemical composition of the CGS coatings as well as the microstructural development for systematically varied spraying conditions.

2. Experimental

Spraying was performed using an industrial-scale CGS device with a maximum operating pressure of 60 bar and a maximum gas temperature of 1000°C, with two powder feeders

connected. Nitrogen was used as carrier gas. The powder was sprayed in 100 layers onto cylindrical titanium substrate rods (ø 30 mm) with a length of 30 mm, using a spraying distance between nozzle and substrate of 40 mm, by oscillating the nozzle in front of the substrate. Two different settings of nitrogen gas temperature and gas pressure have been chosen for the depositions, i.e. 800°C/47 bar and 1000°C/60 bar. A fused and crushed Nb powder with a particle size between 5 and 45 µm (Amperit 160.003, H.C. Starck, Goslar, Germany [14]) was used together with two different Mo powders. First, an agglomerated and sintered Mo powder with a particle size of 15 to 45 µm (Amperit 105.074, H.C. Starck, Goslar, Germany [14]) and second, a densified, spherical powder with a particle size of 10 to 44 µm (SD 152, Global Tungsten & Powders, Towanda, USA [15]). To vary the chemical composition of the deposited coatings, powder mixtures with mixing ratios of 50/50, 60/40, 70/30, 80/20 and 90/10 at.% Mo/Nb were prepared prior to CGS by mixing in a Turbula mixer (type T2F, WAB AG Maschinenfabrik, Muttenz, Switzerland) for 1 h. For comparison with these prepared powder mixtures, the chemical composition of the Mo/Nb powder feedstock was also varied by adjusting the feed rates of the two powder feeders filled with the individual elemental molybdenum and niobium powders, in a second deposition run. The overall powder feeding rate was kept constant at ~30 g/min for both experimental setups, i.e. the spraying of the powder mixtures and the two individual elemental powders.

The deposition efficiency of the cold spraying process was calculated from the weight gain of the titanium substrates in relation to the used powder. The chemical composition of the sprayed coatings was examined by X-ray fluorescence spectroscopy (XRF) using a Bruker S8-TIGER. To study the microstructure of the coatings, metallographic cross-sections were prepared by grinding the samples with a Struers TegraPol-31 using silicon carbide abrasive paper with increasing grit from 320 to 4000. The subsequent polishing was done with a silicon dioxide polishing suspension (OP-S, Struers, Willich, Germany). Light optical images were recorded using a Zeiss Axio Imager M1m with a Zeiss Axio Cam MRc5 camera, after etching the grinded and polished metallographic cross sections in a Murakami etchant for 8 s. The Murakami etchant, composed of 10 g $K_3Fe(CN)_6$, 10 g NaOH and 100 ml H_2O, is known for dissolving molybdenum and molybdenum alloys, while niobium remains unaffected [16]. Finally, X-ray diffraction (XRD) measurements

were performed using a Bruker-AXS D8 Advance diffractometer in Bragg-Brentano configuration with Cu-Kα radiation (λ = 1.5406 Å).

3. Results and discussion

3.1. Spraying with Mo/Nb powder mixtures

Figure 1 shows the development of the Mo and Nb content within the sprayed coatings as a function of the Mo content within the used powder mixtures. In both cases, the agglomerated and sintered Mo powder was used. Figure 1 (a) displays the chemical composition and the deposition efficiency obtained by spraying at a gas temperature of 800°C and a pressure of 47 bar, while Figure 1 (b) summarizes the results for 1000°C and 60 bar. A steady increase of the Mo content within the coating can be seen for the rising Mo fraction within the powder, however, with a significant depletion of Mo compared to the powder compositions. The losses vary between ~25 at.% for the coatings sprayed with the 80/20 at.% Mo/Nb and ~50 at.% for the 50/50 at.% Mo/Nb powder mixture. Comparing the development of the coating compositions for the two different spraying conditions, the observed differences are only minor. Essentially, the two settings differ solely in the deposition efficiency. The higher spraying temperature and pressure leads to an efficiency maximum of 62%, which is up to ~8% higher than for the low temperature/pressure setting. A higher gas temperature increases the gas density and therefore the velocity of the sprayed particles, since particle acceleration is performed by drag [5]. Particles sprayed at a higher temperature can thus reach the critical velocity easier, which fosters their bonding on the substrate and coating surface [2,3]. By spraying the powder mixture of 80/20 at.% Mo/Nb, the deposition efficiency significantly drops. For the powder mixture 90/10 at.% Mo/Nb no deposition occurs, independent of the applied temperature/pressure setting. The large fraction of brittle Mo particles within the mixture erodes the surface instead of coating build-up [3].

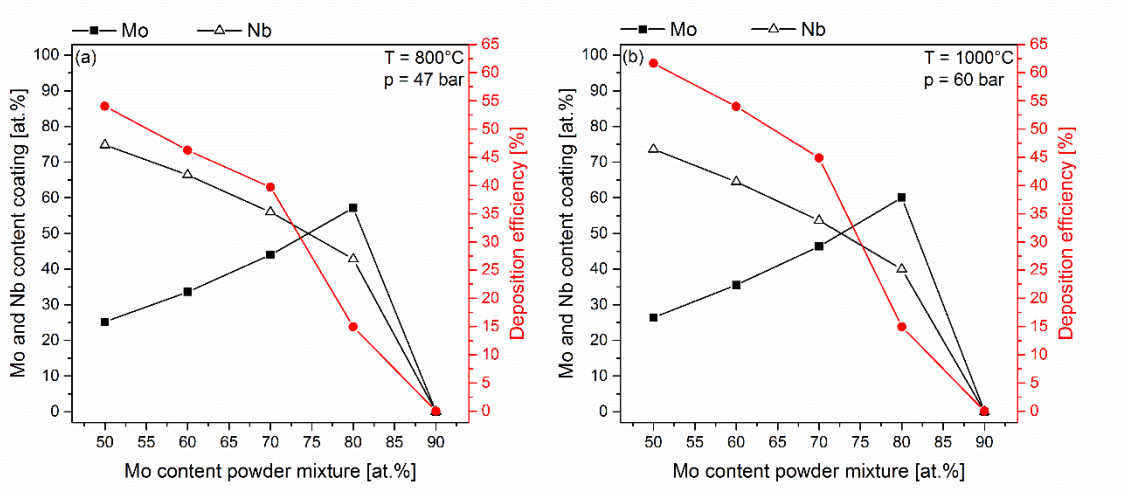

Figure 1: *Development of the Mo and Nb content within the coatings as well as the deposition efficiency as a function of the Mo content within the powder mixture for (a) 800°C/47 bar and (b) 1000°C/60 bar.*

3.2. Spraying with elemental Mo and Nb powders

To evaluate eventual differences between the use of Mo/Nb powder mixtures and individual elemental powders, a second approach with Mo and Nb powders supplied separately via the two powder feeders was chosen. There, the agglomerated and sintered Mo powder and the Nb powder were used. Figure 2 shows again the development of the Mo and Nb content within the coatings, in addition to the development of the deposition efficiency, as a function of the Mo/Nb feed rate ratio. Since the total feed rate was kept constant, a feed rate ratio of 1 can be compared to a composition of 50 at.% Mo and 50 at.% Nb, while a feed rate ratio of 4 should be equal to a composition of 80 at.% Mo and 20 at.% Nb. The chemical composition of the coatings displayed in Figure 2 shows a similar trend as for the powder mixtures (see Figure 1). While the Mo content of the coating remains significantly below that of the powder composition, the Nb content of the coating is much higher than the corresponding Mo/Nb feed ratio, indicating good particle adhesion and thus high deposition efficiency for all coatings up to a feed rate ratio of 4. With further increase of the feed rate ratio, much less coating is built up and the deposition efficiency approaches 0%. The maximum deposition efficiency is 62%, which is equal to the maximum deposition efficiency during spraying of the powder mixture at 1000°C and 60 bar (see Figure 1(b)). The differences observed in the utilisation of a powder mixture or

the two individual elemental powders are therefore marginal. While using the two powder feeders for Mo and Nb has the advantage of a more flexible adjustment of the chemical composition, also during spraying in case of the fabrication of gradient coatings, the application of powder mixtures can yield a more homogenous chemical distribution within the coating with a better reproducibility [2].

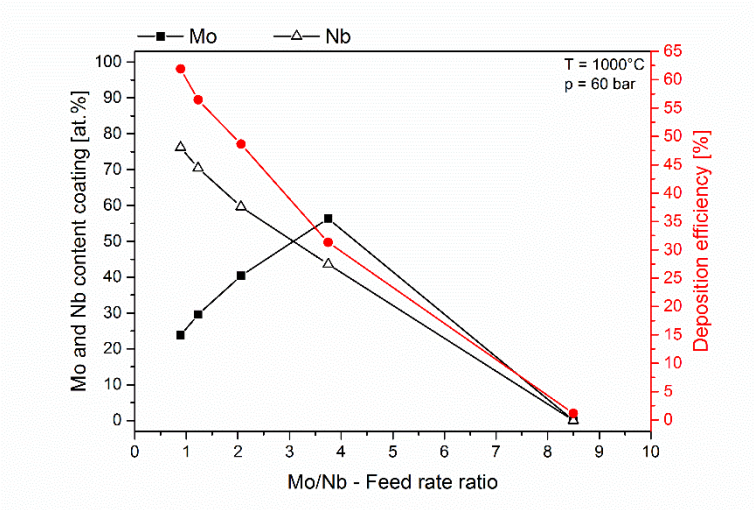

Figure 2: *Development of the Mo and Nb content within the coatings as well as the deposition efficiency as a function of the Mo/Nb feed rate ratio for spraying with two powder feeders at 1000°C and 60 bar.*

3.3. Variation of the Mo powder characteristic

The effect of Mo powders, which differ in shape and particle density, on the chemical composition and the deposition efficiency of sprayed Mo-Nb coatings is shown in Figure 3. Two powder mixtures with composition of 50/50 and 70/30 at.% Mo/Nb were sprayed at 1000°C and 60 bar, where on the one hand the agglomerated and sintered Mo powder (left side of Figure 3) and on the other hand the densified, spherical Mo powder (right side of Figure 3) have been used. For these two Mo powders, clear deviations in the chemical composition of the sprayed coatings have been observed. In particular, spraying the mixture with the spherical Mo powder leads to an even more significant loss of Mo within the coating. Mo contents of only ~10 to ~20 at.% could be determined compared to ~26 and ~46 at.% for the mixture prepared from the agglomerated and sintered Mo powder. The deposition efficiency obtained with the spherical Mo powder based mixture shows a similar trend as for the agglomerated and sintered Mo powder

based mixture, but is considerably lower due to the loss of Mo within the coating. The decreased sprayability of the densified and spherical Mo powder can be explained by the lower ductility of these particles. In CGS, particles should provide sufficient ductility to form a dense and adherent coating; they should be able to withstand the intense plastic deformation [8]. Only then, adiabatic shear instability is able to develop at the particle/substrate interface during particle impact, which is necessary for successful particle bonding [2,3,6,8].

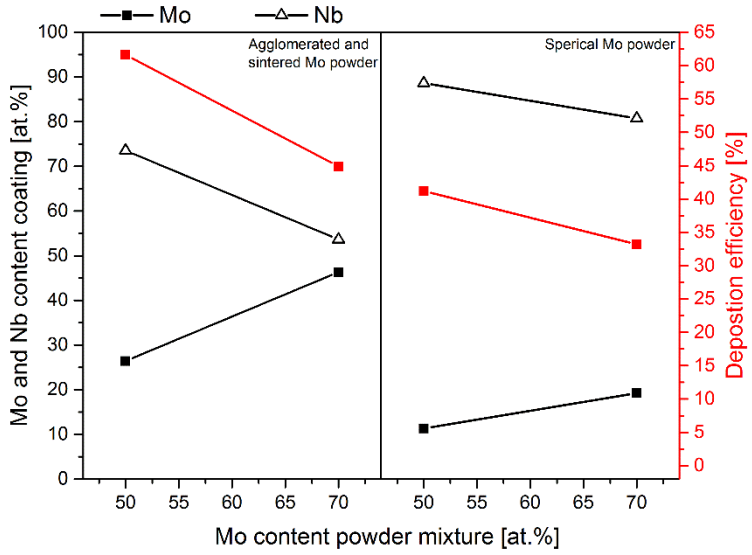

Figure 3: *Development of the Mo and Nb content within the coating as well as the deposition efficiency as a function of the Mo content within the powder mixtures for agglomerated and sintered Mo powder (left side) and densified, spherical Mo powder (right side) at 1000°C and 60 bar.*

3.4. Coating microstructure

Figure 4 displays the microstructural development, as observed by light optical images of the corresponding cross-sections, for four cold gas sprayed coatings deposited at 1000°C and 60 bar with increasing Mo content within the used powder mixtures: (a) 50/50 at.% Mo/Nb, (b) 60/40 at.% Mo/Nb, (c) 70/30 at.% Mo/Nb and (d) 80/20 at.% Mo/Nb. Since there was no deposition for the 90/10 at.% Mo/Nb powder mixture (see Figure 1(b)), no cross-section could be prepared. For a better contrast, the cross-sections have been etched with a Murakami etchant, causing the Mo particles to appear in dark grey colour. The distribution of the Mo and Nb particles is homogenous for all four

coatings, which was also evident across the whole coating thickness. The coatings sprayed with the powder mixtures of 50/50 and 60/40 at.% Mo/Nb are mainly characterised by Nb-Nb and Mo-Nb interfaces and thus also bonds (see Figures 4(a) and (b)). In comparison, an increased number of Mo-Mo interfaces can be seen for the two coatings deposited at the respective higher Mo content (see Figures 4(c) and (d)). This increased fraction of interfaces between the brittle Mo grains explains the significant drop in deposition efficiency (see Figure 1), since the impact of a Mo particle on a Mo coated surface does not provide sufficient ductility to develop adiabatic shear instabilities and therefore bonding becomes more challenging. The particle shape visible within the cross-sections is characterised by the high velocity impact of the particle onto the substrate surface, showing a strong deformation. With particles flattened out or partially showing a lenticular shape, their shape differs strongly from the original powder particle shape, which can be described as porous and spherical for the agglomerated and sintered Mo powder and irregular and blocky for the Nb powder [14]. For the coatings sprayed up to the powder mixture of 70/30 at.% Mo/Nb, hardly any porosity can be seen within the cross-sections, corroborating that a dense coating is formed. Formation of such dense coatings is one of the characteristic features of CGS coatings [5,8], which has also been reported for Nb coatings [11,12]. In comparison, several large pores, with sizes of more than 50 µm, are present in the cross-section of the sample sprayed with the 80/20 at.% Mo/Nb powder mixture, as indicated by the red arrows in Figure 4 (d). Spraying with the 80/20 at.% Mo/Nb powder mixture is therefore unsuitable, since these pores can contribute to the failure of the coating.

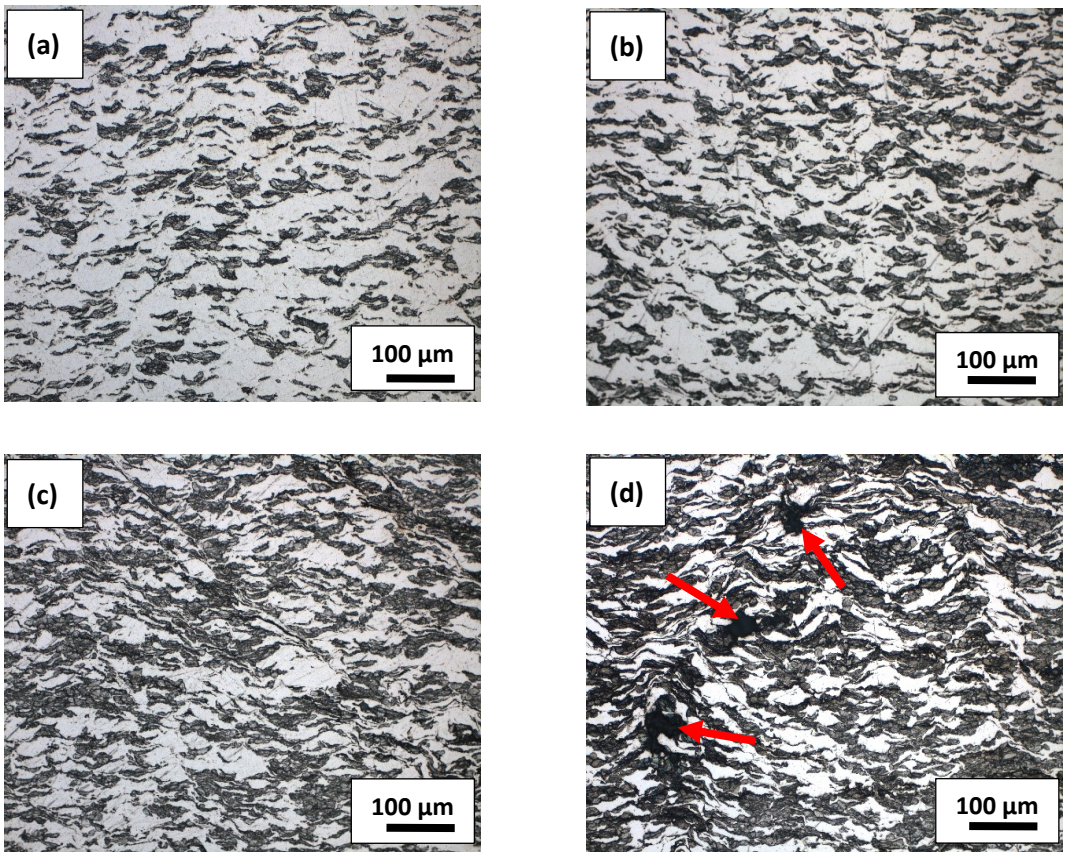

Figure 4: *Light optical micrographs of four Mo-Nb samples sprayed at 1000°C and 60 bar with powder mixtures of (a) 50/50 at.% Mo/Nb, (b) 60/40 at.% Mo/Nb, (c) 70/30 at.% Mo/Nb and (d) 80/20 at.% Mo/Nb. The red arrows indicate the locations of pores.*

Figure 5 displays representative X-ray diffractograms of the four coatings sprayed using powder mixtures between 50/50 and 80/20 at.% Mo/Nb based on the agglomerated and sintered Mo powder. These diffractograms do not differ significantly from those obtained for other Mo-Nb coatings investigated in this work. Due to the low temperature during cold gas spraying, which is not sufficient to melt the metallic powders during spraying [3], Mo and Nb can be determined as separated phases without the occurrence of a solid solution. Also no oxide impurities could be detected, since the oxygen content within CGS coatings is known to be in the same range as the oxygen content of the powder feedstock. Additionally, thin oxide layers on the particle surface can be shattered by the particle impact and removed by the gas stream [5,17]. The formation of an intermetallic compound is also not possible, since the Mo-Nb phase diagram is characterized by a complete solubility in the liquid and the solid state [18].

Differences between the coatings can be detected for the peak heights observed for the Mo and Nb phases, which reflects the changing chemical composition.

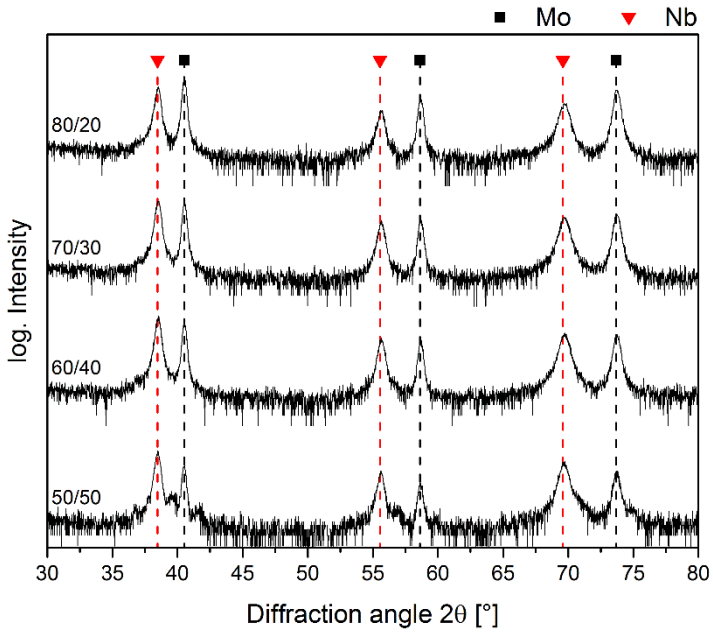

Figure 5: *X-ray diffractograms of Mo-Nb coatings sprayed at 1000°C and 60 bar with powder mixtures of 50/50, 60/40, 70/30 and 80/20 at.% Mo/Nb. The black squares and red triangles indicate the diffraction peaks of pure Mo and Nb [19,20].*

4. Conclusions

Mo-Nb coatings have been prepared by cold gas spraying onto Ti substrates with a systematic variation of the chemical composition of the powder mixtures, the shape of the used Mo powder, and the gas temperature and gas pressure. A higher deposition efficiency could be achieved for an increased temperature and pressure, reaching a maximum of 62%, but showing a dramatic drop as the Mo content within the powder mixtures exceeds a certain threshold. The use of a spherical and densified Mo powder leads to a further decrease of both, the deposition efficiency and the Mo content within the coating, due to low ductility of the powder particles. The Mo-Nb coatings are basically characterized by a homogenous distribution of the Mo and Nb particles, forming a dense coating with largely deformed particles without any sign of oxidation. Only the coatings sprayed with powder mixtures with a Mo content of at least 80 at.%

showed a significant development of large pores; no coating build-up could be observed for 90/10 at.% Mo/Nb powder mixtures, thus representing the limit of sprayability of Mo-Nb coatings by cold gas spraying. The addition of a sufficient fraction of Nb to the powder mixture and the utilisation of a porous Mo powder therefore enable the fabrication of Mo containing coatings by cold spraying.

5. Acknowledgments

This work was supported by the Österreichische Forschungsförderungsgeslleschaft FFG within the project “E²CGS” (Project No. 150130).

6. References

[1] R.N. Raoelison, C. Verdy, H. Liao, Cold gas dynamic spray additive manufacturing today: Deposit possibilities, technological solutions and viable applications, Mater. Design. 133 (2017) 266–287.

[2] S. Grigoriev, A. Okunkova, A. Sova, P. Bertrand, I. Smurov, Cold spraying: From process fundamentals towards advanced applications, Surf. Coat. Tech. 268 (2015) 77–84.

[3] T. Schmidt, H. Assadi, F. Gärtner, H. Richter, T. Stoltenhoff, H. Kreye, T. Klassen, From particle acceleration to impact and bonding in cold spraying, J. Therm. Spray. Tech. 18 (2009) 794–808.

[4] T. Stoltenhoff, C. Borchers, F. Gärtner, H. Kreye, Microstructures and key properties of cold-sprayed and thermally sprayed copper coatings, Surf. Coat. Tech. 200 (2006) 4947–4960.

[5] T.H. van Steenkiste, J.R. Smith, R.E. Teets, J.J. Moleski, D.W. Gorkiewicz, R.P. Tison, D.R. Marantz, K.A. Kowalsky, W.L. Riggs, P.H. Zajchowski, B. Pilsner, R.C. McCune, K.J. Barnett, Kinetic spray coatings, Surf. Coat. Tech. 111 (1999) 62–71.

[6] H. Assadi, F. Gärtner, T. Stoltenhoff, H. Kreye, Bonding mechanism in cold gas spraying, Acta Mater. 51 (2003) 4379–4394.

[7] K. Spencer, V. Luzin, N. Matthews, M.-X. Zhang, Residual stresses in cold spray Al coatings: The effect of alloying and of process parameters, Surf. Coat. Tech. 206 (2012) 4249–4255.

[8] T. Schmidt, F. Gärtner, H. Assadi, H. Kreye, Development of a generalized parameter window for cold spray deposition, Acta Mater. 54 (2006) 729–742.

[9] S. Dosta, M. Couto, J.M. Guilemany, Cold spray deposition of a WC-25Co cermet onto Al7075-T6 and carbon steel substrates, Acta Mater. 61 (2013) 643–652.

[10] R. Lorenz, M. O'Sullivan, D. Sprenger, B. Lang, C. Mitterer, Chemical composition and properties of MoAl thin films deposited by sputtering from MoAl compound targets, J. Vac. Sci. Technol. A 35 (2017) 41504.

[11] R. Lorenz, M. O'Sullivan, A. Fian, D. Sprenger, B. Lang, C. Mitterer, A comparative study on NbO_x films reactively sputtered from sintered and cold gas sprayed targets, Appl. Surf. Sci. 436 (2018) 1157–1162.

[12] S. Kumar, A. Jyothirmayi, N. Wasekar, S.V. Joshi, Influence of annealing on mechanical and electrochemical properties of cold sprayed niobium coatings, Surf. Coat. Tech. 296 (2016) 124–135.

[13] H.-K. Kang, S.B. Kang, Tungsten/copper composite deposits produced by a cold spray, Scripta Mater. 49 (2003) 1169–1174.

[14] H.C. Starck, Amperit: Thermal spray powders, https://www.hcstarck.com/en/products/amperitreg_thermal_spray_powders.html, accessed 5 September 2017.

[15] Global Tungsten & Powders, Thermal spray powders: Tungsten carbide, molybdenum and chrome carbide powders, http://www.globaltungsten.com/en/products-services_thermal-spray.htm, accessed 5 September 2017.

[16] Ann Kelly, ASM Handbook Volume 9 - Metallography and Microstructures: Metallography and Microstructures of Refractory Metals and Alloys, American Society for Metals, Metals Park, Ohio, 2004.

[17] V.K. Champagne, The cold spray materials deposition process: Fundamentals and applications, Woodhead, Cambridge, 2007.

[18] H. Okamoto, Mo-Nb (Molybdenum-Niobium), J. Phase. Equilib. 12 (1991) 616–617.

[19] International Centre of Diffraction Data ICDD, Card 00-035-0789 for bcc Nb (2007).

[20] International Centre of Diffraction Data ICDD, Card 03-065-7442 for bcc Mo (2007).

Publication II

Chemical composition and properties of MoAl thin films deposited by sputtering from MoAl compound targets

Roland Lorenz, Michael O'Sullivan, Dietmar Sprenger, Bernhard Lang, Christian Mitterer

Journal of Vacuum Science and Technology A 35 (2017) 041504

Chemical composition and properties of MoAl thin films deposited by sputtering from MoAl compound targets

Roland Lorenz[1*], Michael O'Sullivan[2], Dietmar Sprenger[2], Bernhard Lang[2], Christian Mitterer[1]

[1] Department of Physical Metallurgy and Materials Testing, Montanuniversität Leoben, Franz-Josef-Straße 18, 8700 Leoben, Austria

[2] Plansee SE, Metallwerk-Plansee-Straße 71, 6600 Reutte, Austria

Abstract

Molybdenum-based thin films are widely used as back-contact layers in solar cells, as interconnect material or diffusion barriers in microelectronics, or as gate and source/drain lines in thin film transistor liquid crystal displays. Within this work, the sputter behavior of three different molybdenum-aluminium compound targets with Al contents of 24, 37 and 49 at.% manufactured by cold gas spraying as well as the chemical composition, the microstructure and the properties of the deposited thin films have been investigated. The increase of the Al content in the targets results in an increasing deposition rate of the films. The fine-columnar films are characterized by the formation of a body-centered cubic solid solution resulting in an electrical resistivity increasing from 100 μΩcm for 10 at.% Al to more than 200 μΩcm for 30 at.% Al. Monte Carlo simulations of sputtering and gas phase transport indicate that the observed large deviations of the chemical compositions of the films with respect to the target are mainly caused by aluminium losses due to gas phase scattering.

* Corresponding author: Mail: roland.lorenz@unileobe.ac.at

1. Introduction

In recent years, intense development has focused on the improvement of multifunctional thin films based on molybdenum. Due to their good thermal, chemical and electrical properties, they are commonly used in many different technical areas. Examples are solar cells, where they act as back-contact material, or microelectronics, where they are applied as diffusion barriers. Moreover, they can be used as an interconnect material in large-scale integrated circuits and as gate and source/drain signal lines in thin film transistor liquid crystal displays [1–4]. However, molybdenum is known to readily oxidize even at room temperature, where the oxide films formed cause degradation of optical properties and reduce the electrical conductivity [5]. Thus, as a step towards molybdenum alloy films with improved properties, within this study the sputter behavior of MoAl compound targets as well as the growth and the properties of Al alloyed Mo films was investigated. The MoAl compound targets for the d.c. magnetron sputter process were manufactured by cold-gas spraying, a thermal spray technique which is used to deposit a several mm thick, dense and solid coating by accelerating metallic powders in a high velocity gas jet, with the particularity that the metallic powders are not melted throughout the whole process [6–9]. Due to the large mass difference of Mo and Al, a significant deviation of the composition of the deposited film with respect to the sputter target can be expected as a result of differences in sticking coefficient and preferential resputtering or scattering in the gas phase [10–12]. Therefore, additional simulations within the MoAl system were carried out using the simulation program Transport of Ions in Matter (TRIM) [13,14], providing the basis for the understanding of the sputter process of MoAl compound targets.

2. Experimental Details

2.1. Film deposition and characterization

A series of MoAl thin films was deposited in a laboratory-scale unbalanced d.c. magnetron sputter deposition system containing two MoAl compound targets (Ø 50.8 × 6 mm²) focused on the substrate holder. Three different target compositions, manufactured by cold gas spraying, with Mo/Al atomic ratios of 76/24, 63/37 and 51/49 were used. The films were grown on 20 × 6 × 1 mm^3 soda-lime glass (SLG) and (100) oriented 20 × 6 × 0.35 mm^3 Si substrates, which were ultrasonically cleaned in ethanol and dried with hot air prior to deposition. The target-substrate distance was about 55 mm and the substrate rotation was set at 50 rpm. The vacuum chamber base pressure was kept below 2×10^{-3} Pa and before every deposition the substrates were plasma etched using a pulsed d.c. discharge at -500 V and 250 kHz for 10 min to remove possible contaminations. For every MoAl target variant four deposition runs were performed: The target current and the Ar flow rates were set to 0.2 and 0.4 A per magnetron and to 30 and 60 sccm, respectively, which leads to chamber pressures of 0.5 and 1 Pa. To keep the film thickness in the range between 1.2 and 1.4 µm, the deposition time was reduced from 30 to 15 min when increasing the target current from 0.2 to 0.4 A. During deposition, no additional substrate heating was applied to the substrate holder, which was kept at floating potential.

A Veeco Wyko NT1000 optical profilometer was used for the measurement of the film thicknesses. The surface morphology as well as the fracture cross-section were investigated with a scanning electron microscope (SEM, Zeiss EVO 50). The chemical compositions of the films were determined by energy-dispersive X-ray spectroscopy (EDX, Oxford Instruments INCA) using built-in sensitivity factors. X-ray diffraction (XRD) measurements were performed using a Bruker-AXS D8 Advance diffractometer in Bragg-Brentano configuration with Cu-Kα radiation (λ = 1.5406 Å). To measure the electrical sheet resistivity of the deposited films, a Jandel four point probe was used.

2.2. TRIM calculations

Modelling of the sputtering process of the compound targets as well as the gas phase transport of the sputtered elements was done by TRIM 2013 [13,14]. The static TRIM neglects compositional changes of the target surface due to preferential sputtering of one element; however, it is used here to obtain first insight into the element specific sputtering and scattering behavior of the target species involved [11]. This approach is justified since both components are present in an unalloyed metallic form and in a homogeneous distribution. Ar was used as projectile ion with a minimum and maximum kinetic energy of 300 and 500 eV, respectively, to cover the whole range of magnetron voltages applied during the deposition process. Compound element targets were chosen with similar MoAl compositions as in thin film deposition, with Mo/Al atomic ratios of 75/25, 60/40 and 50/50. For the calculations, the surface binding energies of 3.36 eV for Al and 6.83 eV for Mo are implemented within TRIM, which correspond to the values reported in literature [15]. To achieve a sufficient statistical base, the impact of 5×10^4 ions was simulated and the resulting sputter yields as well as the kinetic energy of the sputtered Mo and Al were recorded.

These kinetic energy values were then used as input parameters for the transport simulation of again 5×10^4 atoms through the Ar gas phase. The calculations were performed for 0.5, 1 and 2 Pa Ar gas pressure and a target-substrate distance of 55 mm. In accordance with Bundaleski et al. [12] and Mahieu et al. [16], several assumptions have been made for the transport calculation. First, the sputtered target atoms can only collide with argon atoms, due to the small number of sputtered atoms compared to the high number of background gas atoms. Second, the distribution of the background gas is constant, so possible pressure variations within the chamber can be ignored. Furthermore, charged particles like ions or electrons are also neglected. Together with the sputter yields from the first simulation step and the now recorded number of transmitted Mo and Al atoms, the final atomic Mo/Al ratio could be calculated.

3. Results and Discussion

3.1. Deposition of MoAl films

Figure 1 shows the deposition rate normalized by the power applied to the magnetrons, calculated from the measured film thickness, deposition time and the applied target power, as a function of the Al content within the targets. The deposition rate basically rises with increasing Al content. This behavior can most likely be explained by the lower surface binding energy of Al (3.36 eV) compared to Mo (6.86 eV) and the consequently higher probability of sputtering Al [15]. In addition, the deposition rate decreases with increasing gas pressure, due to a more pronounced scattering of the sputtered species by Ar atoms during the transport phase [11,17]. Figure 1 also shows that the normalized deposition rate is lower for the higher target current. It might be speculated that this is due to ion bombardment induced changes of the chemical composition of the target surface. To eject a Mo atom out of the target surface, a sequence of collisions between Mo atoms is required after the primary knock-on by an Ar ion [18]. A higher Ar ion energy, i.e. as a result of the rising target voltage as the target current is increased from 0.2 (corresponding to a target voltage of -365 V) to 0.4 A (target voltage -475 V), can lead to a pronounced recoil implantation of Mo atoms in the subsurface layer, giving rise to sputter erosion amplification, as proposed by Berg et al. for a platinum contaminated carbon target [19]. Transferring their arguments of faster dissipation of the energy of the incident ions and quicker randomization of their momentum to the MoAl system, the increased implantation depth of Mo atoms expected for the higher target voltage should result in less efficient sputter erosion amplification, which explains the slightly lower deposition rate for the deposition runs done at 0.4 A.

A comparison of the Al content of the MoAl compound targets and the respective MoAl films measured by EDX can be seen in Figure 2. The large difference between target and film is remarkable, in particular for the 76/24 and 51/49 MoAl target variants. While the films deposited from the 63/37 MoAl target lose ~9 at.% of Al, the losses for the other two variants are with ~14 at.% and ~17 at.% considerably higher. For the deposition parameters varied within this study, the Al contents differ only slightly, whereby a tendency for higher Al contents was observed for the films deposited at 0.2 A as

compared to 0.4 A. The reasons for the observed changes in Al content will be discussed in section 3.2.

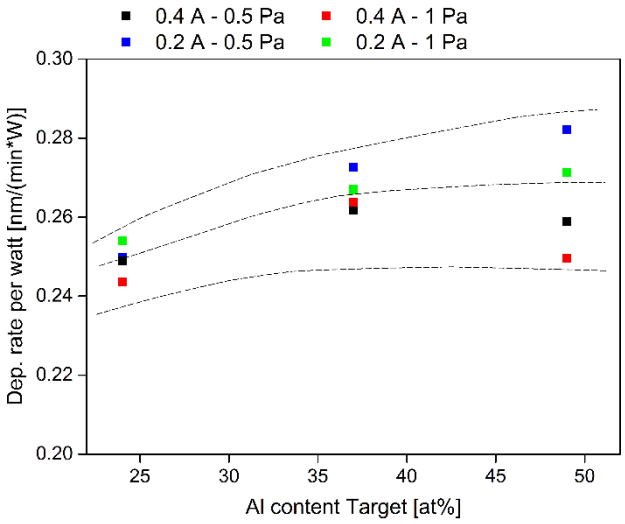

Figure 1: *Deposition rate per watt as a function of the Al content within the targets.*

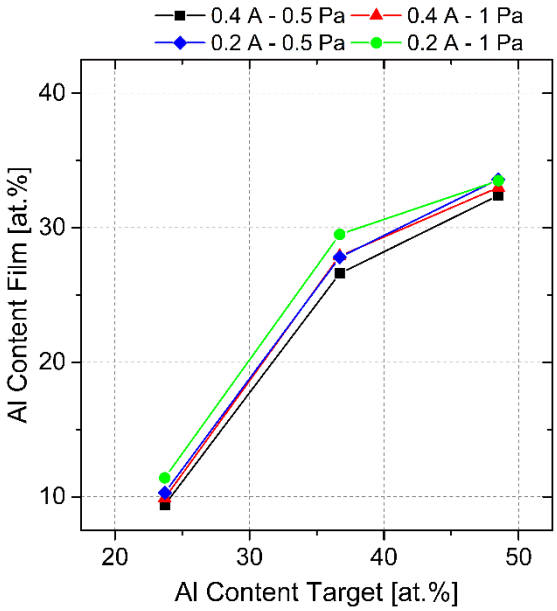

Figure 2: *Comparison of the Al contents of the MoAl compound targets and the MoAl films sputtered from the respective targets.*

None of the films show evidence of delamination from the glass and Si substrates and all films possess a metallic reflecting surface. The SEM top view images, which can be seen on the left-hand side of the images in Figure 3 (a), (b) and (c), confirm the formation of smooth films with a few scattered droplets. Considering the fracture cross-section SEM images (right-hand side of the images), the films show a dense and fine-columnar structure, which is attributable to the Zone T within the structure zone model for microstructural evolution during film growth [20].

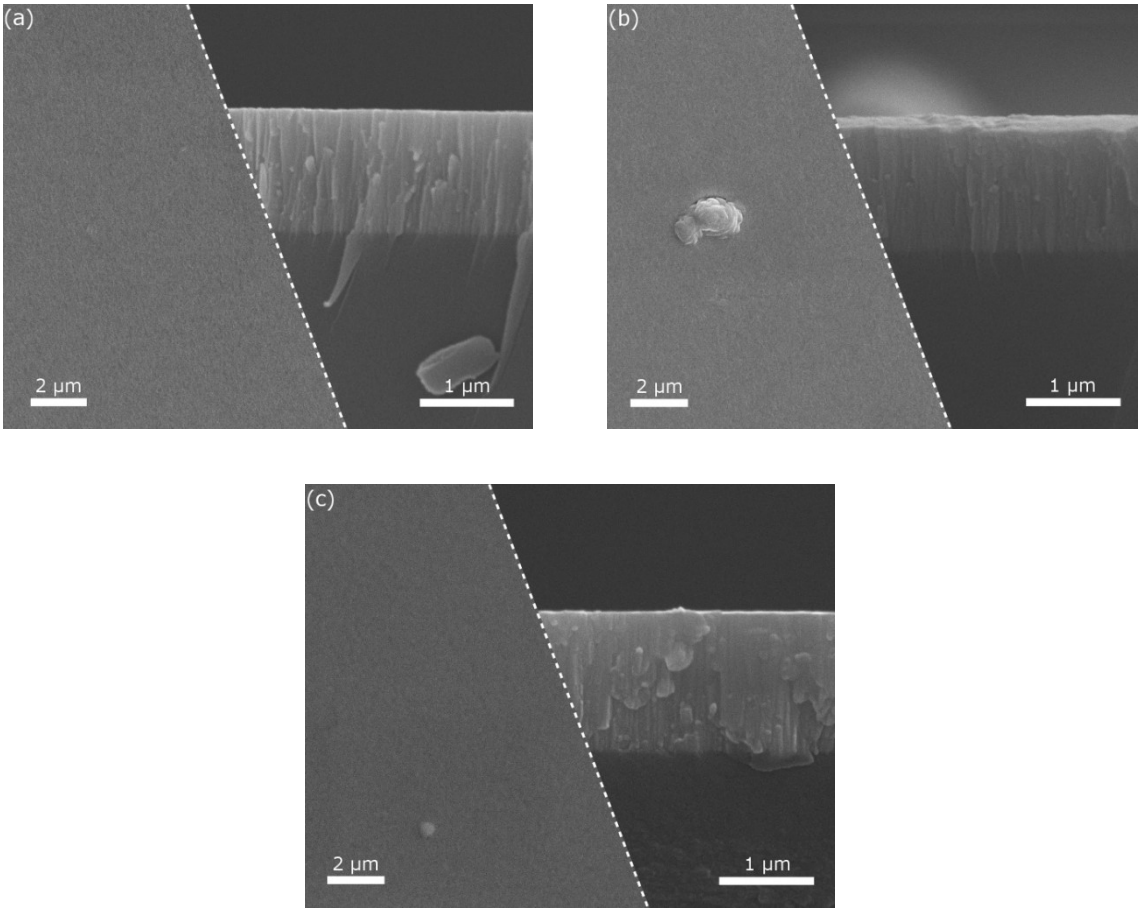

Figure 3: *SEM top view and fracture cross-section images of MoAl films deposited at 0.2 A target current and 0.5 Pa Ar gas pressure onto SLG substrates; (a) 76/24 MoAl target; (b) 63/37 MoAl target; (c) 51/49 MoAl target.*

Figure 4 summarizes the X-ray diffractograms of three MoAl films deposited from the three different target variants on SLG substrates at a target current of 0.4 A and an Ar gas pressure of 0.5 Pa. All films are characterized by formation of a single-phase structure with a Mo-based solid solution with diffraction peaks, which are in good

agreement with the diffraction peaks of pure Mo (2Θ = 40.50°, 58.62°, 73.68°, 87.63°) [21]. Due to the replacement of Mo by the smaller Al atoms in the body-centered cubic lattice, the peaks shift to higher angles compared to the Mo reference positions. The higher the Al content within the used target, the more pronounced is the peak shift, as can be seen in the detail of the (110) Mo peak (Figure 4 (b)). The observed peak shift corresponds to a reduction of the lattice parameter from 3.15 Å for pure Mo to 3.13 Å for the MoAl film deposited from the 51/49 MoAl target. All films show a strong (110) preferred orientation, whereas the (200) peak is almost negligible. With increasing Al content, the intensity of the (110) peak decreases while that of the (211) peak increases slightly. For comparison with thermodynamic equilibrium conditions, the Mo-Al phase diagram [22] shows several intermetallic phases within a broad Al content range. Bielawski [23] and Bates et al. [24], who synthesized MoAl films by co-sputtering, reported on the formation of the Al_8Mo_3 phase at approximately 60-70 wt.% Mo (corresponding to ~30-40 at.% Mo). None of these phases could be found in the current investigation, which is probably caused by the low-energy growth conditions applied within this work. In contrast, Bielawski and Bates et al. applied a bias voltage of up to -100 V.

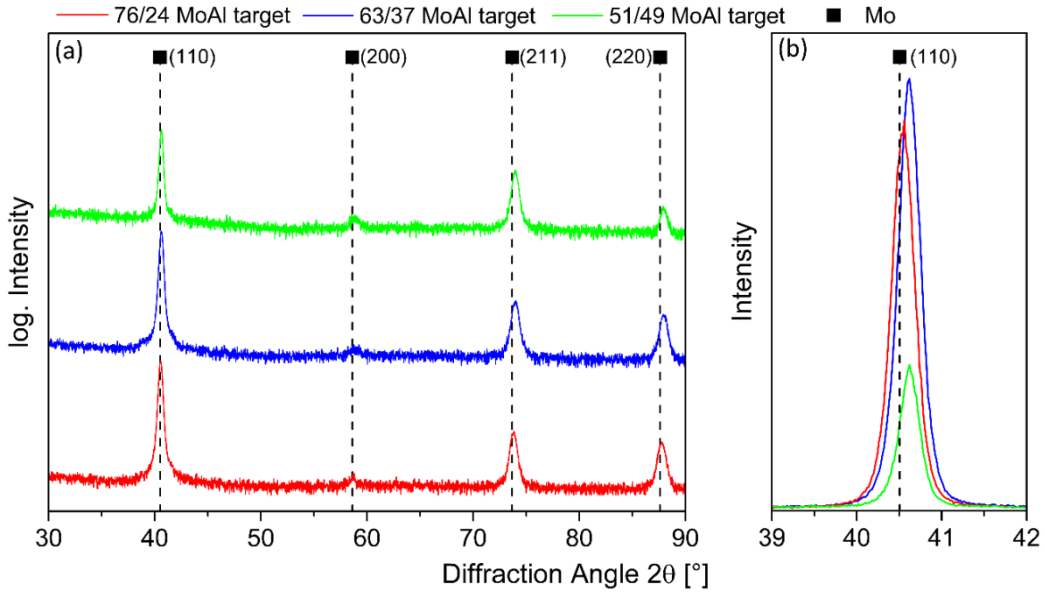

Figure 4: *(a) X-ray diffractograms of three MoAl films deposited at 0.4 A target current and 0.5 Pa Ar gas pressure with varying target compositions; (b) enlarged detail of the (110) peak for varying target composition. The black squares indicate the diffraction peaks of pure Mo [21].*

The influence of alloying Al to Mo thin films on the electrical sheet resistivity as well as the effect of the varied deposition parameters is summarized in Figure 5. Compared to the resistivity of pure Mo films of ~8 µΩcm [1], synthesized under comparable conditions, the deposition of MoAl films with an Al content of ~10 at.% leads to resistivity values of ~100 µΩcm. By increasing the Al content up to 25-35 at.%, the resistivity further increases and reaches a saturation level of ~200 µΩcm. This behavior can be explained by the different atomic sizes of Mo and Al, which consequently leads to local strains and the observed changes in lattice parameters, resulting in pronounced electron scattering. Additionally, different valences introduce a local charge difference that also increases the scattering probability [25]. The differences in resistivity as a result of the varied deposition parameters are insignificantly small, since they lie within the standard deviations of the measured values.

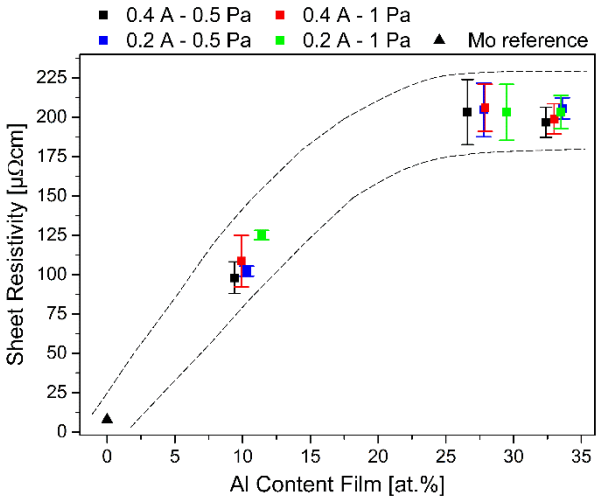

Figure 5: *(Color online) Sheet resistivity of MoAl films on Si substrates as function of the Al content. The black triangle indicates a value for a Mo film taken from reference [1].*

3.2. TRIM calculations

The first step of the simulation calculations was to compute the different sputter yields for the three different target compositions (approximated by Mo/Al atomic ratios of 75/25, 60/40 and 50/50). Bombardment of the MoAl compound target surfaces with Ar projectiles with an ion energy of 500 and 300 eV (for comparison, the magnetron voltage

applied was between -365 and -475 V during deposition) results in different sputter yields depending on the target composition, as summarized in Table 1. The comparison of the ratios of sputter yields of Mo to Al and the respective target composition ratios indicates an Al flux leaving the target higher than the Al content within the target, which can be explained by the lower surface binding energy of Al leading to preferential sputtering. When decreasing the ion energy from 500 to 300 eV, the sputter yields for both Mo and Al decrease as well, while the ratio of the sputter yields of Mo to Al remains almost constant. The change in sputter yield ratio is less than 1% for all target variants. For comparison, the sputter yields calculated for pure element targets are also given in Table 1. The significantly higher values for Mo and the lower values for Al with respect to the compound targets reflects the positive effect of the sputter erosion amplification mechanism proposed by Berg et al. [19]. In contrast to the sputter yields, the ion energy affects the average kinetic energy of the sputtered atoms. The 500 eV impact energy leads to energies of ~34 eV for the sputtered Mo atoms and to ~14 eV for the Al atoms, while the 300 eV results in energies of ~28 eV for Mo and ~12 eV for Al. In contrast, the change of the target composition has again only a slight influence on the kinetic energy of the sputtered atoms. Here only variations of ≤2% have been observed.

Table 1: *Calculated sputter yields with changing Ar ion energy for the three MoAl target compositions and pure Mo and Al targets.*

	Mo	75/25 Mo/Al		60/40 Mo/Al		50/50 Mo/Al		Al
Ar ion energy [eV]	---	Mo	Al	Mo	Al	Mo	Al	---
300	0.74	0.55	0.28	0.42	0.45	0.35	0.57	0.45
500	1.07	0.78	0.40	0.61	0.65	0.49	0.80	0.70

The transport phase of the sputtered atoms through a 55 mm thick Ar gas layer, which is the second part of the simulation process considered within this work, has an enormous influence on the atom flux arriving at the substrate surface. 99.7% of the Mo atoms originating from a point source with a kinetic energy of 34 eV (i.e. the energy calculated for Mo atoms leaving the target when sputtered with 500 eV Ar ions) are able to transmit through the gas phase at a pressure of 0.5 Pa, while only 81.7% of the Al atoms with 14 eV successfully reach the substrate surface. When increasing the pressure up to 2 Pa, the amount of transmitted atoms decreases for both, the Mo and Al atoms. In this case 79.2% of the Mo atoms reach their final destination on the substrate surface, compared to 27.7% of the Al atoms. This leads to a shift in the Mo/Al ratio of the flux of transmitted atoms from 55/45 at 0.5 Pa to 74/26 at 2 Pa. The decrease of the flux of transmitted atoms with increasing pressure depends on the change of the mean free path of the travelling atoms between collisions. The mean free path shows a pressure as well as an atomic mass dependence [16]. Transport calculations with the lower energy Mo (28 eV) and Al (12 eV) from the 300 eV Ar bombardment indicate an overall decrease of transmitted atoms, while the Mo/Al flux ratio remains approximately constant. Apart from the changes in mean free path, the high loss of Al atoms during the gas phase transport can be explained by the more efficient scattering of lighter atoms during gas phase collisions. Together with the lower energy of the sputtered atoms and the higher energy losses during collision, the lighter elements consequently undergo a more efficient thermalization within the background gas [10,12]. These thermalized atoms deposit uniformly within the vacuum chamber, e.g. on the chamber wall and also on the substrate surface.

Figure 6 shows the development of the Al content within the films depending on the pressure for the depositions done at 0.4 A target current (solid symbols, measured by EDX) and the resulting Al content calculated from the simulated sputter yields and the number of transmitted atoms by TRIM (open symbols) for an Ar ion energy of 500 eV. The dashed lines at 25, 40 and 50 at.% Al indicate the Al content of the targets used for the simulation as a reference. When considering the Al content of the deposited films, the loss of Al is clearly evident. As already mentioned, the differences between target and film compositions for the 63/37 MoAl variant are ~9 at.%, while the Al losses for the

76/24 and 51/49 MoAl targets reach values of ~14 and ~17 at.%, respectively. An increase of the pressure within the range experimentally investigated has hardly any influence on the Al content within the film as opposed to predictions made by TRIM. For the films deposited from the 63/37 MoAl target, the Al content even slightly increases when increasing the pressure from 0.5 to 1 Pa. This behavior can be explained by the different regimes occurring during the transport of atoms with relative mass difference through a gas phase, as reported by Rossnagel et al. [10]. They basically distinguish a ballistic and a diffusive regime. In the ballistic regime, i.e. at low pressure conditions, where only few collisions occur, the film composition reflects the target composition. In the intermediate regime which separates the ballistic from the diffusive regime, lighter elements will scatter more rapidly at the increased pressure, leading to a shift of the composition towards the heavier element. Finally, in the diffusive regime, i.e. for a further increase of the pressure, the heavier species are efficiently scattered, which can now result in a concentration rise of the lighter elements. It can be assumed, that the 0.5 Pa depositions performed in this work correspond to the intermediate regime, while the 1 Pa depositions may already be related to the diffusive regime. The simulated curves show that the Al contents for a pressure of 0.5 Pa remain above the original target compositions due to the preferential sputtering of Al and the relative low scattering at the low pressure. The increasing pressure leads to a higher scatter probability and therefore the Al content decreases for 1 and 2 Pa. Comparing the simulated data with the experimental results, particularly for 0.5 Pa, the differences are considerably substantial. A possible explanation can be found most probably in the calculation of the transport phase. Since the individual elements are calculated separately, TRIM does not take the different transport regimes of binary systems into account. Nevertheless, the TRIM simulation gives a first reasonable explanation for the Al losses during the deposition process. Preferentially gas phase scattering of the lighter elements can therefore be named as the main reason, which leads to the large deviations in the chemical composition of the thin films with respect to the compound targets used.

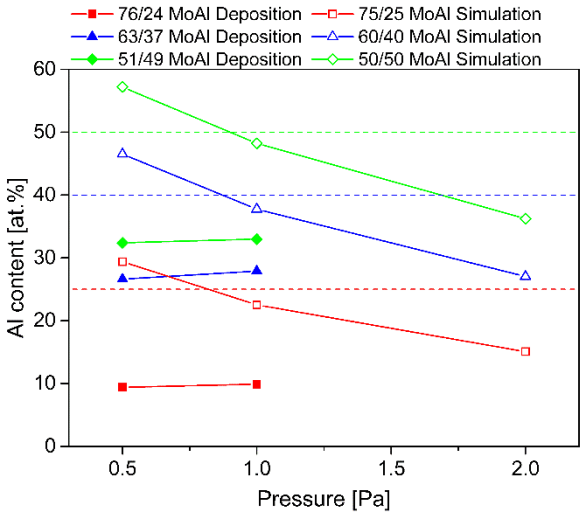

Figure 6: *Al content as a function of pressure for MoAl films deposited at 0.4 A target current (solid symbols) and TRIM simulated with Ar ion energy of 500 eV (open symbols).*

4. Conclusions

The sputter behavior of three MoAl compound targets with Al contents of 24, 37 and 49 at.% manufactured by cold gas spraying, as well as the chemical composition, the microstructure and properties of thin films synthesized by magnetron sputter deposition using these targets have been investigated within this work. Comparisons of the Al content of the targets and the respective films show deviations of up to 17 at.%. The dense films with fine-columnar grains are characterized by the formation of a single-phase structure with a Mo-based solid solution and a strong (110) preferred orientation. An Al content increasing from 10 to 30 at.% within the films results in an electrical resistivity rising from 100 to more than 200 µΩcm. An additional two-step Monte Carlo simulation of the sputtering process and the gas phase transport indicate that the observed deviation in the Al content can be mainly explained by scattering during the gas phase transport.

5. Acknowledgments

This work was supported by the Österreichische Forschungsförderungsgesellschaft FFG within the project “E²CGS” (project number: 150130).

6. References

[1] A.M. Hofer, J. Schlacher, J. Keckes, J. Winkler, C. Mitterer, Sputtered molybdenum films: Structure and property evolution with film thickness, Vacuum 99 (2014) 149–152.

[2] D. Rafaja, H. Köstenbauer, U. Mühle, C. Löffler, G. Schreiber, M. Kathrein, J. Winkler, Effect of the deposition process and substrate temperature on the microstructure defects and electrical conductivity of molybdenum thin films, Thin Solid Films 528 (2013) 42–48.

[3] J.A. Shields, Applications of Molybdenum Metal and its Alloys, International Molybdenum Association (IMOA), London, 2013.

[4] G.K. Rane, S. Menzel, T. Gemming, J. Eckert, Microstructure, electrical resistivity and stresses in sputter deposited W and Mo films and the influence of the interface on bilayer properties, Thin Solid Films 571 (2014) 1–8.

[5] A. List, C. Mitterer, G. Mori, J. Winkler, N. Reinfried, W. Knabl, Oxidation of Sputtered Thin Films of Molybdenum Alloys at Ambient Conditions, Proceedings of the 17th Plansee Seminar, Vol.1 (2009) RM 12/1-9.

[6] H. Assadi, F. Gärtner, T. Stoltenhoff, H. Kreye, Bonding mechanism in cold gas spraying, Acta Mater. 51 (2003) 4379–4394.

[7] S. Grigoriev, A. Okunkova, A. Sova, P. Bertrand, I. Smurov, Cold spraying: From process fundamentals towards advanced applications, Surf. Coat. Tech. 268 (2015) 77–84.

[8] T. Schmidt, H. Assadi, F. Gärtner, H. Richter, T. Stoltenhoff, H. Kreye, T. Klassen, From Particle Acceleration to Impact and Bonding in Cold Spraying, J. Therm. Spray. Techn. 18 (2009) 794–808.

[9] T.H. Van Steenkiste, J.R. Smith, R.E. Teets, J.J. Moleski, D.W. Gorkiewicz, R.P. Tison, D.R. Marantz, K.A. Kowalsky, W.L. Riggs, P.H. Zajchowski, B. Pilsner, R.C. McCune, K.J. Barnett, Kinetic spray coatings, Surf. Coat. Tech. 111 (1999) 62–71.

[10] S.M. Rossnagel, I. Yang, J.J. Cuomo, Compositional changes during magnetron sputtering of alloys, Thin Solid Films 199 (1991) 59–69.

[11] J. Neidhardt, S. Mráz, J.M. Schneider, E. Strub, W. Bohne, B. Liedke, W. Möller, C. Mitterer, Experiment and simulation of the compositional evolution of Ti–B thin films deposited by sputtering of a compound target, J. Appl. Phys. 104 (2008).

[12] N. Bundaleski, S. Petrović, D. Peruško, J. Kovač, A. Zalar, Composition of the sputter deposited W–Ti thin films, Appl. Surf. Sci. 254 (2008) 6390–6394.

[13] Stopping and Range of Ions in Matter, www.srim.org.

[14] J.P. Biersack, W. Eckstein, Sputtering studies with the Monte Carlo Program TRIM.SP, Appl. Phys. A 34 (1984) 73–94.

[15] K. Wasa, I. Kanno, H. Kotera, Handbook of Sputter Deposition Technology: Fundamentals and applications for functional thin films, nano-materials and MEMS, Elsevier/Andrew, Amsterdam, 2012.

[16] S. Mahieu, G. Buyle, D. Depla, S. Heirwegh, P. Ghekiere, R. de Gryse, Monte Carlo simulation of the transport of atoms in DC magnetron sputtering, Nucl. Instrum. Meth. B 243 (2006) 313–319.

[17] D.M. Mattox, Handbook of Physical Vapor Deposition (PVD) Processing, William Andrew, Amsterdam, 2010.

[18] P. Losbichler, C. Mitterer, W.S.M. Werner, H. Störi, J. Barounig, The influence of various process gases on the magnetron sputtering of ZrB_{12}, Thin Solid Films 228 (1993) 56–59.

[19] S. Berg, A.M. Barklund, C. Nender, I.V. Katardjiev, H. Barankova, Sputter erosion amplification, Surf. Coat. Tech. 54-55 (1992) 131–135.

[20] I. Petrov, P.B. Barna, L. Hultman, J.E. Greene, Microstructural evolution during film growth, J. Vac. Sci. Technol. A 21 (2003) 117–128.

[21] ICDD, Card 03-065-7442 for bcc-Mo, 2007.

[22] H. Okamoto, Al-Mo (Aluminum-Molybdenum), J. Phase. Equilib. Diff. 31 (2010) 492–493.

[23] M. Bielawski, Development of unbalanced magnetron sputtered Al–Mo coatings for cadmium replacement, Surf. Coat. Tech. 179 (2004) 10–17.

[24] R.I. Bates, O.A. Abu-Zeid, Deposition of highly supersaturated metastable aluminium-molybdenum alloy by closed field unbalanced magnetron sputtering, Vacuum (1996) 107–111.

[25] Rolf E. Hummel, Electronic Properties of Materials, Springer, New York, 2001

Publication III

Oxidation and wet-etching behaviour of MoAlTi thin films deposited by sputtering from a rotatable MoAlTi compound target

Roland Lorenz, Michael O'Sullivan, Dietmar Sprenger, Bernhard Lang, Harald Köstenbauer, Jörg Winkler, Christian Mitterer

Submitted for publication

Oxidation and wet-etching behaviour of MoAlTi thin films deposited by sputtering from a rotatable MoAlTi compound target

Roland Lorenz[1*], Michael O'Sullivan[2], Dietmar Sprenger[2], Bernhard Lang[2], Harald Köstenbauer[2], Jörg Winkler[2], Christian Mitterer[1]

[1]Department of Physical Metallurgy and Materials Testing, Montanuniversität Leoben, Franz-Josef-Straße 18, 8700 Leoben, Austria

[2]Plansee SE, Metallwerk Planseestraße 71, 6600 Reutte Austria

Abstract

Within the current work, MoAlTi thin films have been deposited by d.c. magnetron sputtering from a cold gas sprayed MoAlTi cylindrical rotatable target. Chemical composition, microstructure, oxidation behaviour, wet etching properties and electrical resistivity of the films are compared to those of a pure Mo reference film. Deviations in the chemical composition of the films with respect to the target are attributed to differences in gas phase scattering of the individual sputtered species. The films deposited are characterized by the formation of a Mo-based body-centred cubic solid solution, resulting in an increased electrical resistivity compared to the pure Mo film. While alloying of Mo films with Al and Ti decreases the wet etching rate in a phosphoric acid-based etching solution, the oxidation behaviour could be significantly improved and the metallic-reflecting surface was maintained after annealing for 1 h at 330°C in air.

Keywords: molybdenum-aluminium-titanium, magnetron sputtering, thin films, cold gas spraying, oxidation resistance, wet etching behaviour

[*] Corresponding author: Mail: roland.lorenz@stud.unileoben.ac.at

1. Introduction

Molybdenum based thin films find versatile applications due to their good thermal, chemical and electrical properties. They are applied as diffusion barriers in microelectronics [1,2] or as a back-contact material in solar cells [1,3–5]. Further, they are used as interconnect material in large-scale integrated circuits and as gate and source/drain signal lines in thin film transistor liquid crystal displays (TFT-LCDs) [1,5–7]. During the manufacturing process of TFTs, the films are exposed to temperatures up to 350°C [8], at which no deterioration of properties should occur. Mo is known to form oxides in air already at 300°C [9,10]. Thus, attempts have recently been reported to alloy Mo-based films with the goal to improve their corrosion and oxidation resistance [11]. Another important step in the TFT manufacturing process is the photolithography process, where film areas not protected by photoresist are selectively removed [8,12]. In particular, Mo is known for its easy pattering in nitric and phosphoric acid solutions [13], which necessitates a careful optimization of oxidation resistance while maintaining a sufficient wet etching rate.

Within the current work, MoAlTi thin films are deposited from a MoAlTi compound rotary target, which was manufactured by cold gas spraying, a novel thermal spray technique [14–16]. Jörg et al. [17], who deposited MoAlTi films by co-sputtering from elemental planar targets, already showed that alloying Al and Ti to Mo-based films improves their oxidation resistance while maintaining an acceptable wet etching behaviour. When depositing such multi-component alloy thin films, the large mass differences between the individual target atoms can lead to a significant deviation in the film composition with respect to the sputter target composition, as shown in our previous work for MoAl films [18]. The variation of the film composition is governed by the applied process pressure [19–21], which determines scattering of sputtered target atoms during the gas phase transport. Consequently, the focus of this study is laid on investigation of the effect of process gas pressure on chemical composition, microstructure, wet chemical etch ability and oxidation resistance of MoAlTi films. The results obtained are compared to pure Mo films.

2. Experimental Details

A series of MoAlTi thin films was deposited in an industrial scale unbalanced d.c. magnetron in-line sputtering system (FHR.Line.600-V) using a cylindrical rotatable MoAlTi target (ø 150 × 600 mm²), manufactured by cold gas spraying. The Al and Ti content of the used target was set to 20.4 at.% and 10.6 at.%, respectively [22]. The films were grown on (100) oriented 20 × 7 × 0.35 mm³ Si substrates, 50 × 50 × 1 mm³ soda-lime glass (SLG) sheets and 50 × 50 × 0.7 mm³ display glass sheets (Corning EAGLE XG), which were ultrasonically cleaned in acetone and ethanol prior to deposition and dried in hot air. After mounting the substrates onto the vertically aligned and grounded substrate carrier, the load-lock chamber was evacuated to a base pressure below 1×10^{-3} Pa. The substrates were then moved via a gate valve into the deposition chamber, where they were plasma etched by oscillating the carrier for 12 cycles in front of a plasma, generated by a radio-frequency power supply (13.56 MHz) at a discharge power of 0.8 kW and an Ar gas pressure of 0.3 Pa. For the subsequent film deposition, the carrier was stationary positioned at a target-substrate distance of about 75 mm in front of the centre of the cylindrical magnetron. The discharge power was kept constant at 8 kW for all depositions, while the Ar gas pressure was systematically varied and set to values of 0.25, 0.42, 0.66, and 1.4 Pa. The deposition time was kept constant at 55 s. To compare the MoAlTi films to a suitable reference, an additional Mo thin film was deposited using a pure Mo cylindrical target under the same deposition parameters at a pressure of 0.66 Pa.

The chemical composition of the MoAlTi films was determined by Elastic Recoil Detection Analysis (ERDA), where the samples have been analysed using a 43 MeV $^{35}Cl^{7+}$ ion beam. The angle between the sample normal and the incoming beam was 75°, the scattering angle was 31°. The analysed area was about 1.5 × 1.5 mm² and the recoiled sample ions were detected by a Bragg Ionization Chamber, which enables energy measurements and atomic number identification of the recoils. The surface morphology as well as the fracture cross-section of the films were investigated with a scanning electron microscope (SEM, Zeiss EVO 50). To characterize the film microstructure, X-ray diffraction (XRD) was used, performed with a Bruker-AXS D8 Advance diffractometer in

grazing incidence geometry with an angle of incidence of 5° and Cu-Kα radiation (λ = 1.5406 Å).

The wet etching rate of the films was evaluated by measuring the weight change of the coated SLG substrates during dissolution of the films in the etchant every 5 s. The weight change per time was converted to a thickness change per time by assuming a linear decrease until the whole film is dissolved. The used phosphoric acid-based etchant (PAN-etchant) was composed of 66 wt.% phosphoric acid, 10 wt.% acetic acid and 5 wt.% nitric acid. Etching was carried out at a stirring rate of 300 rpm and a temperature of 40°C. By annealing the Mo and MoAlTi films in a chamber furnace at 330°C in air, the oxidation behaviour of the films was investigated. To compare the optical properties before and after annealing, the reflectance spectra were measured for the wavelength range between 250 and 850 nm with 2 nm intervals using a PerkinElmer-LAMBDA 950 UV/Vis/NIR spectrometer with a W-set up. A Jandel RM2 four point probe was used to measure the electrical sheet resistivity of the films.

3. Results and Discussion

Figure 1 shows the atomic ratios of the individual elements within the MoAlTi films, as determined by ERDA, together with those of the used target (dashed lines). The atomic ratio of the films differs from that of the target. In addition, the Ar gas pressure clearly affects the film composition. As already shown in our previous investigation [18], individual sputtered species can be lost due to gas phase scattering during the gas phase transport towards the substrates. Light elements like Al (compared to Mo) undergo a more efficient thermalization, since they are easily scattered during collisions with the Ar background gas. This is expressed by the energy transfer coefficient ε

$$\varepsilon = \frac{4\, m_1\, m_2}{(m_1 + m_2)^2}\,, \qquad (1)$$

which reaches its maximum when the mass of the sputtered target atom m_2 is similar to the mass of Ar (m_1) [23]. Consequently, sputtered Al atoms with ε = 0.96 quickly lose their kinetic energy during collisions with Ar, while the energy transfer from Mo to Ar is with ε = 0.83 much less efficient [19,20,23]. The differences in energy transfer seem to

govern the scattering characteristics rather than the respective different mean free path for Mo and Al in Ar (see Table 1). Because of the high mass of Mo atoms, the number of collisions required for thermalization is high and they might thus be able to widely retain their initial direction towards the substrate after colliding with an Ar atom. Light atoms like Al are known to be scattered in large angles and they rapidly lose their kinetic energy [24]. Figure 1 indicates that a maximum decrease of Al of ~7 at.% compared to the target composition could be found for the 0.25 Pa deposition. The subsequent rise of the Al content with the simultaneous decline of the Mo content with increasing Ar gas pressure can be explained by the three different regimes occurring during transport through a gas phase, as originally described by Rossnagel et al. [19] and later-on by Bundaleski et at. [20]. First, in the ballistic regime at low pressure conditions hardly any collisions occur; thus, the film composition largely represents the target composition. In the intermediate regime, lighter elements will be increasingly scattered, shifting the film composition towards the heavier element. A further rise of the pressure leads to the third, the diffusive regime, where the heavier elements are efficiently scattered as well, resulting in a rise of the fraction of the lighter elements within the film. Consequently, we assume that the 0.25 and 0.42 Pa depositions correspond to the intermediate regime, whereas for the 0.66 and 1.4 Pa depositions the diffusive regime is dominating. This interpretation is also supported by the low mean free path values given in Table 1, which enable several collisions within the used target-substrate distance of 75 mm. The Ti content within the films, with values between 1.3 (0.42 Pa) and 4.7 at.% (1.4 Pa) is higher than within the target. Both, sputter yield and surface binding energy of Ti do not indicate a preferential sputtering of Ti (see Table 1). In addition, due to mass conservation the flux of sputtered species leaving the target surface can be assumed to correspond quickly to the target composition. Also the energy transfer coefficient and the mean free path given in Table 1 infer that Ti atoms at a given Ar gas pressure are efficiently scattered by collisions with Ar during the transport phase. Thus, the enhanced Ti fraction in the films with respect to the target (see Figure 1) should stem from differences in condensation and film growth. Apart from that, a slight increase of the Ti content can be observed between 0.25 and 1.4 Pa similar to the increase of Al. This increase may also be referred to the different gas phase transport regimes occurring,

but less pronounced since the mass difference between Mo and Ti is smaller than that between Mo and Al.

Table 1: *Physical properties of Mo, Al and Ti relevant to sputtering.*

		Mo	Al	Ti
Atomic mass [u] [25]		95.95	26.98	47.87
Atomic radius [pm] [26]		145	125	140
Energy transfer coefficient ε [23]		0.83	0.96	0.99
Surface binding energy [eV] [27]		6.86	3.36	4.90
Sputter yield (Ar^+, 300 eV) [27]		0.58	0.65	0.33
Mean free path [mm] [28]	0.25 Pa	61	106	80
	1.4 Pa	11	19	14

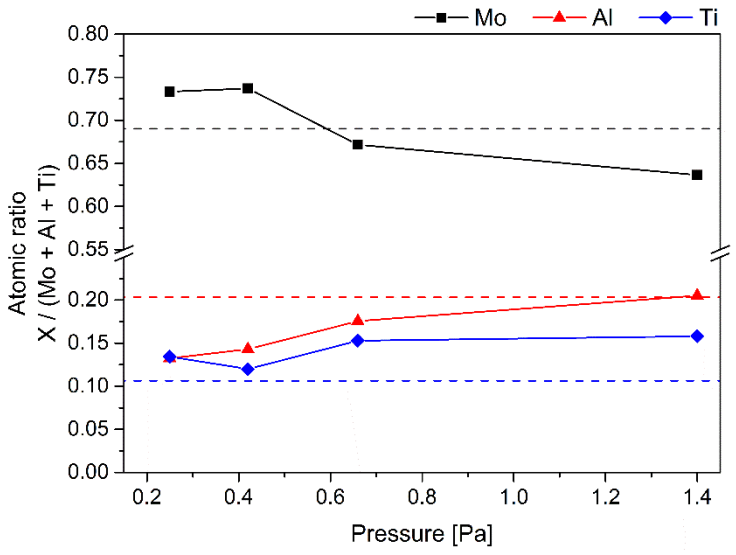

Figure 1: *Chemical composition of the synthesized MoAlTi films on Si substrates as a function of the Ar gas pressure. The target composition is indicated by the dashed lines.*

SEM top view images and cross-sectional images of a Mo reference and a MoAlTi film, both deposited at an Ar gas pressure of 0.66 Pa, are displayed in Figure 2. All films

possess a smooth surface with a few scattered droplets. The fracture cross-sections indicate that the films show a dense and fine-columnar structure, which is attributed to the zone T within the structure zone model for thin film growth [29]. The thicknesses of the MoAlTi films vary between 245 nm for the film grown at 1.4 Pa and 308 nm for the film grown at 0.42 Pa, which corresponds to film growth rates of 4.5 nm/sec and 5.6 nm/sec, respectively. The lower film thickness for the higher pressure can be explained by the decreased mean free path of the sputtered elements in the Ar background gas (Table 1) and the therefore enhanced gas phase scattering. The Mo film shows a similar film thickness of 292 nm with a growth rate of 5.3 nm/sec.

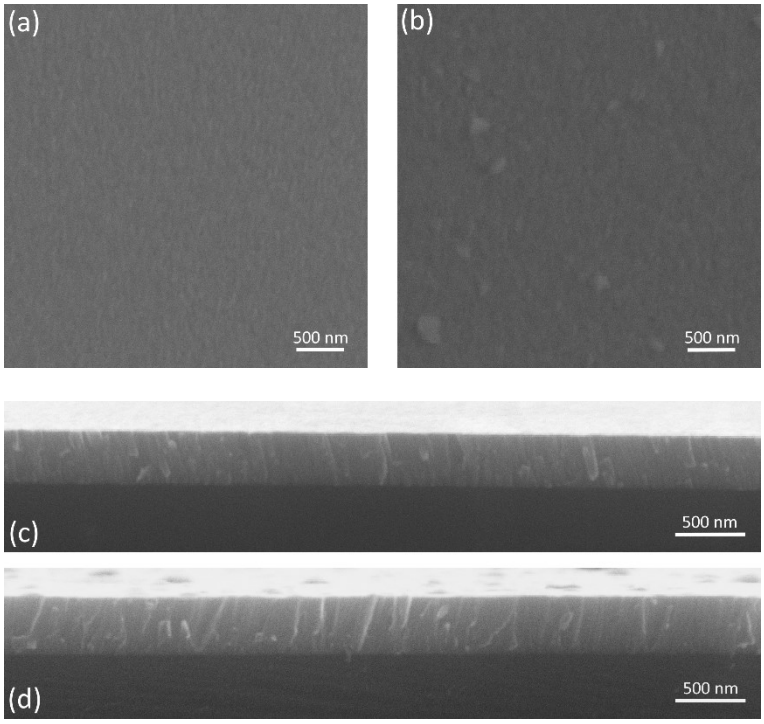

Figure 2: *SEM top view and fracture cross-section images of (a),(c) Mo and (b),(d) MoAlTi films deposited at 0.66 Pa onto Si substrates.*

In Figure 3 (a), the X-ray diffractograms of the MoAlTi films deposited at the different pressure conditions are summarized together with that obtained for the Mo film grown at 0.66 Pa. All films are characterized by the formation of a single-phase body-centred cubic (bcc) structure characteristic for a Mo-based solid solution. The diffraction peaks show a good agreement with those of pure Mo at $2\Theta = 40.50°$, 58.62°, 73.68°, and

87.63° [30]. Indications for the formation of intermetallic phases could not be found, although several phases exist within the binary systems Mo-Al [31] and Ti-Al [32]. In the enlarged illustration of the (110) peak in Figure 3 (b), a pressure-dependent peak shift with respect to the Mo reference position is obvious. At low pressure, the peak is shifted towards lower angles while with increasing pressure the diffraction peaks shift towards higher angles. The peak shift, and therefore the change of the lattice parameter, may be related to internal stresses within the films. Compressive stresses are common for films grown at low pressure conditions due to energetic particle bombardment during growth [33]. On the other hand, the Al content within the films increases with increasing pressure (see Figure 1) and leads consequently to a decreasing lattice parameter due to the incorporation of the smaller Al atoms (see Table 1) within the bcc lattice, shifting the diffraction peaks to higher angles. Comparing the peak heights of the alloyed films with the peak heights of the Mo film, no significant differences could be found, indicating that alloying does not alter the preferred orientation of the films.

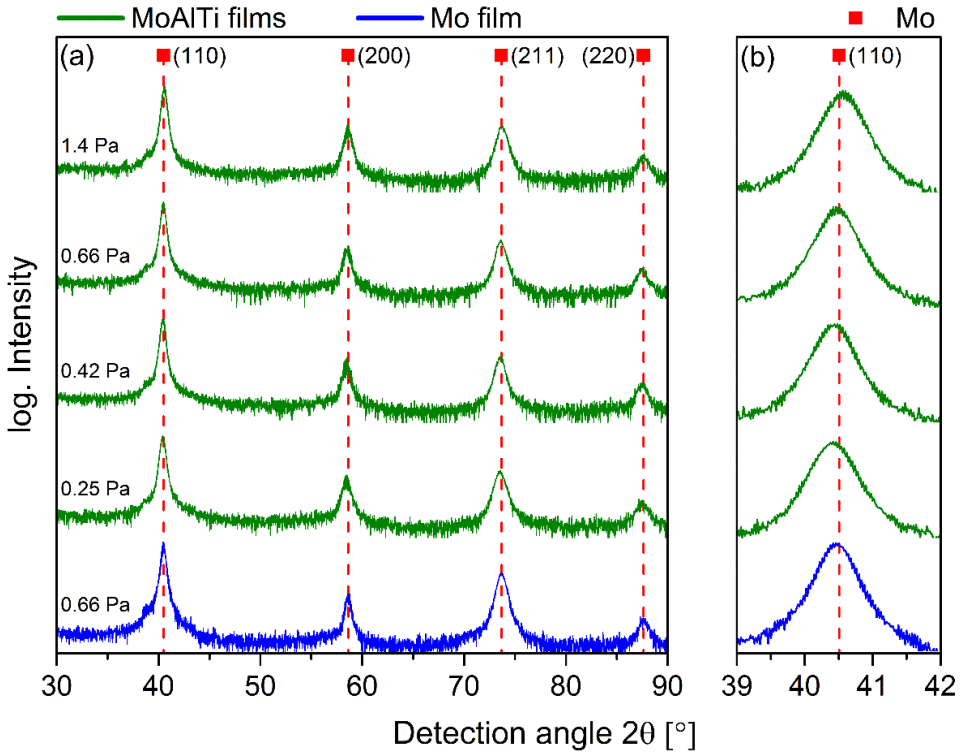

Figure 3: *(a) X-ray diffractograms of Mo and MoAlTi films grown at different Ar gas pressures on Si substrates; (b) enlarged detail of the (110) peak. The red squares indicate the diffraction peaks of pure Mo [30].*

The wet etching rates obtained for the four MoAlTi films and the Mo reference film dissolved in the PAN-etchant are displayed in Figure 4. The etching rate of the Mo film with roughly 14 nm/s is by a factor between 2 to 4 considerable higher than those of the MoAlTi films. Mo films are known to be easily etched by nitric and phosphoric acid solutions; however, also acetic acid, which is often used as a pH buffer component in the wet etchant solution, is able to dissolve Mo and to stabilize dissolved Mo ions in the solution [13,34]. The significant decrease of the wet etching rate of the MoAlTi films with respect to the pure Mo film can be attributed to the incorporation of Al. Wang et al. [35] and Kim et al. [36] showed for Mo/Al stacked films that the less noble Al protects the nobler Mo, since Mo can act as a cathode during the etching reaction, resulting in a supressed dissolution of the films. Although there might be possible differences in corrosion mechanisms between these layered films and the solid solution systems investigated within this work, the decrease of the etching rate observed between 0.42 and 1.4 Pa might be related to the increasing Al content of the films (see Figure 1). Investigations on the corrosion behaviour of Mo-Ti films by Park et al. [37] showed that Ti is corrosion resistant in oxidizing etching media. In the applied PAN etching solution, the nitric acid usually oxidizes the metals first, whereas the phosphoric acid then dissolves the resulting oxides [38]. Thus, Ti may further decrease the etching rate of the MoAlTi films with respect to the Mo film.

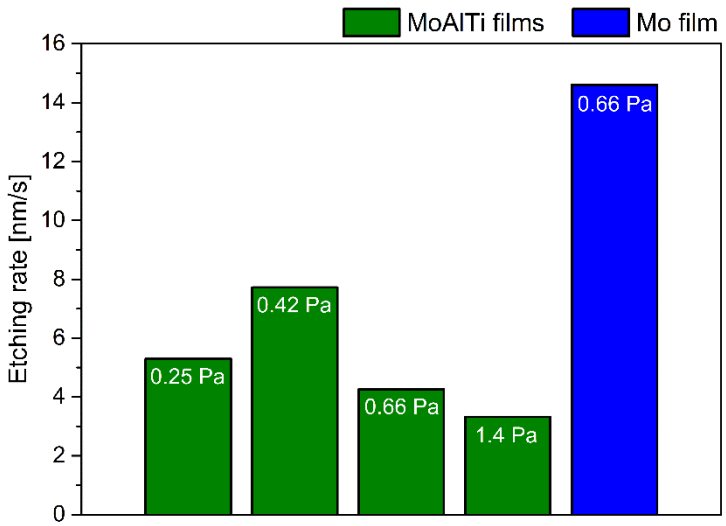

Figure 4: *Wet etching rate of the Mo and MoAlTi films, grown at different Ar gas pressures on SLG substrates, in PAN etching solution.*

The reflectivity spectra obtained for the films in the as-deposited state and after annealing for 1 h at 330°C in air are summarized in Figure 5. In the as-deposited state, all films possess a metallic-reflecting surface with reflectivity values, depending on the wavelength, between 35 and 60 % (see also Figure 6). By annealing the films, the reflectivity decreases significantly for the Mo film but also for those MoAlTi films grown at 0.25 and 0.42 Pa, with a minimum value at a wavelength of ~320 nm. With the increased alloy content for the MoAlTi films grown at 0.66 and 1.4 Pa, the reflectivity spectra after annealing are closer to the curves of the as-deposited films, retaining a minimum reflectivity of at least 10 % at wavelengths below 500 nm. As evidenced by Figure 6, annealing of the Mo reference and those MoAlTi films grown at low pressures leads to the formation of a coloured, yellowish surface. The colour change is attributed to the formation of Mo oxides, in particular MoO_3 which is formed in air at ~300°C [9,10]. The yellow colour stems from the low reflectivity of the films in the violet and blue light range (< 500 nm, see Figure 5). As indicated by the reflectivity spectra, the two MoAlTi films deposited at 0.66 and 1.4 Pa appear darker compared to the as-deposited state, but maintain their metallic-reflecting surface. This behaviour can again be explained by the increased Al content within these films, as Al is known to form a dense alumina layer on the film surface, protecting the Mo against oxidation [39,40].

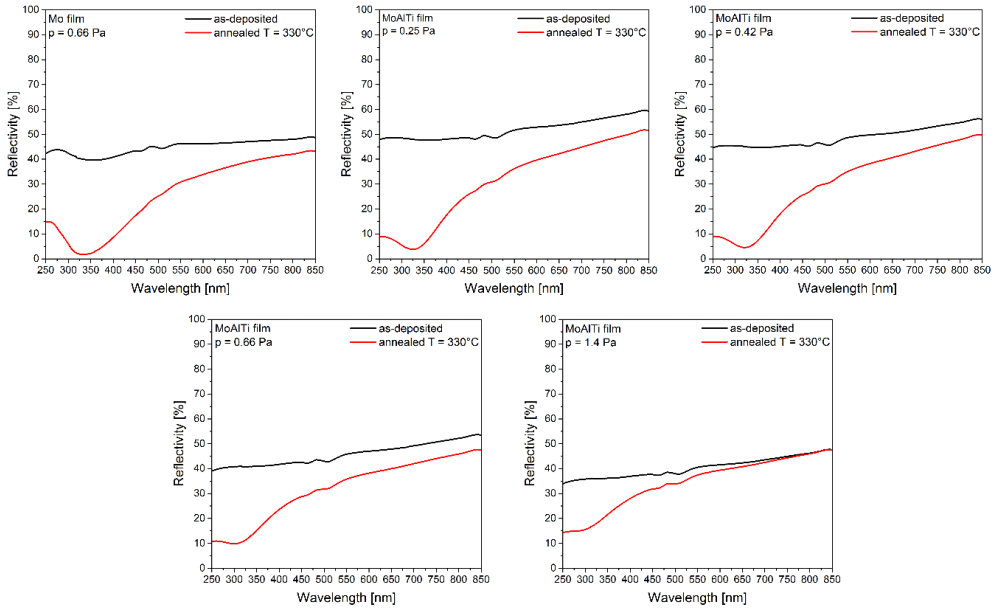

Figure 5: *Reflectivity spectra of the Mo and MoAlTi films, grown at different Ar gas pressures on Corning EAGLE XG glass sheets, in the as-deposited state (black lines) and after annealing in air for 1 h at 330°C (red lines).*

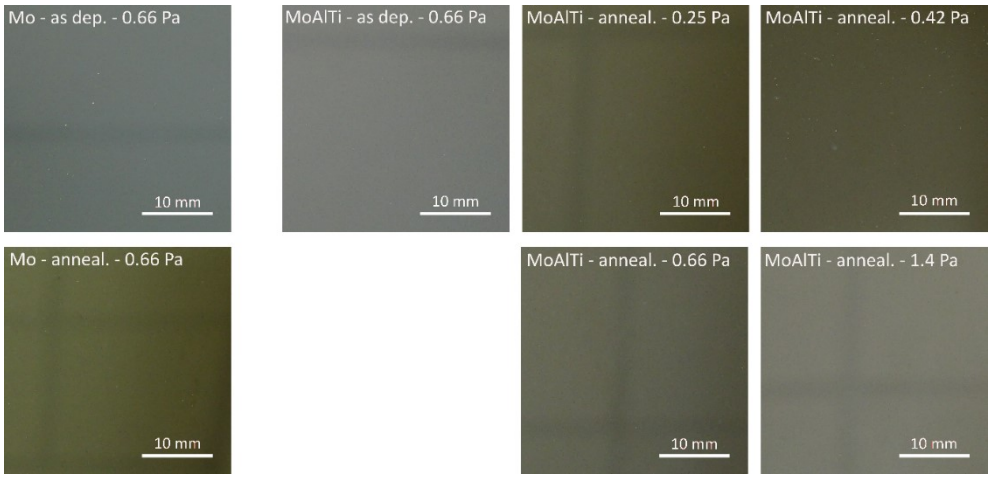

Figure 6: *Pictures of Mo and MoAlTi films, grown at different Ar gas pressures on Corning EAGLE XG glass sheets, in the as-deposited state and after annealing in air for 1 h at 330°C.*

The electrical sheet resistivity as a function of the Ar gas pressure determined by four point probe measurements is displayed in Figure 7. With a resistivity of 11 µΩcm, the Mo film shows good agreement with values known from literature [6,7]. Alloying the films with Ti and Al and thus formation of the bcc Mo-based solid solution leads to an increase of the electrical sheet resistivity to values between 83 and 89 µΩcm. With the exception of the slight rise between 0.25 and 0.42 Pa, the resistivity stays approximately constant over the whole pressure range applied. The higher resistivity can be explained by the addition of atoms of different sizes within the bcc Mo-based solid solution, leading to local strains and the observed variation of the lattice parameter (see Figure 3 (b)), which results in pronounced electron scattering. Further, the alloying elements are characterized by different valences (Al: 3; Ti: 4) compared to Mo (6), which introduces a local charge difference resulting in an additional increase of the electron scatter probability and therefore increasing resistivity [41].

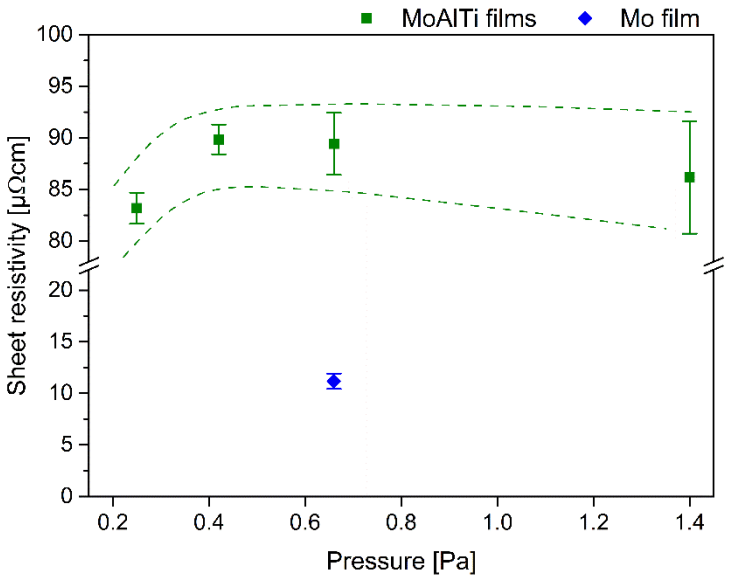

Figure 7: *Electrical sheet resistivity of the Mo and MoAlTi films on Si substrates as a function of the Ar gas pressure. The dashed green lines are added as guide for the eye.*

4. Conclusion

MoAlTi thin films have been synthesized by d.c. magnetron sputtering from a MoAlTi compound cylindrical rotatable target, manufactured by cold gas spraying. Chemical composition, microstructure as well as electrical resistivity, oxidation- and wet etching behaviour of the films have been investigated and compared to a pure Mo reference film. With increasing Ar gas pressure, a significant deviation of the MoAlTi film composition from the target composition could be observed, which can mainly be explained by the changing scattering behaviour of the individual sputtered species during the gas phase transport. The MoAlTi films, which are characterized by a Mo-based single phase solid solution, show a decreased wet etching rate in a phosphoric acid-based etchant with a minimum value of ~3 nm/s compared to the pure Mo film with ~14 nm/s. The less noble Al and the corrosion resistant Ti enhance the films' resistance against dissolution. With an increasing Ar gas pressure and therefore increasing Al and Ti contents within the films, the oxidation behaviour could be improved, as evidenced by an optical shift from yellowish to a metallic-reflecting surface after annealing at 330°C for 1 h in air. The Ar gas pressure enables adjustment of the chemical composition of films deposited from a compound target, and provides a path

to fine-tune film properties including the oxidation resistance and wet etching behaviour.

5. Acknowledgments

This work was supported by the Österreichische Forschungsförderungsgeslleschaft FFG within the project "E²CGS" (Project No. 150130). ERDA measurement were performed at the "Helmholtz Zentrum Dresden Rossendorf" in Dresden, Germany.

6. References

[1] T. Jörg, M.J. Cordill, R. Franz, C. Kirchlechner, D.M. Többens, J. Winkler, C. Mitterer, Thickness dependence of the electro-mechanical response of sputter-deposited Mo thin films on polyimide: Insights from in situ synchrotron diffraction tensile tests, Mater. Sci. Eng. 697 (2017) 17–23.

[2] Y.-W. Yen, Y.-L. Kuo, J.-Y. Chen, C. Lee, C.-Y. Lee, Investigation of thermal stability of Mo thin-films as the buffer layer and various Cu metallization as interconnection materials for thin film transistor–liquid crystal display applications, Thin Solid Films 515 (2007) 7209–7216.

[3] Z.-H. Li, E.-S. Cho, S.J. Kwon, Molybdenum thin film deposited by in-line DC magnetron sputtering as a back contact for Cu(In,Ga)Se_2 solar cells, Appl. Surf. Sci. 257 (2011) 9682–9688.

[4] J.H. Scofield, A. Duda, D. Albin, B.L. Ballard, P.K. Predecki, Sputtered molybdenum bilayer back contact for copper indium diselenide-based polycrystalline thin-film solar cells, Thin Solid Films 260 (1995) 26–31.

[5] J.A. Shields, Applications of Molybdenum Metal and Its Alloys, International Molybdenum Association (IMOA), London, 2013.

[6] A.M. Hofer, J. Schlacher, J. Keckes, J. Winkler, C. Mitterer,Sputtered molybdenum films: Structure and property evolution with film thickness, Vacuum 99 (2014) 149–152.

[7] T. Jörg, M.J. Cordill, R. Franz, O. Glushko, J. Winkler, C. Mitterer, The electro-mechanical behavior of sputter-deposited Mo thin films on flexible substrates, Thin Solid Films 606 (2016) 45–50.

[8] S.D. Brotherton, Introduction to Thin Film Transistors, Physics and Technology of TFTs, Springer, Heidelberg, 2013.

[9] L. Mele, F. Santagata, E. Iervolino, M. Mihailovic, T. Rossi, A.T. Tran, H. Schellevis, J.F. Creemer, P.M. Sarro, A molybdenum MEMS microhotplate for high-temperature operation, Sensor. Actuat. A-Phys. 188 (2012) 173–180.

[10] F. Ullmann, R.F. Sebenik, A.R. Burkin, R.R. Dorfler, J.M. Laferty, G. Leichtfried, H. Meyer-Grünow, M.S. Vukasovich, D.A. Church, G.G. Van Riper, J.C. Gilliland, S.A. Thielke, Ullmann's Encyclopedia of Industrial Chemistry: Molybdenum and Molybdenum Compounds, Wiley-VCH Verlag GmbH & Co. KGaA, Weinheim, 2005.

[11] A. List, C. Mitterer, G. Mori, J. Winkler, N. Reinfried, W. Knabl, Oxidation of sputtered thin films of molybdenum alloys at ambient conditions, Proceedings of the 17th Plansee Seminar (2009) RM 12/1-9.

[12] E. Fortunato, P. Barquinha, R. Martins, Oxide semiconductor thin-film transistors: A review of recent advances, Adv. Mater. 24 (2012) 2945–2986.

[13] J.H. Seo, Electrochemical analysis of sputtered molybdenum thin films on glass substrates in various acid solutions, J. Korean Phys. Soc. 50 (2007) 1193.

[14] S. Grigoriev, A. Okunkova, A. Sova, P. Bertrand, I. Smurov, Cold spraying: From process fundamentals towards advanced applications, Surf. Coat. Tech. 268 (2015) 77–84.

[15] T. Schmidt, H. Assadi, F. Gärtner, H. Richter, T. Stoltenhoff, H. Kreye, T. Klassen, From particle acceleration to impact and bonding in cold spraying, J. Therm. Spray. Tech. 18 (2009) 794–808.

[16] T.H. van Steenkiste, J.R. Smith, R.E. Teets, J.J. Moleski, D.W. Gorkiewicz, R.P. Tison, D.R. Marantz, K.A. Kowalsky, W.L. Riggs, P.H. Zajchowski, B. Pilsner, R.C. McCune, K.J. Barnett, Kinetic spray coatings, Surf. Coat. Tech. 111 (1999) 62–71.

[17] T. Jörg, A.M. Hofer, H. Köstenbauer, J. Winkler, C. Mitterer, Oxidation and wet etching behavior of sputtered Mo-Ti-Al films, J. Vac. Sci. Technol. A 36 (2018) 21513.

[18] R. Lorenz, M. O'Sullivan, D. Sprenger, B. Lang, C. Mitterer, Chemical composition and properties of MoAl thin films deposited by sputtering from MoAl compound targets, J. Vac. Sci. Technol. A 35 (2017) 41504.

[19] S.M. Rossnagel, I. Yang, J.J. Cuomo, Compositional changes during magnetron sputtering of alloys, Thin Solid Films 199 (1991) 59–69.

[20] N. Bundaleski, S. Petrović, D. Peruško, J. Kovač, A. Zalar, Composition of the sputter deposited W–Ti thin films, Appl. Surf. Sci. 254 (2008) 6390–6394.

[21] J. Neidhardt, S. Mráz, J.M. Schneider, E. Strub, W. Bohne, B. Liedke, W. Möller, C. Mitterer, Experiment and simulation of the compositional evolution of Ti–B thin films deposited by sputtering of a compound target, J. Appl. Phys. 104 (2008) 63304.

[22] H. Köstenbauer, J. Köstenbauer, G. Leichtfried, J. Winkler, M.S. Hwang, M. Kathrein, E. Eidenberger, Metallization for a thin-film component, process for the production thereof and sputtering target, Plansee SE, 14.09.2017, US Patent Application US 2017/0260622 A1.

[23] P.M. Martin, Handbook of Deposition Technologies for Films and Coatings: Science, Applications and Technology, 3rd ed., Elsevier, Amsterdam, Boston, 2010.

[24] W.D. Westwood, Sputter Deposition, Education Committee, AVS, New York, 2003.

[25] J. Meija, T.B. Coplen, M. Berglund, W.A. Brand, P. de Bièvre, M. Gröning, N.E. Holden, J. Irrgeher, R.D. Loss, T. Walczyk, T. Prohaska, Atomic weights of the elements 2013 (IUPAC Technical Report), Pure Appl. Chem. 88 (2016) 201.

[26] Reade International Corp., Atomic radii of the elements, 2016, http://www.reade.com/reade-resources/reference-educational/reade-reference-chart-chemical-elements-data/8-atomic-radii-of-the-elements, accessed 10 January 2018, and J.C. Slater, Atomic radii in crystals, J. Chem. Phys. 41 (1964) 3199-3204.

[27] K. Wasa, I. Kanno, H. Kotera, Handbook of Sputter Deposition Technology: Fundamentals and Applications for Functional Thin Films, Nanomaterials and MEMS, 2nd ed., Elsevier/Andrew, Amsterdam u. a., 2012.

[28] S. Mahieu, G. Buyle, D. Depla, S. Heirwegh, P. Ghekiere, R. de Gryse, Monte Carlo simulation of the transport of atoms in DC magnetron sputtering, Nucl. Instrum. Meth. B 243 (2006) 313–319.

[29] I. Petrov, P.B. Barna, L. Hultman, J.E. Greene, Microstructural evolution during film growth, J. Vac. Sci. Technol. A 21 (2003) S117-S128.

[30] ICDD, Card 03-065-7442 for bcc-Mo, 2007.

[31] H. Okamoto, Al-Mo (Aluminum-Molybdenum), J. Phase Equilib. Diffus. 31 (2010) 492–493.

[32] I. Ohnuma, Y. Fujita, H. Mitsui, K. Ishikawa, R. Kainuma, K. Ishida, Phase equilibria in the Ti–Al binary system, Acta Mater. 48 (2000) 3113–3123.

[33] S. Tamulevičius, Stress and strain in the vacuum deposited thin films, Vacuum 51 (1998) 127–139.

[34] K.R. Williams, K. Gupta, M. Wasilik, Etch rates for micromachining processing-part II, J. Microelectromech. Syst. 12 (2003) 761–778.

[35] Y.-C. Wang, W.-H. Lu, H.-B. Chen, S.-C. Yen, Synergetic effect of aluminum and Mo⁄Al etching in phosphoric acid-based etchant with nitric acid, J. Electrochem. Soc. 159 (2012) D103.

[36] I.S. Kim, S. Chon, K.S. Kim, I.C. Jeon, Dissolution of Mo/Al bilayers in phosphoric acid, Bulletin of the Korean Chemical Society 24 (2003) 1613–1617.

[37] P.Y. Park, E. Akiyama, H. Habazaki, A. Kawashima, K. Asami, K. Hashimoto, The corrosion behavior of sputter-deposited Mo-Ti alloys in concentrated hydrochloric acid, Corros. Sci. 38 (1996) 1649–1667.

[38] MicroChemicals GmbH, Aluminium etching, www.microchemicals.com/downloads/application_notes.html, accessed 1 December 2017.

[39] D. Nilsson, N. Stavlid, M. Lindquist, S. Hogmark, U. Wiklund, The role of aluminum additions in the oxidation and wear of a TaC:C low-friction coating, Surf. Coat. Tech. 203 (2009) 2989–2994.

[40] J.F. Yang, Z.G. Yuan, Q. Liu, X.P. Wang, Q.F. Fang, Characterization of Mo–Al–N nanocrystalline films synthesized by reactive magnetron sputtering, Mater. Res. Bull. 44 (2009) 86–90.

[41] R.E. Hummel, Electronic Properties of Materials, 3rd ed., Springer, New York, 2001.

Publication IV

A comparative study on NbO_x films reactively sputtered from sintered and cold gas sprayed targets

Roland Lorenz, Michael O'Sullivan, Alexander Fian, Dietmar Sprenger, Bernhard Lang, Christian Mitterer

Applied Surface Science 436 (2018) 1157-1162

A comparative study on NbO_x films reactively sputtered from sintered and cold gas sprayed targets

Roland Lorenz[1*], Michael O'Sullivan[2], Alexander Fian[3], Dietmar Sprenger[2], Bernhard Lang[2], Christian Mitterer[1]

[1] Department of Physical Metallurgy and Materials Testing, Montanuniversität Leoben, Franz-Josef-Straße 18, 8700 Austria

[2] Plansee SE, Metallwerk-Plansee-Straße 71, 6600 Reutte, Austria

[3] Institute for Surface Technologies and Photonics, Joanneum Research Forschungsgesellschaft mbH, Franz-Pichler-Straße 30, 8160 Weiz, Austria

Abstract

The aim of this work is to evaluate novel cold gas sprayed Nb targets in a reactive sputter deposition process of thin films with respect to the widely used sintered Nb targets. With the exception of a higher target discharge voltage of ~100 V for the cold gas sprayed targets and the thus higher film growth rate compared to sintered targets, NbO_x films with comparable microstructure and properties were obtained for both target variants. The amorphous films with thicknesses between 2.9 and 4.9 µm present an optical shift from dark and non-transparent towards transparent properties, as the oxygen partial pressure increases. X-ray photoelectron spectroscopy confirms the occurrence of the Nb^{5+} oxidation state for the highest oxygen partial pressure, while Nb^{4+} is additionally present at lower oxygen partial pressure settings. With a maximal transparency of ~80% and a refractive index of ~2.5, the transparent films show characteristics similar to Nb_2O_5.

Keywords: niobium oxides, reactive magnetron sputtering, thin films, cold gas spraying, target comparison

[*] Corresponding author: Mail: roland.lorenz@unileoben.ac.at

1. Introduction

For the deposition of functional thin films, magnetron sputtering plays a key role and thus a huge variety of sputter targets manufactured by different techniques are available. Manufacturing routes include vacuum melting and casting or powder metallurgical techniques like sintering. Among the latter, hot isostatic pressing and hot pressing yield the most dense targets [1–3]. The different production techniques affect the target properties such as target material purity and density, which then influence the properties of the synthesized films since pores and voids can act as virtual leaks and contamination sources [1,3]. Systematic investigations on the influence of target properties on the deposition process as well as on the thin film characteristics are rarely found in literature. Lo et al. [4] reported that an increasing tungsten target density decreases film stresses and electrical resistivity, while the target erosion rate and film deposition rate increase. Gehman et al. [5] pointed out that an increased impurity level in indium-tin oxide targets raises the film resistivity and that a higher target density enhances the deposition rate.

A recently introduced possibility to create sputter targets by powder metallurgical techniques is cold gas spraying (CGS). CGS is a thermal spray technique, which is used to deposit a dense and solid thick coating by accelerating a metallic powder in a high velocity gas jet. There, the powder particles are not melted or thermally softened prior to the impact onto the substrate and deposition occurs only by the deformation of solid particles. The high kinetic energy of the powder particles leads to low oxygen contents within the sprayed coatings [6–9], thus making them potential candidates for sputter targets.

Within this work, the sputter performance of niobium (Nb) targets, produced by either conventional sintering or CGS, in a reactive argon/oxygen atmosphere as well as microstructure and properties of the deposited niobium oxide films are investigated and compared.

2. Experimental details

Two different types of Nb targets (ø 50.8 × 6 mm²) were used for the present investigation, in particular (i) commercially available, conventionally sintered targets, which will be named SI targets in the following, and (*ii*) cold gas sprayed targets, denominated as CGS targets. Within the CGS process, the Nb powder was accelerated in a tempered and high pressurized nitrogen gas jet using a de-Laval type nozzle. The fused and crushed Nb powder particles with a grain size between 5 and 45 µm were sprayed onto a 4 mm thick Ti plate up to a coating thickness of 2 mm. To examine the structure of the CGS coating, a metallographically prepared cross-section was investigated by light optical microscopy (LOM, Zeiss Axio Imager) and the target density was determined with an Archimedes balance.

Two targets per target variant were mounted to magnetrons focused to the substrate holder in a laboratory-scale unbalanced d.c. magnetron sputter deposition system, described in detail in refs. [10,11]. The films were grown on 21 × 7 × 1 mm³ soda-lime glass (SLG), 21 × 7 × 0.5 mm³ Si (100) substrates and 50 × 50 × 1 mm³ display glass sheets (Corning EAGLE XG), which were ultrasonically cleaned in acetone and ethanol and dried in hot air prior to deposition. The substrate rotation was set at 50 rpm and the vacuum base pressure was kept below 2×10^{-3} Pa. To remove possible contaminations, the substrates were plasma etched in pure argon atmosphere using a pulsed d.c. discharge at -500 V and 50 kHz for 10 min. A constant target current of 0.35 A was applied per magnetron in a current-controlled mode for a deposition time of 60 min. The NbO_x films were grown in a reactive argon/oxygen atmosphere at a constant total pressure of 0.5 Pa. To deposit films with comparable properties from both target types, the oxygen partial pressure, determined from gas flow calibration curves, was varied between $p(O_2)$ = 40.8% and 48.2% for the SI targets and between $p(O_2)$ = 54.7% and 63.1% for the CGS targets, as shown in Table 1. An asymmetric pulsed d.c. bias of -50 V was applied to the unheated substrate holder with a pulse frequency of 50 kHz, leading to a negative pulse duration of 19.5 µs. The positive pulse, pre-set from the ENI RPG 50 power supply at +37 V, had a duration time of 0.5 µs.

To investigate film composition and morphology, a scanning electron microscope (SEM, Carl Zeiss NTS Ultra plus) equipped with an energy-dispersive X-ray spectroscope (EDX, EDAX Trident XM4) using built-in sensitivity factors was applied. The oxidation states and binding energies of Nb and O for selected films were studied by X-ray photoelectron spectroscopy (XPS) using an Omicron Multiprobe surface analysis system with a DAR 400 X-ray source with an Al-Kα beam and an excitation energy of 1486.7 eV, an XM 500 quartz crystal monochromator and an EA 125 hemispherical electron energy analyser with a 5 channel pulse counting channeltron at a pass energy of 20 eV. The total energy resolution of the system (excitation source, analyser) is 0.5 eV. The binding energy was corrected by using the C-C bond of the C1s peak of residual hydrocarbon surface contaminants at 284.6 eV as reference. Measurements were performed in the as-received state under three different detection angles of 0°, 35° and 50° to the surface normal. The subsequent fitting of the spectral line shape was performed by convolution of Gaussian and Lorentzian functions. X-ray diffraction (XRD) measurements were performed using a Bruker-AXS D8 Advance diffractometer in grazing incidence geometry with an angle of incidence of 5° and Cu-Kα radiation (λ = 1.5406 Å). The reflectance and transmittance spectra were recorded for wavelengths of 250-850 nm with 2 nm intervals using a PerkinElmer-LAMBDA 950 UV/Vis/NIR spectrometer with W- and V-setup, respectively.

Table 1: *O_2 gas flow and the resulting oxygen partial pressure used for film deposition from SI and CGS targets.*

SI targets					
O_2 flow [sccm]	8	8.5	9	9.5	10
$p(O_2)$ [%]	40.8	42.4	44.6	46.0	48.2
CGS targets					
O_2 flow [sccm]	12	13	13.5	14	15
$p(O_2)$ [%]	54.7	57.6	58.6	60.4	63.1

3. Results and discussion

The ground and polished cross-section of a CGS target is displayed in Figure 1. Beside isolated pores and voids, the target appears dense. The size of the pores ranges up to a maximum of ~10 µm, as illustrated in the enlarged inset in Figure 1. The scratches visible in Figure 1 stem from the grinding and polishing process. The density of the CGS targets corresponds with 8.43 g/cm³ to 98.4% of the bulk density of Nb (ρ_{Nb} = 8.57 g/cm³ [12]), which fits to findings for CGS Nb in literature where porosity values of ~0.3% have been reported [13]. For comparison, the SI targets are with 8.57 g/cm³ fully dense.

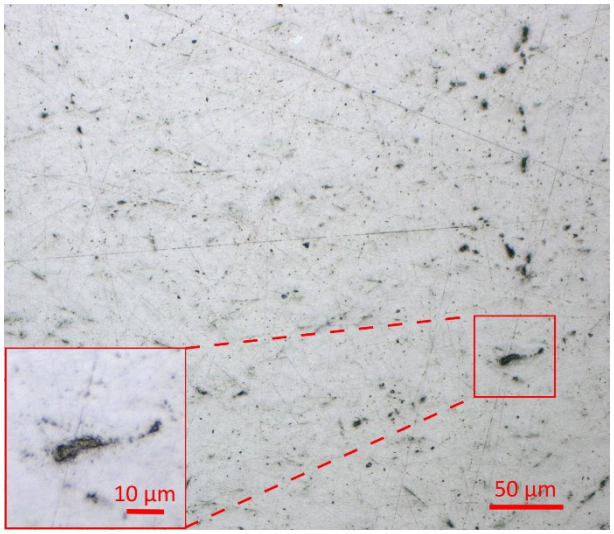

Figure 1: *LOM cross-sectional micrograph of the CGS target.*

Figure 2 illustrates the film growth rate and the applied target voltage as a function of the increasing oxygen partial pressure for both target variants. The target voltage continuously rises with increasing oxygen partial pressure, while the growth rate significantly drops for the highest partial pressures applied. Both changes are attributed to target poisoning, where an oxide layer is formed on the target surface, which significantly reduces the electrical conductivity of the target surface [1,2,14]. The target voltage for the CGS targets lies ~100 V above the one of the SI targets, although the same target current of 0.35 A was applied. This behaviour can be explained by the design of the CGS targets. There, on the one hand, Ti was used as a target backing plate for the CGS process, where the Ti has a significantly higher electrical resistivity of 42 µΩcm [15]

compared to Nb with 15.22 µΩcm [12]. On the other hand, the CGS coatings can be assumed to have a lower electrical conductivity than dense bulk materials due to their low grain size and the existence of pores [16], as evidenced by Figure 1. In the current-controlled sputter mode applied within this study, the observed higher target voltage for the CGS compared to the SI targets leads to a higher kinetic energy of argon ions impinging on the target surface, resulting in an enhanced sputter and film growth rate [2]. This assumption was confirmed by the observed higher thickness of the films deposited from the CGS with respect to the SI targets for the same deposition time.

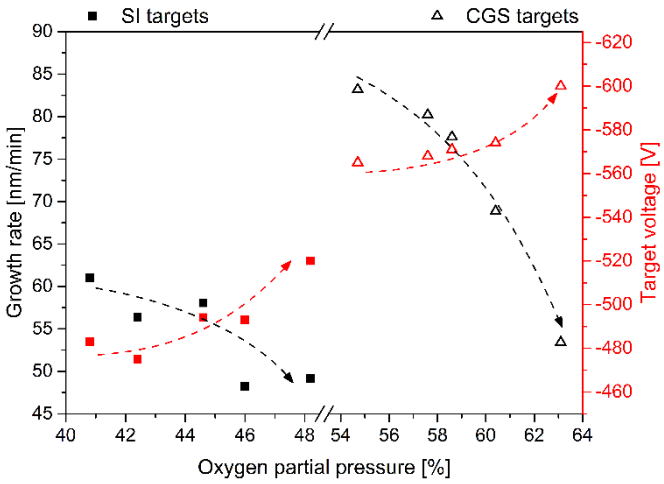

Figure 2: *Growth rate and target voltage as a function of the oxygen partial pressure for the deposition from SI targets (squares) and CGS targets (triangles). The trend lines serve only as guide for the eye.*

The SEM images in Figure 3 present the fracture cross-sections and top view images for two NbO_x films deposited at the respective highest oxygen partial pressures of $p(O_2) = 48.2\%$ (Figs. 3 (a) and (b)) and $p(O_2) = 63.1\%$ (Figs. 3 (c) and (d)) for the two different target variants. The fracture cross-sections do not significantly differ for both films, except the different film thickness. In both cases, the films are characterized by a dense and amorphous appearance, which corresponds to findings reported in literature for sputter deposited Nb_2O_5 films [17,18]. The film grown from the SI targets shows a slightly rough surface in the top view image indicating a domed growth morphology, which can be associated with the Volmer-Weber type thin film growth mode [2,19]. In comparison, the film deposited from the CGS targets show a finer and less pronounced

surface. This difference might originate from both, the more intense particle bombardment of the film surface with energetic film forming species as a result of the higher target voltage and the higher oxygen partial pressure, where the additional oxygen can act as a grain refiner [20].

For comparison of the films deposited, their chemical composition was measured by EDX. For both target variants, slight increases of the oxygen content within the film with increasing oxygen partial pressure have been observed. The oxygen content of the films deposited from the SI targets varies between 60.3 and 62.7 at.%, while those films synthesized using the CGS targets contain between 61.4 and 63.0 at.% oxygen. Thus, despite the limited resolution of EDX for light elements [21] and the higher oxygen partial pressures applied for the CGS targets (see Table 1), films with similar compositions have been synthesized for both target variants.

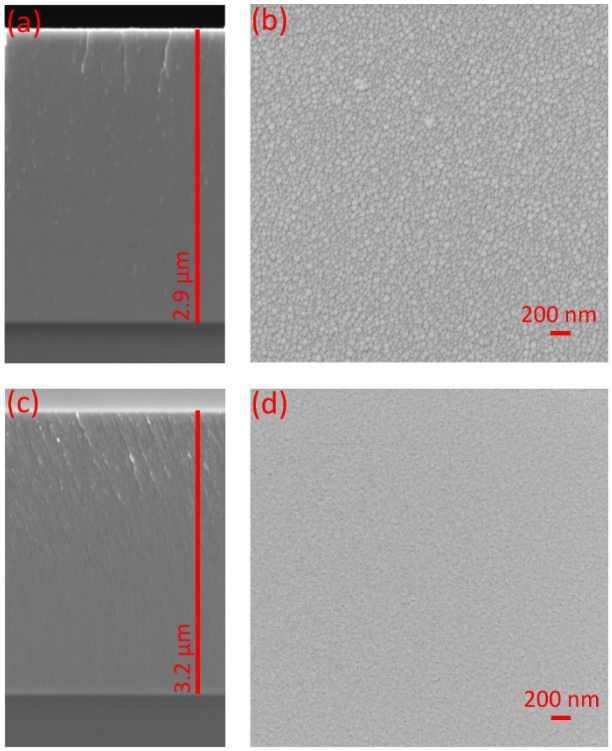

Figure 3: *SEM fracture cross-section and top view images of NbO_x films deposited from (a),(b) SI targets at $p(O_2)$ = 48.2% and (c),(d) CGS targets at $p(O_2)$ = 63.1% on Si substrates.*

Figure 4 summarizes the XPS spectra for selected films, evaluating the Nb3d, consisting of the characteristic $Nb3d_{5/2}$-$Nb3d_{3/2}$ doublet, and O1s core level spectra for the three applied detection angles of 0°, 35° and 50° to the surface normal. The different detection angles yielding different probing depths enable to investigate the binding state of possible surface layers [22]. The curve fitting of the Nb3d orbital (Figs. 4 (a)-(c)) for the three films selected shows the highest peak intensity at a binding energy of ~207 eV, which can be assigned to the Nb^{5+} oxidation state. This peak position is in good agreement with the binding energy of Nb_2O_5 [22-25]. For the two films deposited at the respective lowest oxygen partial pressure (Figs. 4 (a) and (b)), an additional small peak at a binding energy of ~206 eV can be observed, pointing towards the presence of the Nb^{4+} oxidation state characteristic for NbO_2 [22,23]. This peak does not occur for the films deposited at the highest oxygen partial pressure (see Figure 4 (c) for a representative film grown from the SI targets). Consequently, it is assumed that the latter film is dominated by Nb_2O_5 bonds, while for those films presented in Figs. 4 (a) and (b) additional fractions of NbO_2 bonds are formed.

With the increasing detection angle and the thus reduced probing depth, the peak height for the Nb^{4+} binding energy decreases. This decrease points towards the formation of a few nm thick Nb_2O_5 top layer, most probably during storage in ambient air. Under atmospheric conditions, Nb_2O_5 is considered as the thermodynamically most stable NbO_x phase [22,23]. To estimate the fraction of Nb^{4+} bonds, model calculations of the Nb3d spectra for reproducing the measured data have been performed by applying and adjusting two different fitting parameters. First, the presence of a Nb_2O_5 top layer with variable layer thickness and second, the ratio of Nb^{4+}/Nb^{5+} in the underlying film. The model calculation for different detection angles is described in detail in the supplementary information. The calculation yields a Nb^{4+}/Nb^{5+} ratio of 0.29 for the film deposited from the SI targets at $p(O_2)$ = 40.8% and of 0.21 for the film deposited from the CGS targets at $p(O_2)$ = 54.7%. The higher Nb^{4+} content can most probably be explained by the lower fraction of oxygen available during sputtering.

The XPS spectra of the O1s core level are displayed in Figs. 4 (d) to (f) for the same three film variants and detection angles. These spectra consist of three peaks with the highest intensity for O^{2-} at a binding energy of 530.1 eV, which ca be attributed to an oxidic bond

with Nb. However, a distinction between Nb_2O_5 and NbO_2 is not possible. The other components indicate surface hydroxylation with OH-groups and adsorbed H_2O-molecules at ~531 eV and ~532 eV [26].

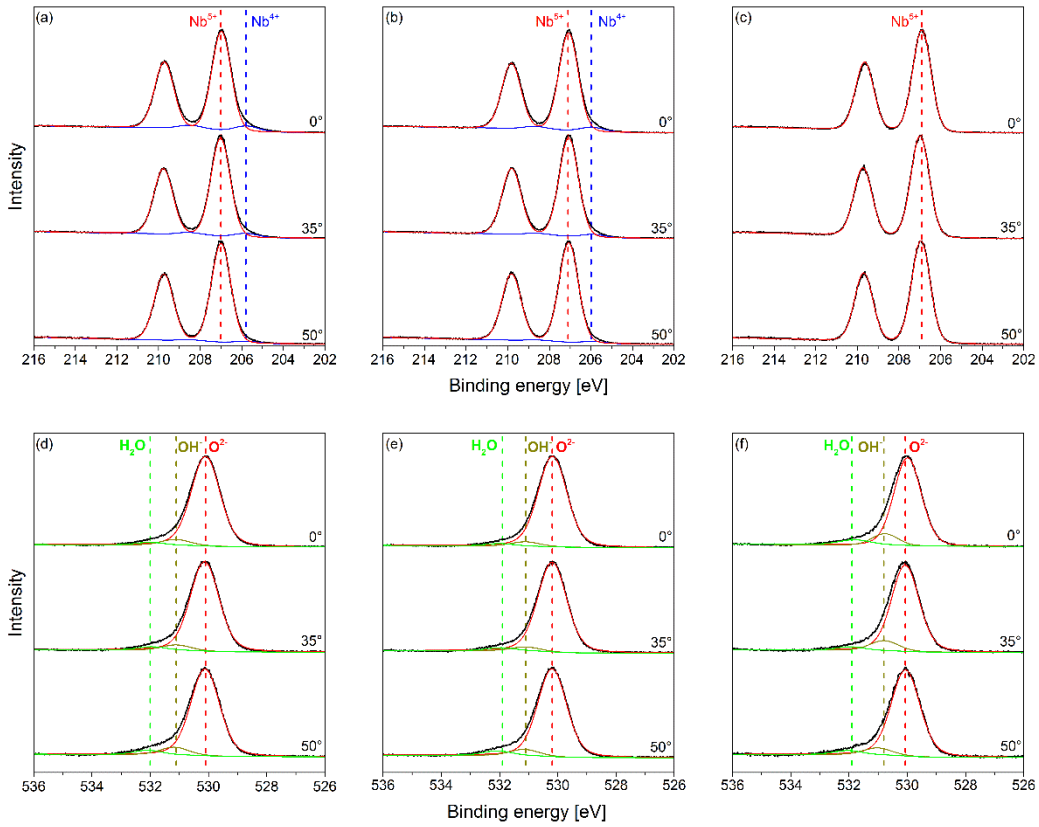

Figure 4: *Nb3d and O1s XPS spectra of NbO_x films deposited from SI and CGS targets for various oxygen partial pressures and detection angles to the surface normal. (a),(d) SI targets at $p(O_2)$ = 40.8%; (b),(e) CGS targets at $p(O_2)$ = 54.7%; (c),(f) SI targets at $p(O_2)$ = 48.2%.*

Selected X-ray diffractograms are summarized in Figure 5 for both target variants and different oxygen partial pressures. The absence of well-defined peaks of crystalline phases corroborates the assumption of an amorphous film microstructure, as already inferred from the SEM cross-sections shown in Figure 3. Also the enhanced intensity between 20° < 2Θ < 40° cannot be associated with a crystalline oxide phase like NbO_2 or Nb_2O_5. Differences between the SI and CGS targets can not be recognized.

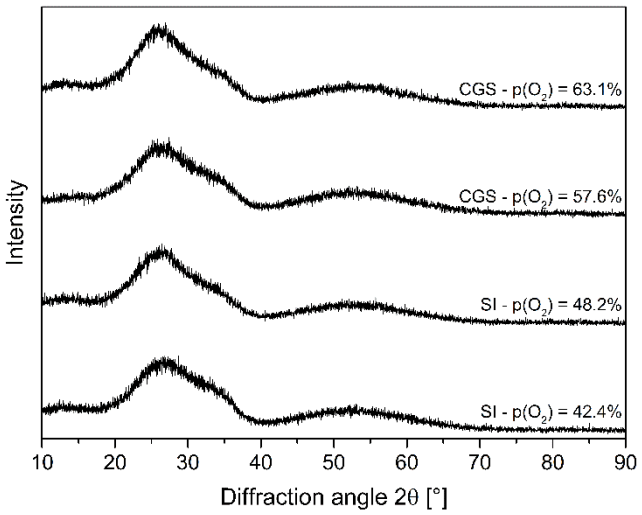

Figure 5: *X-ray diffractograms of NbO_x films grown by sputter deposition from SI and CGS targets on Si substrates at various oxygen partial pressures.*

Figure 6 demonstrates that the NbO_x films undergo an optical shift from dark and non-transparent to nearly fully transparent with increasing oxygen partial pressure. Figures 7 (a) and (b) summarize the transmittance and reflectance spectra for films deposited at different oxygen partial pressures for both target variants. The transparent films grown at the higher oxygen partial pressure settings ($p(O_2) \geq 46.0\%$ for the SI and $p(O_2) \geq 60.4\%$ for the CGS targets) reach a maximum transmittance of ~80%, while the reflectance stays approximately constant between 20-30%, regardless of the partial pressure. Both are in good agreement with literature [27–29]. The development of transmittance and reflectance as a function of the oxygen partial pressure at an averaged wavelength between 540-560 nm can be seen in Figure 7 (c). This wavelength was chosen, since the luminous efficiency function of the human eye for daylight shows its maximum at ~550 nm [30]. Again, the clear shift in transparency with increasing oxygen partial pressure can be seen.

The form of a transmission spectrum, like the appearance of interference fringes (see Figure 7 (a)), is directly determined by the refractive index n together with the film thickness d. The product of n and d influences the spacing of the interference fringes. Based on these fringes, Poelman et al. [31] suggested a paper and pencil method to calculate the refractive index from the transmission maxima, as displayed in Figure 7 (d) for the films deposited at the respective highest oxygen partial pressure applied to the

SI and the CGS targets. In the wavelength range between 500-850 nm n has a value of ~2.5, which again shows a good agreement with literature. There, n is reported to lie between 2.1 and 2.6 for amorphous Nb_2O_5 films, depending on synthesis method, microstructure and internal stresses [17,18,23,29,32]. The sharp increase for the wavelength below 500 nm may indicate the limit for the paper and pencil method, but can also be related to the 2 nm intervals applied for the measurements, leading to a reduced accuracy of the transmission maxima positions.

Summarizing the optical properties of the NbO_x films and comparing the two different target variants, hardly any differences are visible. Both the transmittance and reflectance properties show a strong similarity, together with the shape of the shift from non-transparent to nearly fully-transparent films as well as the development of the refractive index. Considering the optical properties of the films grown at the lowest and highest oxygen partial pressure, the difference can be explained by the diverse bonding characteristics, as suspected by XPS. The presence of Nb^{4+}, and thus the non-transparent NbO_2 phase, affects the optical transmittance of the films significantly. Highly transparent single-phase Nb_2O_5 films can be grown at $p(O_2) \geq 46.0\%$ (SI targets) and 60.4% (CGS targets). For the latter process, Figure 2 shows a 43% higher film growth rate compared to conventional SI targets could be obtained.

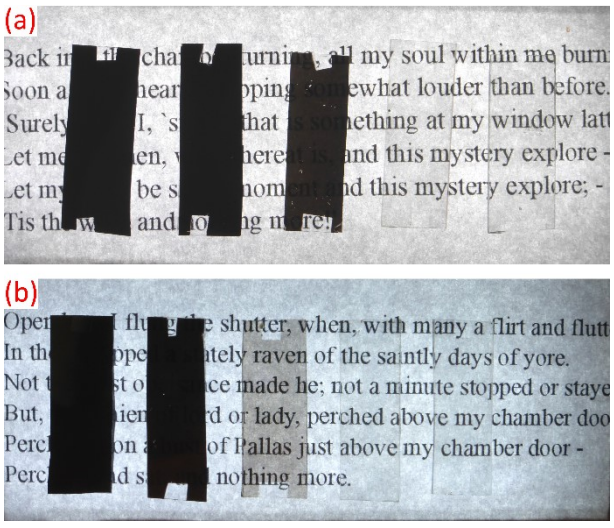

Figure 6: *NbO_x films deposited on SLG substrates with oxygen partial pressure increasing from left to right. (a) SI targets ($p(O_2)$ = 40.8, 42.4, 44.6, 46.0 and 48.2%, respectively); (b) CGS targets ($p(O_2)$ = 54.7, 57.6, 58.6, 60.4 and 63.1%, respectively).*

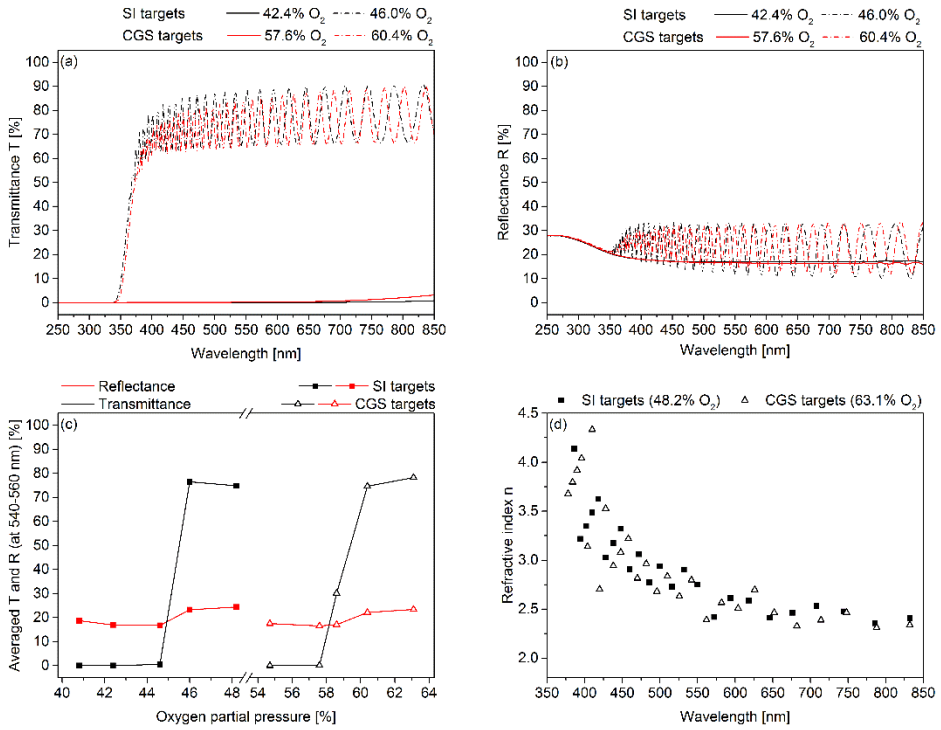

Figure 7: *Optical properties of NbO_x films grown on Corning EAGLE XG glass sheets. (a) Transmittance T and (b) reflectance R as a function of the wavelength, (c) averaged transmittance T and reflectance R as a function of the oxygen partial pressure between 540-560 nm, (d) refractive index n as a function of the wavelength.*

4. Conclusions

Within this work, the sputter behaviour of cold gas sprayed Nb targets in argon/oxygen atmosphere with increasing oxygen partial pressure has been investigated and compared to that of conventionally sintered Nb targets. Besides the higher target discharge voltage and consequently a by 43% higher film growth rate obtained for the cold gas sprayed targets due to their different design, no remarkable differences for the films grown from both target variants was observed. The amorphous NbO_x films show an optical shift from dark and non-transparent towards transparent properties with increasing oxygen partial pressure, with a maximum transparency of ~80% and a refractive index n of ~2.5. This optical shift can most likely be explained by the presence of the Nb^{4+} oxidation state and thus the NbO_2 phase beside Nb_2O_5 in the films deposited at lower oxygen partial pressures. In summary, it could be shown that using the novel cold gas sprayed Nb targets results in the formation of films with properties equivalent to conventionally sintered targets.

5. Acknowledgments

This work was supported by the Österreichische Forschungsförderungsgesellschaft FFG within the project "E²CGS" (project number: 150130). The authors are grateful to Michaela Zaberning (Plansee SE, Reutte, Austria) for SEM characterization.

6. References

[1] D.M. Mattox, Handbook of physical vapor deposition (PVD) processing, 2nd ed., William Andrew, Oxford, UK, 2010.

[2] K. Wasa, I. Kanno, H. Kotera, Handbook of sputter deposition technology: Fundamentals and applications for functional thin films, nano-materials and MEMS, 2nd ed., Elsevier/Andrew, Amsterdam, 2012.

[3] N. Schalk, T. Weirather, C. Polzer, P. Polcik, C. Mitterer, A comparative study on $Ti_{1-x}Al_xN$ coatings reactively sputtered from compound and from mosaic targets, Surf. Coat. Tech. 205 (2011) 4705–4710.

[4] C.-F. Lo, P. McDonald, D. Draper, P. Gilman, Influence of tungsten sputtering target density on physical vapor deposition thin film properties, Journal of Elec. Materi. 34 (2005) 1468–1473.

[5] B.L. Gehman, S. Jonsson, T. Rudolph, M. Scherer, M. Weigert, R. Werner, Influence of manufacturing process of indium tin oxide sputtering targets on sputtering behavior, Thin Solid Films 220 (1992) 333–336.

[6] S. Grigoriev, A. Okunkova, A. Sova, P. Bertrand, I. Smurov, Cold spraying: From process fundamentals towards advanced applications, Surf. Coat. Tech. 268 (2015) 77–84.

[7] T. Schmidt, H. Assadi, F. Gärtner, H. Richter, T. Stoltenhoff, H. Kreye, T. Klassen, From particle acceleration to impact and bonding in cold spraying, J. Therm. Spray. Techn. 18 (2009) 794–808.

[8] T. Schmidt, F. Gärtner, H. Assadi, H. Kreye, Development of a generalized parameter window for cold spray deposition, Acta Mater. 54 (2006) 729–742.

[9] T.H. van Steenkiste, J.R. Smith, R.E. Teets, J.J. Moleski, D.W. Gorkiewicz, R.P. Tison, D.R. Marantz, K.A. Kowalsky, W.L. Riggs, P.H. Zajchowski, B. Pilsner, R.C. McCune, K.J. Barnett, Kinetic spray coatings, Surf. Coat. Tech. 111 (1999) 62–71.

[10] N. Fateh, G.A. Fontalvo, C. Mitterer, Structural and mechanical properties of dc and pulsed dc reactive magnetron sputtered V_2O_5 films, J. Phys. D: Appl. Phys. 40 (2007) 7716–7719.

[11] C. Mitterer, N. Fateh, F. Munnik, Microstructure-property relations of reactively magnetron sputtered VC_xN_y films, Surf. Coat. Tech. 205 (2011) 3805–3809.

[12] F. Ullmann, J. Eckert, Ullmann's Encyclopedia of Industrial Chemistry: Niobium and Niobium Compounds, Wiley-VCH Verlag GmbH & Co. KGaA, Weinheim, 2005.

[13] S. Kumar, A. Jyothirmayi, N. Wasekar, S.V. Joshi, Influence of annealing on mechanical and electrochemical properties of cold sprayed niobium coatings, Surf. Coat. Tech. 296 (2016) 124–135.

[14] W.D. Sproul, D.J. Christie, D.C. Carter, Control of reactive sputtering processes, Thin Solid Films 491 (2005) 1–17.

[15] F. Ullmann, H. Sibum, V. Güther, O. Roidl, F. Habashi, H.U. Wolf, Ullmann's Encyclopedia of Industrial Chemistry: Titanium, Titanium Alloys, and Titanium Compounds, Wiley-VCH Verlag GmbH & Co. KGaA, Weinheim, 2005.

[16] T. Stoltenhoff, C. Borchers, F. Gärtner, H. Kreye, Microstructures and key properties of cold-sprayed and thermally sprayed copper coatings, Surf. Coat. Tech. 200 (2006) 4947–4960.

[17] F. Lai, M. Li, H. Wang, H. Hu, X. Wang, J.G. Hou, Y. Song, Y. Jiang, Optical scattering characteristic of annealed niobium oxide films, Thin Solid Films 488 (2005) 314–320.

[18] G. Ramírez, S.E. Rodil, S. Muhl, D. Turcio-Ortega, J.J. Olaya, M. Rivera, E. Camps, L. Escobar-Alarcón, Amorphous niobium oxide thin films, J. Non-Cryst. Solids. 356 (2010) 2714–2721.

[19] P.M. Martin, Handbook of Deposition Technologies for Films and Coatings: Science, Applications and Technology, 3rd ed., Elsevier, Amsterdam, 2010.

[20] I. Petrov, P.B. Barna, L. Hultman, J.E. Greene, Microstructural evolution during film growth, J. Vac. Sci. Technol. A 21 (2003) S117-S128.

[21] L. Reimer, Scanning Electron Microscopy: Physics of Image Formation and Microanalysis, Springer Berlin Heidelberg, Berlin, Heidelberg, s.l., 1998.

[22] Q. Ma, R.A. Rosenberg, Angle-resolved X-ray photoelectron spectroscopy study of the oxides on Nb surfaces for superconducting r.f. cavity applications, Appl. Surf. Sci. 206 (2003) 209–217.

[23] C. Nico, T. Monteiro, M.P.F. Graça, Niobium oxides and niobates physical properties: Review and prospects, Prog. Mater. Sci. 80 (2016) 1–37.

[24] T. Hryniewicz, K. Rokosz, H.Z. Sandim, SEM/EDX and XPS studies of niobium after electropolishing, Appl. Surf. Sci. 263 (2012) 357–361.

[25] B. Vincent Crist, PDF Handbooks of Monochromatic XPS Spectra (Demo Version): Volume 1 - The Elements and Native Oxides, XPS International, LLC, Mountain View, California, USA.

[26] Y. Tanaka, M. Nakai, T. Akahori, M. Niinomi, Y. Tsutsumi, H. Doi, T. Hanawa, Characterization of air-formed surface oxide film on Ti-29Nb-13Ta-4.6Zr alloy surface using XPS and AES, Corrosion Science 50 (2008) 2111–2116.

[27] A. Foroughi-Abari, K.C. Cadien, Growth, structure and properties of sputtered niobium oxide thin films, Thin Solid Films 519 (2011) 3068–3073.

[28] R. Franz, C. Clavero, J. Kolbeck, A. Anders, Influence of ionisation zone motion in high power impulse magnetron sputtering on angular ion flux and NbO_x film growth, Plasma Sources Sci. T. 25 (2016).

[29] S. Venkataraj, R. Drese, O. Kappertz, R. Jayavel, M. Wuttig, Characterization of niobium oxide films prepared by reactive dc magnetron sputtering, Phys. Status Solidi A 188 (2001) 1047–1058.

[30] L.T. Sharpe, A. Stockman, W. Jagla, H. Jagle, A luminous efficiency function, V*(λ), for daylight adaptation, J. Vision. 5 (2005) 948–968.

[31] D. Poelman, P.F. Smet, Methods for the determination of the optical constants of thin films from single transmission measurements: a critical review, J. Phys. D: Appl. Phys. 36 (2003) 1850–1857.

[32] F. Lai, L. Lin, Z. Huang, R. Gai, Y. Qu, Effect of thickness on the structure, morphology and optical properties of sputter deposited Nb_2O_5 films, Appl. Surf. Sci. 253 (2006) 1801–1805.

Publication V

Effect of the bias pulse frequency on reactively sputter deposited NbO_x films

Roland Lorenz, Michael O'Sullivan, Alexander Fian, Dietmar Sprenger, Bernhard Lang, Christian Mitterer

Submitted for publication

Effect of the bias pulse frequency on reactively sputter deposited NbO_x films

Roland Lorenz[1*], Michael O'Sullivan[2], Alexander Fian[3], Dietmar Sprenger[2], Bernhard Lang[2], Christian Mitterer[1]

[1] Department of Physical Metallurgy and Materials Testing, Montanuniversität Leoben, Franz-Josef-Straße 18, 8700 Leoben, Austria

[2] Plansee SE, Metallwerk-Plansee-Straße 71, 6600 Reutte Austria

[3] Institute for Surface Technologies and Photonics, Joanneum Research Forschungsgesellschaft mbH, Franz-Pichler-Straße 30, 8160 Weiz, Austria

Abstract

Within the current work, niobium oxide thin films have been deposited by reactive d.c. magnetron sputtering from cold gas sprayed niobium targets, applying a systematic variation of oxygen partial pressure, bias pulse frequency and substrate temperature. The films grown without additional substrate heating are amorphous. X-ray photoelectron spectroscopy shows the Nb^{5+} oxidation state, characteristic for the Nb_2O_5 phase, for films grown at the highest oxygen partial pressure applied, while the Nb^{4+} state of NbO_2 is additionally present at lower oxygen partial pressures. With increasing oxygen partial pressure, an optical shift from non-transparent to nearly fully transparent was observed, whereby the higher bias pulse frequency leads to a transition already at lower oxygen partial pressures. The transparent films are characterised by a maximal transparency of ~80% and a refractive index of ~2.5. Increasing the substrate temperature of up to 600°C results in the formation of well crystalline coatings consisting of the orthorhombic Nb_2O_5 phase, which are whitish and semi-transparent.

Keywords: Niobium oxides, reactive magnetron sputtering, cold gas spraying, thin films, pulsed bias

[*] Corresponding author: Mail: roland.lorenz@stud.unileoben.ac.at

1. Introduction

Thin films based on niobium oxide find a wide variety of technical applications due to their versatile properties; they are used e.g. as capacitor materials [1,2] or as catalysts for polymerization processes [1,3]. Niobium pentoxide (Nb_2O_5), especially as a polycrystalline film, is well known for its promising electrochromic behaviour with a wide optical modulation range [2–4]. Amorphous Nb_2O_5, a transparent dielectric material, possesses a high refractive index which makes it useful in optical systems such as optical interference filters [1,2,5,6]. Besides Nb_2O_5, which is the thermodynamically most stable phase in the niobium-oxygen system [7], niobium oxides can also occur as monoxide NbO, a metallic compound with superconductive properties below 1.38 K [1,7], or niobium dioxide NbO_2, a semiconducting material [1,3,7]. Previous investigations performed with reactive d.c. magnetron sputter deposition, carried out under various oxygen partial pressure and total pressure conditions, showed that amorphous Nb_2O_5 is the most probable phase to be formed [2,3,5,6]. The oxygen content provided determines if – in addition to these Nb_2O_5 films – films consisting of NbO or NbO_2 phases can also be deposited [1]. Also, high-power impulse magnetron sputtering has been applied for the deposition of niobium oxides [8], where, compared to d.c. magnetron sputtering, the inherently high degree of ionisation promotes growth of stoichiometric and dense films. Crystallization of Nb_2O_5 films has been observed for thicknesses exceeding ~2 µm [6] or by post-deposition annealing treatment in air [3,5].

Despite the reports mentioned, detailed studies on the influence of substrate temperature or substrate bias induced ion bombardment on microstructure and properties of NbO_x films are not available. The aim of this study is thus to synthesize NbO_x thin films by reactive magnetron sputtering with a variation of the oxygen partial pressure, substrate bias pulse frequency and substrate temperature and to determine their influence on microstructure evolution and optical properties.

2. Experimental details

For the deposition of the NbO_x films, two Nb targets (ø 50.8 × 6 mm²) prepared by cold gas spraying (CGS) were used. In CGS, a metallic powder is accelerated in a high

pressurized nitrogen gas jet by a de Laval type nozzle. The powder particles are not molten or thermally softened prior to their impact onto the substrate, leading to a low oxygen content within the sprayed coating [9–11]. Within this work, Nb powder was deposited by CGS as a 2 mm thick coating onto 4 mm thick titanium backing plates, and the sprayed coatings served as sputter targets.

These targets were mounted to magnetrons focused towards the substrate holder in a laboratory-scale unbalanced d.c. magnetron sputter deposition system. The films were grown on 21 × 7 × 1 mm³ soda-lime glass (SLG), (100) oriented 21 × 7 × 0.5 mm³ Si substrates and 50 × 50 × 1 mm³ display glass sheets (Corning EAGLE XG), which were ultrasonically cleaned in acetone and ethanol and dried in hot air prior to deposition. The substrate rotation was set at 50 rpm and the vacuum base pressure was kept below 2×10^{-3} Pa. To remove possible contaminations, the substrates were plasma etched in pure argon atmosphere before film deposition, using a pulsed d.c. discharge at -500 V and 50 kHz for 10 min. A constant d.c. current of 0.35 A per magnetron was applied to the targets for a deposition time of 60 min. The NbO_x films were grown in a reactive argon/oxygen atmosphere at a constant chamber pressure of p_{tot} = 0.5 Pa. To investigate the influence of an increasing oxygen content, the oxygen partial pressure, calculated from gas flow calibration curves, was varied between $p(O_2)$ = 54.7% and 63.1% (see Table 1). An asymmetrically pulsed d.c. bias of -50 V was applied to the substrate holder with frequencies of 50 and 250 kHz, leading to negative pulse duration times of 19.5 and 3.5 µs, respectively. In both cases, the positive pulse, pre-set from the ENI RPG 50 power supply used at a voltage of +37 V, had a duration of 0.5 µs. To obtain information on the substrate temperature for the deposition runs without additional substrate heating, temperature-time profiles were recorded with a type K thermocouple, mounted in front of the substrate holder. For the films deposited at an oxygen partial pressure of $p(O_2)$ = 57.6% and a bias frequency of 250 kHz, the substrate temperature was varied by additional substrate heating between 300 and 600 °C.

The morphology of the deposited films was investigated using surface and fracture cross-section micrographs obtained by scanning electron microscopy (SEM, Carl Zeiss NTS Ultra plus). To determine the chemical composition, samples grown at a bias pulse frequency of 250 kHz were analysed by elastic recoil detection analysis (ERDA) using a 43 MeV $^{35}Cl^{7+}$ ion beam. The angle between the sample normal and the incoming beam

was 75°, the scattering angle was 31°. For an analysed area of 1.5 × 1.5 mm², the recoiling sample ions were detected using a Bragg ionization chamber, enabling energy measurements and atomic number identification of the recoils. Hydrogen recoils were detected using a separate solid state detector at a scattering angle of 41°. X-ray photoelectron spectroscopy (XPS) for selected samples was performed to identify the binding energies and oxidation states of the Nb and O atoms using an Omicron Multiprobe surface analysis system with a DAR 400 X-ray source with an Al-Kα beam and an excitation energy of 1486.7 eV, an XM 500 quartz crystal monochromator and an EA 125 hemispherical electron energy analyser with a 5 channel pulse counting channeltron at a pass energy of 20 eV. The total energy solution of the system (excitation source, analyser) was 0.5 eV. The binding energy was corrected by using the C-C bond of the C1s peak of residual hydrocarbon surface contaminants at 284.6 eV as reference. All measurements were performed in the as-received state under three different detection angles of 0, 35 and 50° to the surface normal and the fitting of the spectral line shape was performed by convolution of Gaussian and Lorentzian functions. X-ray diffraction (XRD) measurements were done using a Bruker-AXS D8 Advance diffractometer in grazing incidence geometry with an angle of incidence of 5° and Cu-Kα radiation (λ = 1.5406 Å). Identification of the oxide phases was further supported by Raman spectroscopy using a Jobin Yvon LABRAM confocal Raman spectrometer equipped with a frequency doubled Nd-YAG laser (λ = 532.2 nm) and a measurement range between 200-1200 nm. To investigate the optical properties of the films, the reflection and transmission spectres were recorded between 250-850 nm at 2 nm intervals using a PerkinElmer-LAMBDA 950 UV/Vis/NIR spectrometer with W- and V-set up, respectively.

Table 1: *Variations of the Ar and O_2 gas flow with the resulting O_2 partial pressure.*

Ar flow [sccm]	28	27	27	26	25
O_2 flow [sccm]	12	13	13.5	14	15
$p(O_2)/p_{tot}$ [%]	54.7	57.6	58.6	60.4	63.1

3. Results

Figure 1 (a) shows the film growth rate and the applied target voltage as a function of the increasing oxygen partial pressure for films grown without additional substrate heating at both bias pulse frequency settings. In addition, the temperature-time curve is displayed in Figure 1 (b), indicating values of 198°C (50 kHz) and 206°C (250 kHz) after the applied deposition time of 60 min. In both frequency settings, the target voltage rises continuously with increasing oxygen partial pressure. For the 50 kHz deposition, values increase from -565 to -600 V (i.e. by ~6%), while the minimum and maximum voltage for the 250 kHz deposition lies between -536 and -589 V, corresponding to an increase of ~9%. In a similar way as the voltage increases, the film growth rates drops with the increasing oxygen partial pressure. Here, the values vary between ~83 nm/min for $p(O_2)$ = 54.7 % and 53 nm/min (50 kHz) and 48 nm/min (250 kHz), respectively, for $p(O_2)$ = 63.1%. Additionally it is evident that for all oxygen partial pressures the lower bias pulse frequency of 50 kHz results in higher voltage and growth rate values. For the films grown at $p(O_2)$ = 57.6% and 250 kHz at substrate temperatures up to 600°C, the film growth rate slightly declines to a minimum value of 68 nm/min at 600°C, compared to 73 nm/min for the film grown without additional substrate heating. The target voltage stays approximately constant at -550 V over the whole temperature range investigated.

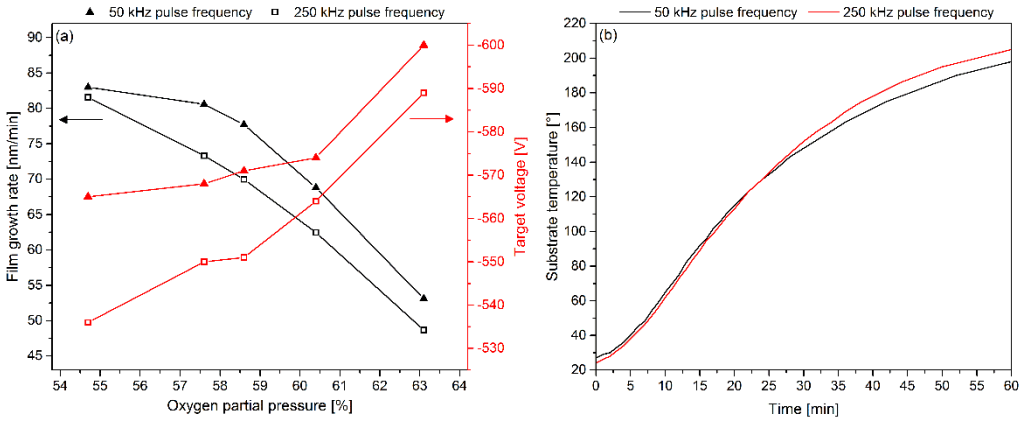

Figure 1: *(a) Growth rate and target voltage as a function of the oxygen partial pressure and (b) the substrate temperature-time curve for the two bias pulse frequency settings studied, recorded in 1 min steps (0-20 min) or 2 min steps (20-60 min), respectively.*

The fracture cross-sections and top view SEM micrographs of four films deposited at the respective lowest ($p(O_2)$ = 54.7%) and highest oxygen partial pressure ($p(O_2)$ = 63.1%) for both bias pulse frequency settings are displayed in Figures 2 (a) to (d). All films are characterized by a dense and feature-less microstructure, where the decreasing film thickness with increasing oxygen partial pressure as a result of the decreasing growth rate (see Figure 1 (a)) can clearly be recognized in the fracture cross-sections. The irregularities visible in the upper range of the films are attributed to fracture lines. The rising oxygen partial pressure hardly affects the film surface topography; all films grown without additional substrate heating appear smooth and homogenous. While some minor surface features are recognizable for the 50 kHz samples, the 250 kHz variants seem to be even smoother. The morphology and topography of the films deposited did not change significantly for substrate temperatures up to 500°C. The film grown at $p(O_2)$ = 57.6%, a bias pulse frequency of 250 kHz and a substrate temperature of 600°C is displayed in Figure 2 (e), showing a change from a featureless to a columnar grain structure. A closer look indicates that in the lower third the film resembles the feature-less morphology of those films grown without additional substrate heating, while crystal growth is dominating in the later growth stage. In good agreement, the film topography appears rough with faceted crystals protruding from the surface.

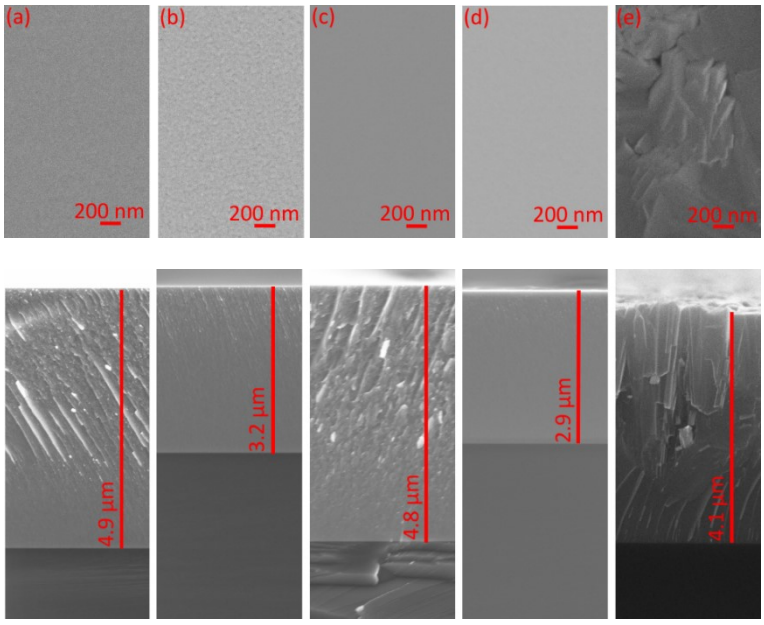

Figure 2: *SEM top view (above) and fracture cross-section (below) micrographs of NbO_x films deposited at various oxygen partial pressures and bias pulse settings on Si substrates. (a) $p(O_2)$ = 54.7%, 50 kHz; (b) $p(O_2)$ = 63.1%, 50 kHz; (c) $p(O_2)$ = 54.7%, 250 kHz; (d) $p(O_2)$ = 63.1%, 250 kHz; (e) $p(O_2)$ = 57.6%, 250 kHz, T = 600°C.*

The chemical composition of the films grown at 250 kHz without additional substrate heating and at a substrate temperature of 600°C, measured by ERDA, is summarized in Table 2. Beside Nb and O only a minor content of hydrogen could be detected. Within the range investigated, the increasing oxygen partial pressure does not affect the Nb and O content within the films. The O/Nb atomic ratio of ~2.35 is located between NbO_2 (O/Nb = 2) and Nb_2O_5 (O/Nb = 2.5). The minor hydrogen contamination is attributed to hydrogen uptake during deposition stemming from H_2O contamination of the residual gas. H_2O is known as the main hydrogen source, present in high vacuum systems [12].

Table 2: *Element concentrations determined for the NbO_x films deposited at a bias pulse frequency of 250 kHz by ERDA.*

$p(O_2)$ [%]	Substrate-temperature [°C]	Nb [at.%]	O [at.%]	H [at.%]
54.7	RT	29.7	70.2	0.09
57.6	RT	29.7	70.1	0.19
58.6	RT	29.7	70.1	0.21
60.4	RT	29.7	70.0	0.26
63.1	RT	29.7	70.0	0.24
57.6	600	30.0	69.6	0.44

In Figure 3, the XPS spectra for selected films are summarized, evaluating the Nb3d and O1s core level spectra in the as-received state, measured under three different detection angles of 0, 35 and 50° to the surface normal. As a result of the characteristic $Nb3d_{5/2}$-$Nb3d_{3/2}$ doublet, two different components in the XPS spectra of Nb can be identified which can be assigned to different bond states of Nb. For all three films investigated, the curve fitting of Nb3d shows the most prominent feature at a binding energy of ~207.1 eV (Figures 3 (a) to (c)), which can be related to the Nb^{5+} oxidation state, and thus the binding energy of Nb_2O_5 [7,13–15]. Further, a low intensity peak can be seen at a binding energy of ~206.0 eV for the two films grown at the respective lowest oxygen partial pressure. This peak is associated with the Nb^{4+} oxidation state and thus the binding energy of NbO_2 [7,14]. By increasing the detection angle from 0 to 50°, the peak height of the Nb^{4+} peak decreases indicating a surface oxidation layer of Nb^{5+}. For the 250 kHz film at 50° it is no longer detected (see Figure 3 (b)). For the films deposited at the highest oxygen partial pressure there is no evidence of the peak corresponding to Nb^{4+} at any detection angle.

The XPS spectra of the O1s core level are displayed in Figures 3 (d) to (f) for the same three films and detection angles, and they consist of three peaks. The highest intensity peak characteristic for O^{2-} in metal oxides can be found at a binding energy of 530.1 eV, beside the two peaks stemming from surface hydroxylation with OH-groups and absorbed H_2O molecules at binding energies of ~531 eV and ~532 eV, respectively [16]. Again, the increase of the peak height with increasing detection angle indicates that

these contributions come from the film surface. Except for the varying peak heights of these two surface contaminants, no further significant differences can be seen for the three NbO_x films investigated.

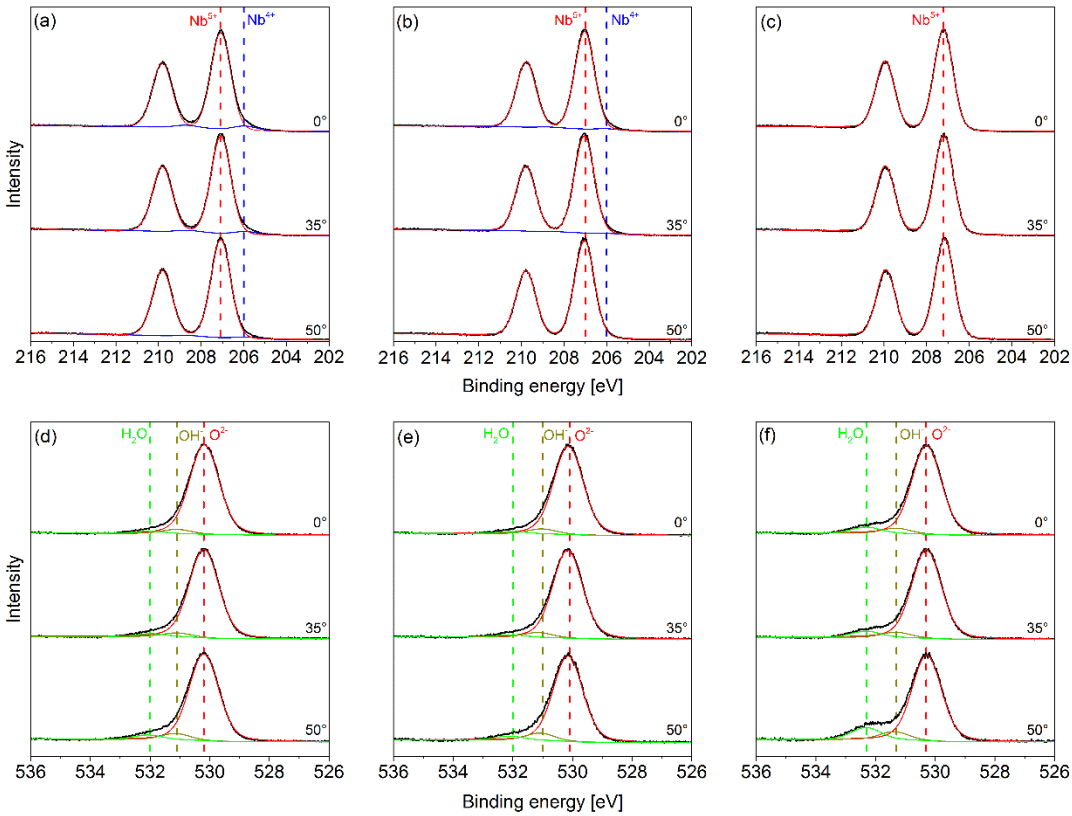

Figure 3: *Nb3d and O1s XPS spectra of NbO_x films deposited with different bias pulse frequencies and oxygen partial pressures, measured under different detection angles to the surface normal. (a), (d) 50 kHz and $p(O_2)$ = 54.7%; (b),(e) 250 kHz and $p(O_2)$ = 54.7%; (c),(f) 250 kHz and $p(O_2)$ = 63.1%.*

Figure 4 presents the X-ray diffractograms of NbO_x films deposited with a bias pulse frequency of 250 kHz; they do not differ significantly from those of the films grown at 50 kHz (not shown). In particular, films deposited at three different oxygen partial pressures are displayed, in addition to those two films grown at substrate temperatures of 500 and 600°C at $p(O_2)$ = 57.6%. The absence of well-defined peaks obtained for those films grown without additional substrate heating supports the optical impression derived from the fracture cross-section micrographs in Figure 2 and confirms the amorphous film microstructure. The slightly enhanced intensity between 20° < 2Θ < 40° is not associated with a crystalline oxide phase like NbO_2 or Nb_2O_5. Film growth at an

elevated temperature up to 500°C does not lead to significant changes in the amorphous microstructure, although first indications for enhanced diffraction intensity seem to appear at 500°C, as indicated by the arrow in Figure 4. In contrast, a further increase of the substrate temperature to 600°C results in sharp and high-intensity diffraction peaks, which best agree with the orthorhombic T-Nb_2O_5 phase [17].

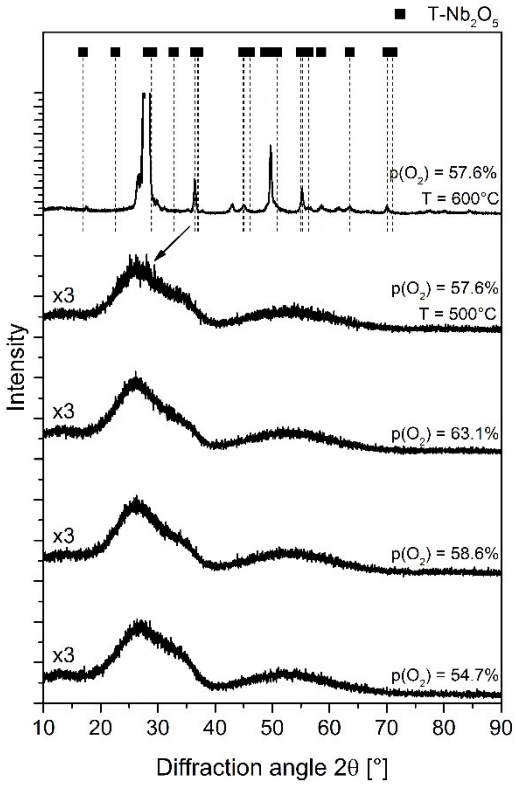

***Figure 4**: X-ray diffractograms of NbO_x films deposited at a bias pulse frequency of 250 kHz for various oxygen partial pressures and substrate temperatures on Si substrates. The black squares indicate the diffraction peaks of T-Nb_2O_5 [17].*

The recorded Raman spectra for films deposited with the bias pulse frequency of 250 kHz are displayed in Figure 5. NbO_2 and Nb_2O_5 are known to be Raman active and peak positions taken from refs. [7,18–20] for both phases have been added. Only at oxygen partial pressures $p(O_2) \geq 58.6\%$, broad bands with low intensity are visible, particularly between 200-350 cm^{-1} and 550-750 cm^{-1}. These broad peaks prevent an unambiguous assignment to a particular niobium oxide phase. At lower partial pressures, the films do not appear to be Raman active. The high intensity peaks at 520 cm^{-1} and between 920-1045 cm^{-1} are attributed to the Si substrates, as the NbO_x films become transparent at $p(O_2) \geq 58.6\%$ [21].

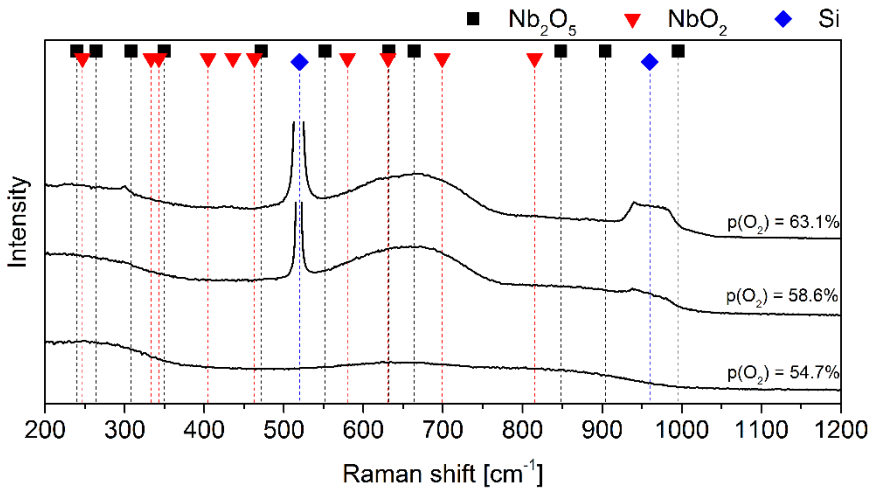

Figure 5: *Raman spectra of NbO_x films deposited with a bias pulse frequency of 250 kHz for varying oxygen partial pressure on Si substrates. Reference spectra for Nb_2O_5, NbO_2 and Si taken from references [7,18–21] are included.*

As demonstrated in Figure 6 (a), the NbO_x films undergo an optical shift from non-transparent to nearly fully transparent with increasing oxygen partial pressure. The main difference between the two bias pulse frequencies can be seen for the two oxygen partial pressures $p(O_2)$ = 57.6% and 58.6%. The sample grown at 250 kHz and at the lower partial pressure is characterized by a high transparency, while the 50 kHz sample appears to be non-transparent. The influence of the substrate temperature on the optical appearance is visualized in Figure 6 (b), where hardly any difference can be seen for the deposition runs between room temperature and 400°C. Despite its dominating amorphous structure, the film grown at 500°C appears highly absorbing. A substrate temperature of 600°C leads to a semi-transparent film with a whitish colour, which agrees well with the formation of the T-Nb_2O_5 phase, since Nb_2O_5 polymorphs tend to have a white colour [7].

The transition from non-transparent to transparent observed in Figure 6 at lower oxygen partial pressures of the 250 kHz films is supported by the measured optical properties, which are summarized in Figure 7. The spectral transmittance is higher for the 250 kHz compared to the 50 kHz films, with a maximum transmittance of ~80% at $p(O_2)$ = 63.1%. The reflectance values are similar for all samples, ranging from 20 to 30 %, regardless of the applied oxygen partial pressure (Figure 7 (c) and (d)). Figure 8 (a) compares the transmittance and reflectance development as a function of the oxygen partial pressure

for a wavelength region between 540 and 560 nm, which was chosen since the luminous efficiency function of the human eye for daylight shows its maximum at ~550 nm [22]. Because of the interference fringes of the transparent films, a mean value of transmittance and reflectance was calculated for the wavelength region between 540 and 560 nm. Again, the sharp increase of transmittance was observed for oxygen partial pressures $p(O_2) > 57.6\%$, while the reflectance remains approximately constant over the whole partial pressure range investigated. Poelman et al. [23] suggested a rough method to calculate the refractive index n, based on interference fringes and existing transmission maxima. Applying this method for the films grown at the highest oxygen partial pressure for a wavelength between 500 and 850 nm, the refractive index was calculated to be 2.5, increasing to values of 4.3 for a wavelength below 500 nm (see Figure 8 (b)).

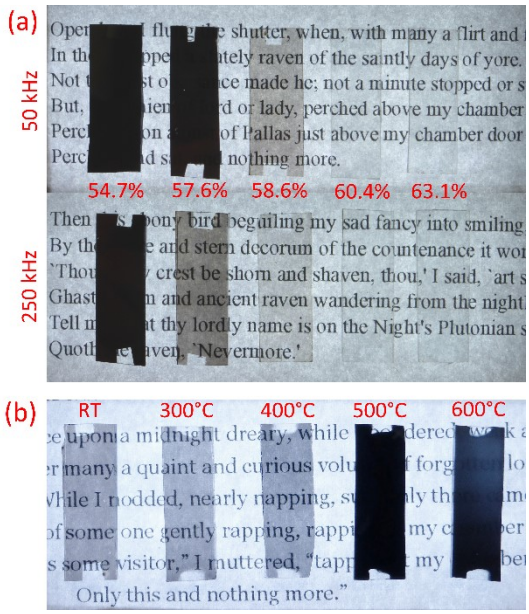

***Figure 6**: (a) NbO_x films deposited on SLG substrates with bias pulse frequencies of 50 and 250 kHz, respectively, and oxygen partial pressure increasing from left to right. ($p(O_2)$ = 54.7, 57.6, 58.6, 60.4 and 63.1%); (b) NbO_x films deposited on SLG substrates with bias pulse frequency of 250 kHz, $p(O_2)$ = 57.6% and increasing substrate temperature from left to right (RT, 300°C, 400°C, 500°C and 600°C).*

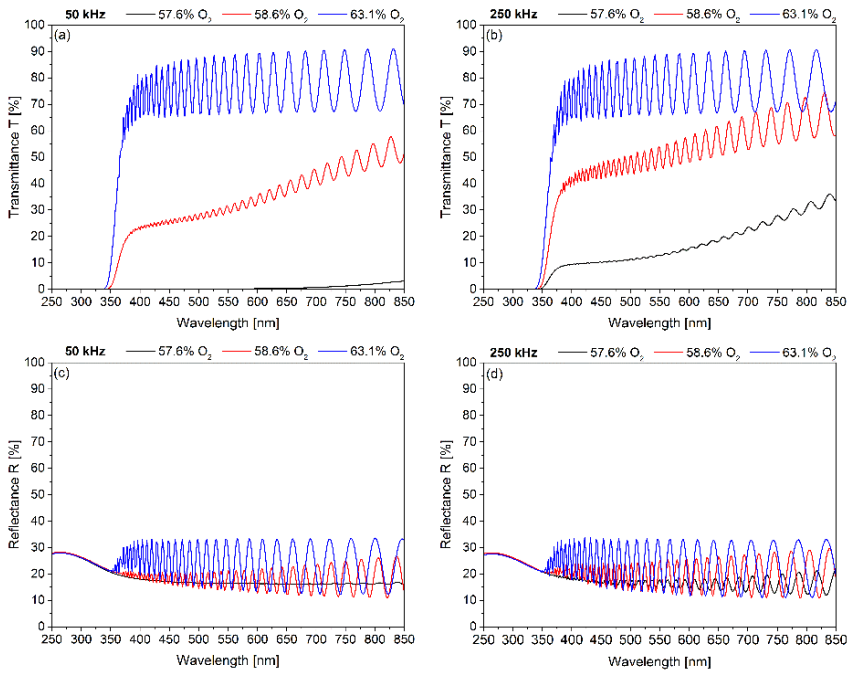

Figure 7: *Optical properties of NbO_x films grown on Corning EAGLE XG glass sheets. (a),(b) Transmittance T and (c),(d) reflectance R as a function of the wavelength.*

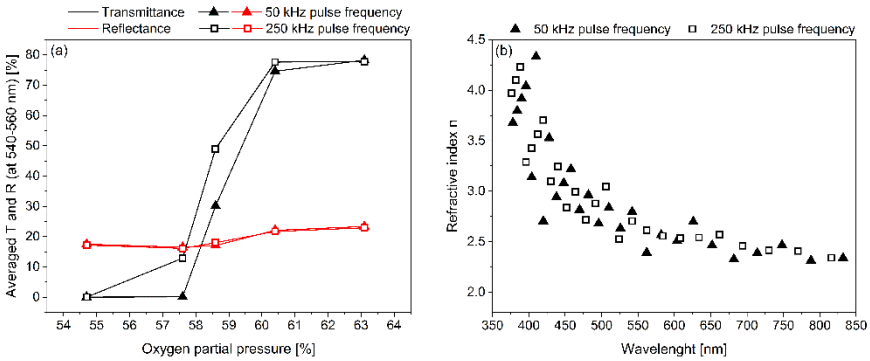

Figure 8: *Optical properties of NbO_x films grown on Corning EAGLE XG glass sheets. (a) Averaged transmittance T and reflectance R as a function of the oxygen partial pressure between 540-560 nm, (b) refractive index n as a function of the wavelength.*

4. Discussion

The continuous increase of the target voltage with increasing oxygen partial pressure is attributed to target poisoning, where an oxide layer is formed on the target surface, which significantly reduces its electrical conductivity [24–27]. Consequently, since the sputter rate decreases with an increasing coverage of the target surface with less conductive oxides, the film growth rate drops, as observed for the increasing oxygen

partial pressures (see Figure 1 (a)). Despite the numerous reports on the effect on target poisoning, only a few reports on the effect of pulse bias conditions on the film growth rate are available. Pulsing the substrate bias voltage affects the flux of charge carriers arriving at the substrate. During the negative pulse, ions are drawn towards the substrate and the growing film, while electrons are attracted during the positive pulse, de-charging a possible positive charge formed during ion bombardment [28,29]. Since the positive pulse duration was held constant at 0.5 µs within the present study, the pulse frequency increase from 50 to 250 kHz corresponds to a decrease of the negative pulse duration, and thus to an increase of the duration available for efficient ion bombardment of the film surface, before positive charging occurs. Lee et al. [30] and Obrosov et at. [31] reported on changes in growth rate with bias pulse frequency, arguing that the increasing ion bombardment and increasing resputtering observed for higher pulse frequency are responsible for the observed decreasing film thickness. Within the present study, the higher pulse frequency also leads to a lower film growth rate (see Figure 1 (a)), which can, however, also be attributed to the observed lower target voltage and the thus lower kinetic energy of Ar^+ ions impinging on the target surface, resulting in reduced sputter erosion and consequently also film growth rate [24]. On the other hand, diffusion of adatoms on the surface of the growing film can also be thermally activated and is therefore affected by the substrate temperature [24]. The observed slight decrease of the film growth rate from 73 to 68 nm/min with increasing substrate temperature can thus be attributed to the thermally enhanced mobility of adatoms on the film surface and the consequently resulting densification of the formed film. Probably, also adatom re-evaporation might contribute to the reduction of the growth rate [24].

An amorphous structure of NbO_x films, especially for Nb_2O_5 films, has been reported several times in literature [2,3,5,6] and agrees well with the findings of the current investigation. The observed formation of a smoother film surface at a higher bias pulse frequency is explained by the increased average number of ions bombarding the film surface before they are repelled by the build-up of negative charge, which enhance the surface mobility of condensed adatoms [32]. A film thickness dependent crystallization, as reported for Nb_2O_5 [6], V_2O_5 [33] and MoO_x films [27] with thicknesses exceeding 1-2 µm and thus substrate temperature induced crystallization during the process-inherent

plasma heating (see Figure 1 (b)) could, however, not be found. The formation of well crystalline films at a substrate temperature of 600°C on the other hand, corresponds to findings reported by Klünsner et al. [34] for sputter deposited V_2O_5 films grown at elevated temperatures and by Ramirez et at. [3] and Lai et al. [5], who post-annealed NbO_x films for 1 h in air at 500 and 600°C, respectively. The orthorhombic T-Nb_2O_5 observed at a substrate temperature of 600°C within this work is known to be stable in the temperature range between 600 and 800°C [7].

Adjusting the detection angle during XPS enables to vary the surface probing depth and thus to investigate the binding state of eventual surface layers [14]. Considering the decreasing peak height of the Nb^{4+} oxidation state with increasing detection angle (and therefore decreased surface probing depth) for those films deposited at the lowest oxygen partial pressure applied (see Figure 3 (a)-(b)), the formation of a few nm thick Nb_2O_5 top layer can be presumed. Due to the reduced probing depth, the detected photoelectrons stem mainly from the Nb_2O_5 top layer. Nb_2O_5 is considered as the thermodynamically most stable NbO_x phase and its formation takes place most probably during storage in ambient air [7,14]. Further it is assumed that the films deposited at the highest oxygen partial pressure, as displayed in Figure 3 (c), are dominated by Nb_2O_5 bonds, while for those films grown at lower oxygen partial pressures shown in Figs. 3 (a) and (b) additional fractions of NbO_2 bonds are formed. To estimate the fraction of Nb^{4+} bonds in the latter films, the total contribution of Nb^{4+} and Nb^{5+} to the measured Nb3d spectra has been calculated following the procedure described in our earlier paper [35]. For peak fitting, the formation of a Nb_2O_5 top layer with variable layer thickness and packing density as well as the Nb^{4+}/Nb^{5+} ratio in the underlying film have been used. The calculation yields a Nb^{4+}/Nb^{5+} ratio of 0.21 or 0.25 for the films deposited with bias pulse frequencies of 50 or 250 kHz, respectively. Furthermore, the calculations indicate an increased Nb_2O_5 top layer thickness for the 250 kHz variants with an at the same time reduced packing density. This more porous surface layer is assumed to be caused by a reduction of Nb-O bonds due to preferential sputtering of oxygen by Ar^+ ions, as reported by Silversmit et al. [36] and Cui et al. [37] for Ar^+ ion bombardment of vanadium oxide phases, where the V atoms are shifted towards lower oxidation states. However, since the films studied within the current investigations are exposed to an oxygen containing atmosphere during deposition, it can be further assumed that those Nb-O

bonds are reconstituted, leading to a volume change and as a result to the formation of pores, explaining the reduced density of the Nb_2O_5 top layers. The increased pulse frequency allows a higher flux of ions enables to be drawn to the substrate [29,32,38,39], and is thus further enhancing this effect. The increased layer thickness of the Nb_2O_5 top layer for the 250 kHz film is supported by the Nb3d XPS spectra (Figure 3 (b)) for a detection angle of 50°, where no Nb^{4+} is present any more, compared to the 50 kHz film variant, displayed in Figure 3 (a).

The differences of the films grown at the two bias pulse frequencies are visible in their optical appearance for the oxygen partial pressures of $p(O_2)$ = 57.6% and $p(O_2)$ = 58.6% (Figure 6 (a)). Both, the ion current and electron current, drawn to the substrate by the negative and positive pulse, respectively, contribute to an increased substrate temperature during deposition. With increasing pulse frequency, plasma parameters like electron temperature and density also increase, leading to a further temperatures rise [28,29,32,38,39]. The slightly higher temperature observed for the 250 kHz deposition (see Figure 1 (b)) can therefore lead to the formation of films richer in the thermodynamically stable Nb_2O_5 at lower oxygen partial pressures [7]. On the other hand, the films deposited at elevated substrate temperatures up to 400°C show almost no change in their optical appearance (see Figure 6 (b)) with respect to those grown at room temperature. The significant change in the optical appearance visible in Figure 6 (b) between 400 and 500°C may indicate the start of crystal growth, with first indications for enhanced X-ray diffraction intensity in Figure 4. Concluding the possible bias related effects by applying different pulse frequencies together with the observed higher transparency for a lower oxygen partial pressure at the higher pulse frequency setting, we assume that the lower target voltage for the 250 kHz deposition determines the differences between the films. The lower target voltage and therefore lower kinetic energy of argon ions bombarding the target surface reduces the number of sputtered Nb atoms [24]. Consequently, a lower number of Nb atoms arrive at the substrate surface, and can subsequently be more easily oxidized in the oxygen containing deposition plasma to Nb_2O_5.

The transmittance and reflectance spectra displayed in Figure 7 are in good agreement with spectra reported by Foroughi-Abari et al. [1], Venkataraj et al. [2] and Franz et al. [8], indicating a shift towards higher transparency with increasing oxygen content. The

transparent films are characterized by interference fringes. The shape of a transmission spectrum is affected by the refractive index n together with the film thickness d. The product of n and d influences the spacing of the interference fringes [23]. With the film thicknesses known from the SEM cross-sections and the wavelength at the transmission maxima from Figures 7 (a) and (b), the refractive index n can be calculated, following the procedure reported in [23]. Comparing the calculated n values at a wavelength between 500 and 850 nm in Figure 8 (b), again a good agreement with values from literature is obtained. Refractive indices between 2.1 and 2.6 are reported for amorphous Nb_2O_5, depending on the synthesis method, microstructure and internal film stresses [2,3,5–7]. The sharp increase of n for a wavelength below 500 nm may indicate the limit for the applied rough calculation method [23], but can also be related to the 2 nm intervals applied for the measurements, leading to a reduced accuracy of the transmission maxima positions.

5. Conclusions

Niobium oxide thin films were deposited by reactive d.c. magnetron sputtering from cold gas sprayed niobium targets, with a variation of oxygen partial pressure, bias pulse frequency and substrate temperature, to evaluate microstructural/chemical evolution and optical properties of the films. The amorphous, transparent films deposited without additional substrate heating at the highest oxygen partial pressure consist solely of Nb_2O_5, while additional fractions of NbO_2 are present for the lowest oxygen partial pressure, which is reflected by their non-transparent characteristics. The increase of the bias pulse frequency from 50 to 250 kHz leads to a decreasing target voltage, resulting in a reduced Ar^+ ion kinetic energy and therefore decreased target sputter erosion and consequent film growth rate. With the reduced number of Nb atoms sputtered, optical transparency was reached for films grown at 250 kHz at lower oxygen partial pressures films compared to the 50 kHz films. Since the target surface is increasingly poisoned with increasing oxygen partial pressure, a decline of the film growth rate from 83 to 48 nm/min could be observed. A substrate temperature of 600°C leads to formation of crystalline films consisting of the orthorhombic Nb_2O_5 phase with semi-transparent whitish appearance.

6. Acknowledgments

This work was supported by the Österreichische Forschungsförderungsgesellschaft FFG within the project "E²CGS" (project number: 150130). ERDA measurements were performed at the "Helmholtz Zentrum Dresden Rossendorf" in Dresden, Germany. The authors are grateful to Michaela Zaberning (Plansee SE, Reutte, Austria) for SEM characterization.

7. References

[1] A. Foroughi-Abari, K.C. Cadien, Growth, structure and properties of sputtered niobium oxide thin films, Thin Solid Films 519 (2011) 3068–3073.

[2] S. Venkataraj, R. Drese, O. Kappertz, R. Jayavel, M. Wuttig, Characterization of niobium oxide films prepared by reactive dc magnetron sputtering, Phys. Stat. sol. (a) 188 (2001) 1047–1058.

[3] G. Ramírez, S.E. Rodil, S. Muhl, D. Turcio-Ortega, J.J. Olaya, M. Rivera, E. Camps, L. Escobar-Alarcón, Amorphous niobium oxide thin films, J. Non-Cryst. Solids. 356 (2010) 2714–2721.

[4] K. Yoshimura, T. Miki, S. Iwama, S. Tanemura, Characterization of niobium oxide electrochromic thin films prepared by reactive d.c. magnetron sputtering, Thin Solid Films 281-282 (1996) 235–238.

[5] F. Lai, M. Li, H. Wang, H. Hu, X. Wang, J.G. Hou, Y. Song, Y. Jiang, Optical scattering characteristic of annealed niobium oxide films, Thin Solid Films 488 (2005) 314–320.

[6] F. Lai, L. Lin, Z. Huang, R. Gai, Y. Qu, Effect of thickness on the structure, morphology and optical properties of sputter deposited Nb_2O_5 films, Appl. Surf. Sci. 253 (2006) 1801–1805.

[7] C. Nico, T. Monteiro, M.P.F. Graça, Niobium oxides and niobates physical properties: Review and prospects, Prog. Mater. Sci. 80 (2016) 1–37.

[8] R. Franz, C. Clavero, J. Kolbeck, A. Anders, Influence of ionisation zone motion in high power impulse magnetron sputtering on angular ion flux and NbO_x film growth, Plasma Sources Sci. T. 25 (2016) 15022.

[9] S. Grigoriev, A. Okunkova, A. Sova, P. Bertrand, I. Smurov, Cold spraying: From process fundamentals towards advanced applications, Surf. Coat. Tech. 268 (2015) 77–84.

[10] T. Schmidt, H. Assadi, F. Gärtner, H. Richter, T. Stoltenhoff, H. Kreye, T. Klassen, From particle acceleration to impact and bonding in cold spraying, J. Therm. Spray. Techn. 18 (2009) 794–808.

[11] T.H. van Steenkiste, J.R. Smith, R.E. Teets, J.J. Moleski, D.W. Gorkiewicz, R.P. Tison, D.R. Marantz, K.A. Kowalsky, W.L. Riggs, P.H. Zajchowski, B. Pilsner, R.C. McCune, K.J. Barnett, Kinetic spray coatings, Surf. Coat. Tech. 111 (1999) 62–71.

[12] J.M. Schneider, A. Anders, B. Hjörvarsson, I. Petrov, K. Macák, U. Helmersson, J.-E. Sundgren, Hydrogen uptake in alumina thin films synthesized from an aluminum plasma stream in an oxygen ambient, Appl. Phys. Lett. 74 (1999) 200–202.

[13] B. Vincent Crist, PDF handbooks of monochromatic XPS spectra (Demo version): Volume 1 - The elements and native oxides, Mountain View, California, USA, 1999.

[14] Q. Ma, R.A. Rosenberg, Angle-resolved X-ray photoelectron spectroscopy study of the oxides on Nb surfaces for superconducting r.f. cavity applications, Appl. Surf. Sci. 206 (2003) 209–217.

[15] T. Hryniewicz, K. Rokosz, H.Z. Sandim, SEM/EDX and XPS studies of niobium after electropolishing, Appl. Surf. Sci. 263 (2012) 357–361.

[16] Y. Tanaka, M. Nakai, T. Akahori, M. Niinomi, Y. Tsutsumi, H. Doi, T. Hanawa, Characterization of air-formed surface oxide film on Ti–29Nb–13Ta–4.6Zr alloy surface using XPS and AES, Corros. Sci. 50 (2008) 2111–2116.

[17] International Centre for Diffraction Data, Card 00-027-1003 for orthorhombic Nb_2O_5, 2007.

[18] B.X. Huang, K. Wang, J.S. Church, L. Ying-Sing, Characterization of oxides on niobium by raman and infrared spectroscopy, Electrochim. Acta 44 (1999) 2571–2577.

[19] M. Palatnikov, O. Shcherbina, N. Sidorov, I. Skab, K. Bormanis, The structure of niobium and tantalum oxides processed by concentrated light flux, Ukr. J. Phys. Opt. 13 (2012) 207.

[20] Y. Zhao, Z. Zhang, Y. Lin, Optical and dielectric properties of a nanostructured NbO_2 thin film prepared by thermal oxidation, J. Phys. D: Appl. Phys. 37 (2004) 3392–3395.

[21] K. Uchinokura, T. Sekine, E. Matsuura, Raman scattering by silicon, Solid. State. Commun. 11 (1972) 47–49.

[22] L.T. Sharpe, A. Stockman, W. Jagla, H. Jagle, A luminous efficiency function, V*(λ), for daylight adaptation, J. Vision. 5 (2005) 948–968.

[23] D. Poelman, P.F. Smet, Methods for the determination of the optical constants of thin films from single transmission measurements: a critical review, J. Phys. D: Appl. Phys. 36 (2003) 1850–1857.

[24] K. Wasa, I. Kanno, H. Kotera, Handbook of sputter deposition technology: Fundamentals and applications for functional thin films, nano-materials and MEMS, 2nd ed., Elsevier/Andrew, Amsterdam u. a., 2012.

[25] W.D. Sproul, D.J. Christie, D.C. Carter, Control of reactive sputtering processes, Thin Solid Films 491 (2005) 1–17.

[26] J.M. Pachlhofer, C. Jachs, R. Franz, E. Franzke, H. Köstenbauer, J. Winkler, C. Mitterer, Structure evolution in reactively sputtered molybdenum oxide thin films, Vacuum 131 (2016) 246–251.

[27] J.M. Pachlhofer, A.T. Martín-Luengo, R. Franz, E. Franzke, H. Köstenbauer, J. Winkler, A. Bonanni, C. Mitterer, Industrial-scale sputter deposition of molybdenum oxide thin films: Microstructure evolution and properties, J. Vac. Sci. Technol. A 35 (2017) 21504.

[28] P.J. Kelly, R. Hall, J. O'Brien, J.W. Bradley, P. Henderson, G. Roche, R.D. Arnell, Studies of mid-frequency pulsed dc biasing, J. Vac. Sci. Technol. A 19 (2001) 2856.

[29] P.J. Kelly, R. Hall, J. O'Brien, J.W. Bradley, G. Roche, R.D. Arnell, Substrate effects during mid-frequency pulsed DC biasing, Surf. Coat. Tech. 142-144 (2001) 635–641.

[30] J.-W. Lee, S.-K. Tien, Y.-C. Kuo, The effects of substrate bias, substrate temperature, and pulse frequency on the microstructures of chromium nitride coatings deposited by pulsed direct current reactive magnetron sputtering, J. Electron. Mater. 34 (2005) 1484–1492.

[31] A. Obrosov, M. Naveed, A.A. Volinsky, S. Weiß, Substrate frequency effects on Cr_xN coatings deposited by dc magnetron sputtering, J. Mater. Ebg. Perform. 26 (2017) 366–373.

[32] E. Barnat, T.-M. Lu, Pulsed bias magnetron sputtering of thin films on insulators, J. Vac. Sci. Technol. A 17 (1999) 3322–3326.

[33] N. Fateh, G.A. Fontalvo, L. Cha, T. Klünsner, G. Hlawacek, C. Teichert, C. Mitterer, Synthesis–structure relations for reactive magnetron sputtered V_2O_5 films, Surf. Coat. Tech. 202 (2008) 1551–1555.

[34] T. Klünsner, Q. Shen, G. Hlawacek, C. Teichert, N. Fateh, G.A. Fontalvo, C. Mitterer, Morphology characterization and friction coefficient determination of sputtered V_2O_5 films, Thin Solid Films 519 (2010) 1416–1420.

[35] R. Lorenz, M. O'Sullivan, A. Fian, D. Sprenger, B. Lang, C. Mitterer, A comparative study on NbO_x films reactively sputtered from sintered and cold gas sprayed targets, Appl. Surf. Sci. 436 (2018) 1157–1162.

[36] G. Silversmit, D. Depla, H. Poelman, G.B. Marin, R. de Gryse, Determination of the V2p XPS binding energies for different vanadium oxidation states (V^{5+} to V^{0+}), J. Electron. Spectrosc. 135 (2004) 167–175.

[37] J. Cui, D. Da, W. Jiang, Structure characterization of vanadium oxide thin films prepared by magnetron sputtering methods, Appl. Surf. Sci. 133 (1998) 225–229.

[38] P.J. Kelly, R.D. Arnell, Magnetron sputtering: a review of recent developments and applications, Vacuum 56 (2000) 159–172.

[39] K.E. Cooke, J. Hamsphire, W. Southall, D.G. Teer, The industrial application of pulsed DC bias power supplies in closed field unbalanced magnetron sputter ion plating, Surf. Coat. Tech. 177-178 (2004) 789–794.